



Yoiz Eleduvith Nuñez Ruiz

**Modeling and Characterization of a
Holographic Artificial Impedance Antenna
Operating in Microwave and Terahertz
Frequencies**

Dissertação de Mestrado

Dissertation presented to the Programa de Pós-graduação em Engenharia Elétrica of PUC-Rio in partial fulfillment of the requirements for the degree of Mestre em Engenharia Elétrica.

Advisor : Prof. Glaucio Lima Siqueira
Co-advisor: Prof. Marbey Manhães Mosso

Rio de Janeiro
August 2019



Yoiz Eleduvith Nuñez Ruiz

**Modeling and Characterization of a
Holographic Artificial Impedance Antenna
Operating in Microwave and Terahertz
Frequencies**

Dissertation presented to the Programa de Pós-graduação em Engenharia Elétrica of PUC-Rio in partial fulfillment of the requirements for the degree of Mestre em Engenharia Elétrica. Approved by the Examination Committee.

Prof. Luiz Alencar Reis da Silva Mello

Centro de Estudos em Telecomunicações – PUC-Rio

Prof. Marbey Manhães Mosso

Co-advisor

Centro de Estudos em Telecomunicações – PUC-Rio

Prof. Marco Antonio Grivet

Centro de Estudos em Telecomunicações – PUC-Rio

Dr. Jorge Angelo Mitrione Souza

Centro de Estudos em Telecomunicações – PUC-Rio

Prof. Leni Joaquim de Matos

Universidade Federal Fluminense – UFF

Rio de Janeiro, August 23rd, 2019

All rights reserved.

Yoiz Eleduvith Nuñez Ruiz

The author received the Electronic Engineer degree from the Technological University of Honduras (UTH) in 2012 and the degree of Master in Project Management from the Central American Technology University (UNITEC) in 2016. She worked for Claro Honduras accumulating 5 five years of experience at the Network Operation Center (NOC) and Network Quality (NQ) department, dealing with the management and optimization of the mobile network 2G, 3G, and LTE.

Bibliographic data

Ruiz, Yoiz Eleduvith Nuñez

Modeling and Characterization of a Holographic Artificial Impedance Antenna Operating in Microwave and Terahertz Frequencies / Yoiz Eleduvith Nuñez Ruiz; advisor: Glaucio Lima Siqueira; co-advisor: Marbey Manhães Mosso. – 2019.

134 f: il. color. ; 30 cm

Dissertação (mestrado) - Pontifícia Universidade Católica do Rio de Janeiro, Departamento de Engenharia Elétrica, 2019.

Inclui bibliografia

1. Engenharia Elétrica – Teses. 2. Ondas de vazamento;. 3. Tecnologia SIW;. 4. Varredura de feixe controlado por frequência;. 5. Princípio holográfico;. 6. Superfície de impedância artificial.. I. Siqueira, Glaucio Lima. II. Mosso, Marbey Manhães. III. Pontifícia Universidade Católica do Rio de Janeiro. Departamento de Engenharia Elétrica. IV. Título.

CDD: 621.3

Acknowledgments

I would like to express my most enormous gratitude to God, to give me the courage and strength to continue advancing in my professional and personal life.

I would also like to express my sincere gratitude to my parents, Olga and Francisco and my brother Jecel and sister Cynthia for offering me their unconditional love and support.

I also wish to express my gratitude to my advisor, Glaucio Lima Siqueira, by his guidance and patient in the preparation of this dissertation and my co-advisor, Marbey Manhães Mosso, for everything learned, his patient, shared stories and his suggestions in the development of this work.

I am very grateful to my colleagues and friends Johnes and Bruno, for their time dedicated to this work, for their observations and for always encouraging me. You are like my Brazilian brothers.

I would like to especially thank Virgilio for the collaboration with the codes in MATLAB, a significant contribution which allowed to carry out this work.

I would like to thank Guilherme and Rodolfo for their collaboration and patient with the measurements in the Anechoic Chamber.

I would like to thank my colleagues and friends of the Center for Studies in Telecommunications (CETUC) and SBMeta (Sociedade Brasileira de Meta-materiais) for their friendship and support.

I also wish to thank CNPq and PUC-Rio for the financial support. Without them, this work would not have been realized.

I am also very grateful to my fiancé Jorge Castellanos. Thank you for inspiring and motivating me to achieve my dreams, by staying with me in difficult times and for your unconditional love.

Abstract

Ruiz, Yoiz Eleduith Nuñez; Siqueira, Glaucio Lima (Advisor); Mosso, Marbey Manhães (Co-Advisor). **Modeling and Characterization of a Holographic Artificial Impedance Antenna Operating in Microwave and Terahertz Frequencies**. Rio de Janeiro, 2019. 134p. Dissertação de Mestrado – Departamento de Engenharia Elétrica, Pontifícia Universidade Católica do Rio de Janeiro.

This work aims to present the development of a holographic artificial impedance antenna (HAIA) for potential applications in satellite systems in the X (8 - 12 GHz) and Ku (12 - 18 GHz) bands, as well as in the frequency of terahertz. As a proof of concept, the prototype is created to operate in the K (18 - 27 GHz) band, specifically at the design frequency of 18.4 GHz. HAIA is a kind of leaky-wave antenna (LWA) with a unique operating principle for controlled beam radiation. Due to their radiation characteristics are broad, and the degree of design freedom allows us to explore the antenna performance, different parameters are studied for modeling. The antenna design obeys the established theory for the leaky-wave radiation in the conversion of a surface wave into a leaky-wave, where an artificial impedance surface (AIS) is characterized and distributed on a dielectric substrate using the holographic principle developed in the optical system. In order to minimize the dimensions of the HAIA, a planar surface wave launcher is studied and compared with the performance of conventional surface wave feeding used in this type of structure. A series of designs are evaluated for the conclusion of the best result and compared with other works. The final prototype is manufactured for experimental tests, where the results show that the designed antenna responds to the modeled characteristics with a good agreement between the simulated and measured results.

Keywords

Leaky-waves; SIW technology; Frequency-controlled beam scanning; Holographic principle; Artificial impedance surface.

Resumo

Ruiz, Yoiz Eleduith Nuñez; Siqueira, Glaucio Lima; Mosso, Marbey Manhães. **Modelamento e Caracterização de uma Antena Holográfica de Impedância Artificial Operando nas Frequências de Microondas e Terahertz**. Rio de Janeiro, 2019. 134p. Dissertação de Mestrado – Departamento de Engenharia Elétrica, Pontifícia Universidade Católica do Rio de Janeiro.

Este trabalho tem como objetivo apresentar o desenvolvimento de uma antena HAIA (*Holographic Artificial Impedance Antenna*) para potenciais aplicações em sistemas de satélites nas bandas X (8 - 12 GHz) e Ku (12 - 18 GHz), bem como na frequência de terahertz. Como prova de conceito, o protótipo é criado para operar na banda K (18 - 27 GHz), especificamente na frequência de 18,4 GHz. O HAIA é um tipo de antena com ondas vazadas, com um princípio operacional único para radiação de feixe controlado. Devido às suas amplas propriedades de radiação, o grau de liberdade do projeto nos permite explorar o comportamento de resposta da antena e diferentes parâmetros para sua modelagem são estudados. O projeto da antena obedece à teoria estabelecida para a radiação de ondas vazadas na conversão de uma onda de superfície para uma onda com vazamento, onde uma AIS (*Artificial Impedance Surface*) é caracterizada e distribuída em um substrato dielétrico usando o princípio holográfico desenvolvido no sistema óptico. A fim de minimizar as dimensões da antena, uma fonte planar é estudada para gerar uma onda de superfície e comparada com o desempenho da alimentação de onda de superfície convencional neste tipo de estrutura. Os diferentes projetos são avaliados para a conclusão do melhor resultado e comparados com outros trabalhos. O protótipo final é fabricado para testes experimentais, onde os resultados provam que a antena projetada responde às características modeladas, com uma boa concordância entre os resultados simulados e medidos.

Palavras-chave

Ondas de vazamento; Tecnologia SIW; Varredura de feixe controlado por frequência; Princípio holográfico; Superfície de impedância artificial.

Table of contents

1	Introduction	18
1.1	Objectives	20
1.2	Methodology of the Project	20
2	Fundamental Concepts	22
2.1	Surface Waves	22
2.2	Leaky-Waves	24
2.3	Background of Metamaterials	24
2.4	State-of-art: Artificial Impedance Surface	27
2.5	Scalar and Tensor Surface Impedance	31
2.5.1	Scalar AIS	32
2.5.2	Tensor Surface Impedance	34
3	Fundamental Theory of Leaky-Wave Antennas	36
3.1	Approaches of LWAs Design	36
3.2	Uniform LWA	37
3.3	Periodic LWA	40
3.4	Modulation of the Surface Impedance	41
3.5	Applications in LWAs	44
3.6	Terahertz LWA	45
4	Holographic Artificial Impedance Antenna	46
4.1	Background of Holography in Microwave System	46
4.2	Principles of Holography	47
4.3	Parameters of Radiation Efficiency	49
4.4	Fundamental Performance Parameters	51
4.4.1	Return Loss and Reflection Coefficient	51
4.4.2	Scattering Parameter	52
4.4.3	Voltage Standing Wave Ratio	52
4.4.4	Efficiency	52
4.4.5	Aperture efficiency	53
4.4.6	Directivity	53
4.4.7	Gain	53
4.4.8	Beamwidth	54
4.4.9	Radiation Pattern	55
4.4.10	Bandwidth	55
4.4.11	Front-to-back ratio	56
4.4.12	Polarization	56
4.5	Co-polarization and Cross-polarization	56
4.6	Axial Ratio	57
4.7	Field Regions of the Antenna	57
5	Planar Surface Wave Feeding	58
5.1	Characteristics of Surface Wave Feeding	58

5.2	Conventional H-plane Sectoral Antenna	59
5.3	SIW H-plane Sectoral Feeding	61
5.4	Printed Transition Zone	62
6	Design Procedure of the HAIA	65
6.1	Design Goals	65
6.2	Modeling of the AIS	65
6.2.1	Influence of the phase difference in the Unit Cell	67
6.2.2	Modeling of the Scalar Surface Impedance	68
6.3	Modeling of the Holographic Pattern	71
6.4	Modeling of the SIW H-sectoral Feeding	72
6.4.1	Modeling of the Printed Transition Zone	73
6.4.2	Modeling of the SIW with Coaxial Probe	74
6.5	Modeling SIW with Microstrip Line	78
6.5.1	Modeling of the Monopole Feeding	80
7	Simulations of the Holographic Artificial Impedance Antenna	83
7.1	HAIA with SIW H-sectoral feeding	83
7.1.1	Coaxial probe connection	83
7.1.2	Frequency-controlled Beam Scanning	89
7.1.3	VSWR	91
7.1.4	Microstrip line connection	92
7.2	HAIA with Monopole Feeding	94
7.3	HAIA with Horizontal Polarization	97
7.4	Conclusion of the Proposed Designs	99
7.5	Change in the Design Radiation Angle	100
8	Antenna Design for X and Ku bands, and Terahertz frequency	103
8.1	Results for the X and Ku bands	103
8.2	Results for Terahertz Frequency	106
8.2.1	Modeling of the Unit Cell in THz Frequency	107
9	Prototype Realization and Results	112
9.1	Prototype of the Fabricated Antenna	112
9.2	Measurement of the Reflection Coefficient	113
9.3	Measurements in Anechoic Chamber	114
10	Final comments and Conclusions	120
	Bibliography	123
A	Specification Sheet of the Coaxial Probe Connector	131
B	Specification sheet of the Horn Antenna	132
C	Near-field Plots	134

List of figures

Figure 2.1	Reflection and transmission of a plane wave at an interface.	22
Figure 2.2	Structure of a metamaterial with properties: (a) negative magnetic permeability, (b) negative electric permittivity, and (c) realization of metamaterial with refractive negative index [15].	25
Figure 2.3	Effect of the Snell's law in: (a) conventional material, and (b) double-negative material.	25
Figure 2.4	Categories of metamaterials based on their effective properties.	27
Figure 2.5	Examples of photonic crystals periodic in: (a) 1-D, (b) 2-D, and (c) 3-D.	28
Figure 2.6	Sievenpiper mushroom surface: (a) unit cell, and (b) equivalent circuit.	28
Figure 2.7	Reflection and transmission of a plane wave in an interface with metal conductor [8].	29
Figure 2.8	Reflection and transmission of a plane wave in an interface with AIS [8].	30
Figure 2.9	Propagation of a surface wave on a impedance surface [8].	30
Figure 2.10	Example of a AIS unit cell for application in antennas: (a) frontal view, and (b) top view.	32
Figure 2.11	Schematic propagation of the surface wave mode: (a) TM-polarization, and (b) TE-polarization [27].	32
Figure 2.12	Magnitude of the electric field in V/m of the evaluated geometries: (a) circular unit cell, (b) square unit cell, and (c) triangle unit cell.	33
Figure 2.13	Surface current vector in A/m of the evaluated geometries: (a) circular unit cell, (b) square unit cell, and (c) triangle unit cell.	33
Figure 2.14	Phase of the reflection coefficient of the evaluated geometries.	34
Figure 2.15	Examples of AIS unit cell with tensorial impedance.	35
Figure 2.16	Example of a tensor impedance distribution using square sliced gap unit cell [4].	35
Figure 3.1	Dispersion diagram of the condition for the backward and forward radiation of an LWA.	36
Figure 3.2	Illustration of a uniform LWA: (a) rectangular waveguide with a continuous slot [35], (b) rectangular waveguide with circular slots, and (c) circular waveguide with a continuous slot [36].	37
Figure 3.3	Uniform LWA in the form of a rectangular waveguide with a continuous aperture slot in the top wall for the leakage energy.	38
Figure 3.4	Ray diagram of power flow in free-space with exponential growth [39].	39

Figure 3.5	Ray diagram of power flow in free-space with exponential decay [39].	39
Figure 3.6	Example of an open waveguide with periodic discontinuities on the surface.	40
Figure 3.7	Dispersion diagram in a conventional rectangular waveguide.	41
Figure 3.8	Sinusoidal modulation in one-dimension (1-D) of the surface impedance and its propagation constants.	42
Figure 3.9	Illustration of forward and backward leaky-wave modes in a periodic LWA.	43
Figure 3.10	Slotted SIW leaky-wave antenna [45].	44
Figure 3.11	LWA based on a right/left-handed metamaterial.	45
Figure 4.1	Examples of holographic antennas with (a) linear metallic film [52], and (b) curve metallic film [53].	46
Figure 4.2	Example of a hologram image [54].	47
Figure 4.3	Recording process of the hologram.	47
Figure 4.4	Reconstruction process of the hologram.	48
Figure 4.5	Illustration of the holographic principle in microwave system.	49
Figure 4.6	Representation of the maximum radiation angle of the antenna [33].	50
Figure 4.7	S-matrix.	52
Figure 4.8	2-D Radiation pattern [59].	54
Figure 4.9	3-D Radiation pattern [59].	55
Figure 4.10	Polarization ellipse [59].	57
Figure 5.1	Types of planar feeding using: (a) microstrip line [7], (b) SIW H-sectoral antenna [8], (c) Vivaldi antenna [9], and (d) quasi-Yagi antenna [10].	58
Figure 5.2	Structure of a conventional H-plane sectoral antenna: (a) frontal view, and (b) top view [59].	60
Figure 5.3	Radiation pattern of the E- and H-plane of a conventional H-plane sectoral antenna [59].	61
Figure 5.4	Geometry of a SIW H-plane sectoral feeding.	62
Figure 5.5	Values of gain for different lengths and waveguides aperture for the SIW-H sectoral feeding [67].	63
Figure 5.6	Transition zone with parallel blocks.	63
Figure 5.7	Transition zone with small rectangles.	64
Figure 6.1	Setup used in the full-wave simulation of the unit cell on HFSS.	66
Figure 6.2	Resonance frequencies of the unit cell with variation of the phase difference.	67
Figure 6.3	Surface impedance of the unit cell for the different material tested.	68
Figure 6.4	Resonance frequencies for the different materials tested.	69
Figure 6.5	Relationship between gaps and surface impedance of the unit cell for different geometries tested.	70

Figure 6.6 Relationship between gaps and surface impedance of the unit cell with square patch.	70
Figure 6.7 Flow diagram of the distribution of the surface impedance.	71
Figure 6.8 Example of a holographic pattern with square patches.	72
Figure 6.9 Transition zone in the SIW feeding with: (a) rectangular patches, and (b) small triangles.	73
Figure 6.10 Coaxial probe technique: (a) top view, and (b) frontal view.	74
Figure 6.11 SIW H-plane feeding: (a) without transition zone, (b) transition zone of rectangular patches, and (c) transition zone of small triangles. Total dimension: $W_m = 50$ mm, $L_m = 40$ mm and $Z_t = 6.95$ mm.	75
Figure 6.12 Comparative reflection coefficient results among the transition zones using coaxial probe connection.	76
Figure 6.13 SIW structure with coaxial probe: (a) magnitude of the electric field, in V/m, and (b) 3-D radiation pattern, at $f_o = 18.4$ GHz.	77
Figure 6.14 Comparative of the different structure SIW H-sectoral with coaxial probe connection: (a) E-plane ($\phi = 0^\circ$), and (b) H-plane ($\theta = 90^\circ$) at the maximum resonance frequency.	77
Figure 6.15 Microstrip line feeding.	78
Figure 6.16 Simulated reflection coefficient for the SIW with microstrip line.	79
Figure 6.17 Radiation pattern of the SIW with microstrip line for the E-plane ($\phi = 0^\circ$) and H-plane ($\theta = 90^\circ$).	80
Figure 6.18 SIW structure with microstrip line: (a) magnitude of the electric field, in V/m, and (b) 3-D radiation pattern, at $f_o = 18.4$ GHz.	80
Figure 6.19 Monopole of a quarter-wavelength: (a) view of the structure, and (b) 3-D radiation pattern.	81
Figure 6.20 Simulated reflection coefficient of the monopole.	81
Figure 6.21 Comparative results of axial ratio among the types of feeding studied, at $f_o = 18.4$ GHz.	82
Figure 7.1 Simulated HAIA with SIW H-sectoral feeding coaxial probe connection, at $f_o = 18.4$ GHz and $\theta_d = 20^\circ$.	84
Figure 7.2 Radiation Pattern E-plane ($\phi = 0^\circ$) for different dimensions of the HAIA at $f_o = 18.4$ GHz with coaxial probe connection, maximum gain of 23.18 dB.	85
Figure 7.3 Radiation Pattern E-plane ($\phi = 0^\circ$) for the lower and higher dimensions of the HAIA at $f_o = 18.4$ GHz with coaxial probe connection, maximum gain of 23.18 dB.	85
Figure 7.4 3-D radiation pattern for the HAIA with coaxial probe connection at $f_o = 18.4$ GHz.	86
Figure 7.5 Comparative result of reflection coefficient between the HAIA with coaxial probe connection (size of $12.26\lambda^2$) and the SIW feeding.	87

Figure 7.6 Distribution of the (a) magnitude of electric field, in V/m, and (b) magnitude of the surface current, in A/m, at $f_o = 18.4$ GHz and $\theta_d = 20^\circ$.	87
Figure 7.7 Radiation pattern SIW H-sectoral with coaxial probe, E-plane ($\phi = 0^\circ$) at $f_o = 18.4$ GHz, maximum gain of 22.02 dB at $\theta_m = 23^\circ$.	88
Figure 7.8 Radiation pattern for the co- and cross- polarization component of the gain at $f_o = 18.4$ GHz, HAIA with coaxial probe connection.	88
Figure 7.9 Gain versus frequency and maximum radiation angle in the firsts operating band, with scanning range from 13.5° to 16° .	89
Figure 7.10 Radiation pattern of the firsts band, E-plane ($\phi = 0^\circ$).	90
Figure 7.11 Gain versus frequency and maximum radiation angle in the second operating band, with scanning range from 22° to 24° .	91
Figure 7.12 Radiation pattern of the second band, E-plane ($\phi = 0^\circ$).	91
Figure 7.13 Comparative result of VSWR between the HAIA and the SIW feeding.	92
Figure 7.14 HAIA with microstrip line feeding, size of $12.26\lambda^2$, at $f_o = 18.4$ GHz and $\theta_d = 20^\circ$.	93
Figure 7.15 Simulated radiation pattern of the E-plane ($\phi = 0^\circ$) of the HAIA using microstrip line at $f_o = 18.4$ GHz, with maximum gain of 21.81 dB at $\theta_m = 24^\circ$.	93
Figure 7.16 Radiation pattern for the co- and cross- polarization component of the gain at $f_o = 18.4$ GHz, HAIA with microstrip line connection.	94
Figure 7.17 Holographic antenna with monopole feeding, size of $12.26\lambda^2$, at $f_o = 18.4$ GHz and $\theta_d = 20^\circ$.	94
Figure 7.18 Comparative gain result of the HAIA with monopole feeding for variation in the focus position, size of $12.26\lambda^2$, at $f_o = 18.4$ GHz.	95
Figure 7.19 Comparative radiation pattern, E-plane ($\phi = 0^\circ$) of the holographic antenna with monopole feeding and SIW H-plane sectoral (size of $15.33\lambda^2$ in both structures).	96
Figure 7.20 Distribution of the (a) magnitude of the electric field, in V/m, and (b) magnitude of the surface current, in A/m, size of $15.33\lambda^2$, at $f_o = 18.4$ GHz.	97
Figure 7.21 Holographic surface with 180° out-of-phase, for horizontal polarization, at $f_o = 18.4$ GHz and $\theta_d = 20^\circ$.	97
Figure 7.22 Radiation pattern of the co- and cross-polarization components of the gain, E-plane ($\phi = 0^\circ$), horizontal polarization, size of $12.26\lambda^2$, at $f_o = 18.4$ GHz.	98
Figure 7.23 Radiation pattern of the co- and cross-polarization components of the gain, E-plane ($\phi = 0^\circ$), horizontal polarization, size of $15.33\lambda^2$, at $f_o = 18.4$ GHz.	99
Figure 7.24 Radiation angle tested on the holographic surface: (a) $\theta_d = 0^\circ$, and (b) $\theta_d = 90^\circ$, size of $12.26\lambda^2$ at $f_o = 18.4$ GHz.	101
Figure 7.25 Simulated radiation pattern of the HAIA SIW H-sectoral at $f_o = 18.4$ GHz, $\theta_m = 4^\circ$, E-plane ($\phi = 0^\circ$).	101

Figure 7.26 Simulated radiation pattern of the HAIA SIW H-sectoral at $f_o = 18.4$ GHz, $\theta_d = 90^\circ$ E-plane ($\phi = 0^\circ$).	102
Figure 8.1 Relationship between the gap and surface impedance of the unit cell, at the central frequency of 11.63 GHz.	103
Figure 8.2 Relationship between the gap and impedance surface of the unit cell, at central frequency of 14.29 GHz.	104
Figure 8.3 Reflection coefficient of the SIW feeding at central frequency of 11.63 GHz (bandwidth operation from 11.60 to 11.75 GHz, BW = 150 MHz).	105
Figure 8.4 Reflection coefficient of the SIW feeding at central frequency of 14.29 GHz (bandwidth operation from 14.20 to 14.42 GHz, BW = 220 MHz).	105
Figure 8.5 Radiation pattern of the co-polarization of the gain at $f_o = 11.63$ GHz, E-plane ($\phi = 0^\circ$).	106
Figure 8.6 Radiation pattern of the co-polarization of the gain at $f_o = 14.29$ GHz, E-plane ($\phi = 0^\circ$).	106
Figure 8.7 Impedance value for THz frequency.	107
Figure 8.8 Antenna modeled in THz frequency.	108
Figure 8.9 Simulated reflection coefficient of the HAIA operating at the THz frequency.	109
Figure 8.10 Simulated radiation pattern E-plane ($\phi = 0^\circ$) of the HAIA at $f_o = 1.205$ THz, with maximum gain of 24.45 dB.	109
Figure 8.11 Radiation pattern of the HAIA, in the firsts band, E-plane ($\phi = 0^\circ$), THz frequency.	110
Figure 8.12 Radiation pattern of the HAIA, in the second band, E-plane ($\phi = 0^\circ$), THz frequency.	110
Figure 9.1 Demonstration of the fabricated antenna (rule in cm).	112
Figure 9.2 Setup for the measurement of the reflection coefficient: (a) top view of the holographic surface, and (b) close view of the feeding system.	113
Figure 9.3 Software of the analyzer Teledyne Lecroy.	113
Figure 9.4 Comparative result between the simulated and measured reflection coefficient of the antenna.	114
Figure 9.5 Initial setup in the anechoic chamber of CETUC, at 18.4 GHz: (a) position of the horn antennas with 20 dB of gain, and (b) FieldFox analyzer.	114
Figure 9.6 Normalized radiation pattern measured of the horn antenna for the initial setup at $f_o = 18.4$ GHz, E-plane ($\phi = 0^\circ$).	115
Figure 9.7 Setup in the anechoic chamber of CETUC to measures the co-polarization component of the HAIA.	115
Figure 9.8 Normalized radiation pattern measured for the co-polarization gain at $f_o = 18.4$ GHz, E-plane ($\phi = 0^\circ$). Maximum radiation angle at 26° .	116
Figure 9.9 Transmission coefficient measured for the co- and cross-polarization component of the HAIA at 18.4 GHz.	116

Figure 9.10 Normalized pattern measured for the co-polarization component of the antenna at $f_o = 18.2$ GHz. Maximum radiation angle at 24° .	117
Figure 9.11 Normalized pattern measured for the co-polarization component of the antenna at $f_o = 18.5$ GHz. Maximum radiation angle at 26° .	117
Figure 9.12 Normalized radiation pattern measured for the co-polarization component of the antenna at $f_o = 16.2$ GHz.	118
Figure A.1 Connector of the antenna.	131
Figure B.1 Specification sheet Horn antenna.	132
Figure B.2 Specification sheet of the waveguide of the Horn antenna.	133
Figure C.1 Radiation pattern near-field, co-polarization component of the electric field at $f_o = 18.4$ GHz.	134
Figure C.2 Radiation pattern near-field, co- and cross-polarization components of the electric field at $f_o = 18.4$ GHz.	134

List of tables

Table 4.1	Field regions of an antenna [59].	57
Table 6.1	Design requirements of the HAIA.	65
Table 6.2	Properties of the materials tested.	68
Table 6.3	Design goals of the SIW H-sectoral.	73
Table 6.4	Parameters of the transition zone.	73
Table 6.5	Parameters of the coaxial probe connection.	74
Table 6.6	Parameters used in the simulations of the SIW H-plane feeding.	75
Table 6.7	Performance results of the SIW structures with coaxial probe analyzed at the maximum resonance frequency.	76
Table 6.8	Dimensions of the microstrip line.	78
Table 6.9	Parameters used in simulations for the SIW H-plane microstrip line.	79
Table 7.1	Dimensions of the holographic surface tested.	84
Table 7.2	Performance of the HAIA with variation in the holographic surface dimension at $f_o = 18.4$ GHz.	84
Table 7.3	Performances parameter of the antenna in the first operating band, simulated in the E-plane ($\phi = 0^\circ$).	89
Table 7.4	Simulation results of the frequencies in the second band, E-plane.	90
Table 7.5	Performance results of the HAIA with microstrip line at $f_o = 18.4$ GHz.	92
Table 7.6	Performance parameters of the HAIA at $f_o = 18.4$ GHz with monopole feeding.	95
Table 7.7	Performance parameters of the HAIA with monopole, size of $15.33\lambda^2$, at $f_o = 18.4$ GHz.	96
Table 7.8	Comparison of results between the modeled designs.	100
Table 7.9	Comparative results with other works.	100
Table 7.10	Performance results of the HAIA SIW H-sectoral at $f_o = 18.4$ GHz, $\theta_d = 0^\circ$ and $\theta_d = 90^\circ$.	101
Table 8.1	Performance results of the HAIA SIW H-sectoral at $f_o = 11.63$ GHz and $f_o = 14.29$ GHz.	105
Table 8.2	Parameters used in the SIW feeding in THz frequency.	108
Table 8.3	Values of the transition zone in THz frequency.	108
Table 8.4	Results of the HAIA in the first band, E-plane ($\phi = 0^\circ$), THz frequency.	111
Table 8.5	Results of the HAIA in the second band, E-plane ($\phi = 0^\circ$), THz frequency.	111
Table 9.1	Results of the measured gain in the setups used.	118
Table 9.2	Comparative results between the measured angle and simulated angle in the setups used.	119

List of Abbreviations

ADS	Advanced Design System
AIS	Artificial Impedance Surface
FEM	Finite Element Method
FNBW	First Null Beam Width
FTBR	Front-to-Back Ratio
HAIA	Holographic Artificial Impedance Antenna
HIS	High Impedance Surface
HFSS	High Frequency Structure Simulator
HPBW	Half Power Beamwidth
LWA	Leaky-Wave Antenna
MMs	Metamaterials
MTs	Metasurfaces
PBG	Photonic Bandgap
SIW	Substrate Integrated Waveguide
SSR	Split-Ring Resonators
TE	Transverse Electric mode
TM	Transverse Magnetic mode

*Man cannot discover new oceans unless he has
the courage to lose sight of the shore*

Andre Gide, .

1

Introduction

Advances in metamaterials (MMs) and metasurfaces (MTs) have allowed the exploration and development of new types of antenna systems of compact size, low cost, and high performance, due to design demands, such as low-profile, reconfigurable antennas varying the frequency, bandwidth, radiation pattern or polarization [1], as well as high gain with applications in satellites system, radars, medical images, and others. In this sense, leaky-wave antennas (LWAs) have demonstrated characteristics that make it possible to comply with the above requirements, and recently holographic artificial impedance antenna (HAIA) has been widely explored due to its uniqueness and relevant operating principle.

HAIA belongs to a group of LWAs distinguished by the conversion of a surface wave mode into a leaky-wave mode to generate frequency-controlled beam radiation in the far-field [2]. These antennas are known for their high gain, narrow beamwidth, and beam scanning capability without complex feeding network, such as phased array systems [3], and they are composed of two parts: holographic artificial impedance and a feed element launching a surface wave.

Artificial impedance surface (AIS) has been defined in the literature as two-dimensional (2-D) version of metamaterials [2], with sub-wavelength thickness known as a metasurface, which provides polarization control, phase, and amplitude of the reflected and transmitted wave. For application in antennas, D. Sievenpiper in [4] developed a method with scalar and tensor surface impedance producing linear and circular polarization, respectively, using the theory of impedance modulation [5] and the holographic principle applied in optical systems, creating a new kind of antenna with control of the desired radiation angle.

The simple design, integration, and scalability of the AIS have allowed exploring a variety of their features and optimization points for different applications, from microwave frequencies (0.3 - 300 GHz) up to the terahertz domain (0.1 - 10 THz).

The conventional HAIA design has used a monopole or dipole to generate a surface wave mode. Recently, other types of feedings as planar source

integrated directly on the dielectric substrate are of interest for a more compact design, easy integration into the holographic pattern for operation at high-frequencies [6], allowing the reduction of the antenna size without compromising its performance.

In this dissertation, it is proposed an HAIA with surface wave feeding based on the substrate integrated waveguide (SIW) technology with potential application in the X (8 - 12 GHz) and Ku (12 - 18 GHz) bands for satellites systems, as well as for operation in terahertz frequency. The HAIA is developed with scalar impedance for the excitation of a TM (Transverse Magnetic) surface wave mode, where a vertically polarized electric field is radiated far away from the antenna. Another feature explored in this kind of antenna is a change in the AIS distribution as designed in [2] to support the propagation of a TE (Transverse Electric) surface wave mode to radiate the horizontally polarized electric field.

Different parameters in the feeding and dimensions of the holographic surface are evaluated in order to understand the influence of each parameter in the performance of the antenna and to find the best results. In addition, a comparative analysis with a monopole feeding is performed to know the improvements of the HAIA. The final prototype is chosen for physical realization and measurements as a proof of concept in 18.4 GHz.

Outline of the dissertation:

- Chapter 2 presents a review of the fundamental concepts of leaky-wave and AIS;
- Chapter 3 describes the theory of LWAs and their radiation characteristics;
- Chapter 4 deals with the theory and equations that involve the holographic principle applied to antennas and the efficiency parameters in these type of structures;
- Chapter 5 provides the fundamentals of the surface wave launcher and its characteristics, as well as modeling methods;
- Chapter 6 presents a step-by-step design to model the components of the HAIA;
- Chapter 7 explores and evaluates the different characteristics and designs of the HAIA and compares its results;
- Chapter 8 develops the antenna design in the X and Ku bands, as well as in the terahertz frequency;
- Chapter 9 presents the realization of the final prototype and measurements, such as the reflection coefficient and the radiation pattern;

- Chapter 10 deals with the final comments, conclusions, and future works.

1.1 Objectives

For this project, the following objectives are defined:

- Review of the state-of-art in LWAs and the theory of impedance modulation to generate a leaky-wave mode on a surface;
- Theoretical review of the fundamental concepts that involve AIS for its understanding in antenna applications;
- Study of the SIW-H sectoral theory to model the feeding, using different types of connections and geometric structures for a comparative analysis of results;
- Comparative analysis of the antenna performance between the SIW feeding and monopole with different sizes on the holographic surface;
- Modeling of the final prototype for its manufacture and experimental tests;
- From the proof of concept manufactured for the K band, antennas operating in X and Ku bands, as well as in terahertz frequencies are developed.

1.2 Methodology of the Project

The elaboration of this project is carried out in the following stages:

- Establishment of the design goals of the surface wave feeding and the HAIA according to the performance reported in the literature for initial simulations;
- Definition of design parameters of the unit cell for the distribution of the AIS on the antenna surface;
- Definitions of the design parameters of the SIW feeding and modeling on HFSS (High-Frequency Structure Simulator);
- Realization of the AIS distribution in MATLAB to make the hologram pattern of the antenna.

Furthermore, a series of aspects of the HAIA characteristics are studied and explored, including:

- Variation of the electric permittivity and height of the dielectric substrate for modeling of the unit cell;
- HAIA feeding techniques;
- Variation of the holographic surface dimensions;
- Different distributions of the holographic pattern.

With the results, a comparative analysis of the antenna is made among the different types of feeding, dielectric substrates, and holographic surface dimensions, where the best performance is chosen to manufacture and experimentally measure it.

2

Fundamental Concepts

This chapter presents the theoretical foundations involved in this research project, starting with general concepts about the radiation properties of surface waves and leaky-waves, and their existing conditions in a waveguide plane. A background of metamaterials and state-of-art of AIS applied in antennas is reviewed.

2.1

Surface Waves

The theory that involves surface waves has more than a century of existence, beginning with the studies made by Zenneck and Sommerfeld, in 1907, over the ground propagation [7]. The antenna systems formed by metal sheets are affected by the appearance of surface waves. Furthermore, in antennas array, an unwanted mutual coupling is generated [8]. Some solutions have been employed to control them, such as AIS by altering the surface with some discontinuities to modify their electromagnetic properties [4] [8].

Surface waves are guided at an interface between two media, as illustrated in figure 2.1 and all the energy is concentrated in it ($z = 0$).

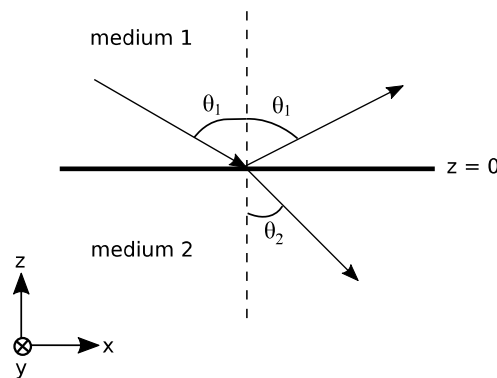


Figure 2.1: Reflection and transmission of a plane wave at an interface.

The propagation characteristic of a surface wave can be studied with the Snell's law, when the angle of incidence (θ_1) is higher than the critical (θ_c) angle [9], given by

$$\theta_1 \geq \theta_c = \sin^{-1}\left(\sqrt{\frac{\epsilon_2}{\epsilon_1}}\right), \quad (2-1)$$

where ϵ_1 and ϵ_2 are the electric permittivity in the medium 1 and 2, respectively.

When the condition in (2-1) occurs, the transmission angle (θ_2) is complex. The reflected wave decays rapidly at some wavelengths and vanishes. Thus, the surface wave propagates parallel to the interface ($z = 0$), and its velocity is slower than the speed of light (c), known as *slow wave*.

In an incidence plane (xz) without variation in the y -direction, the electric field can be polarized perpendicular (TE mode) or parallel (TM mode) to the plane of incidence. However, it is known that surface waves do not exist in the TE mode, because the energy is confined in the interface between the two media [9] [10].

By applying Maxwell's equations in the TM mode, and considering a time-harmonic convention with variation $e^{j\omega t}$, the condition of existence for the surface wave is obtained by

$$\begin{aligned} \nabla \times \mathbf{E} &= -j\omega\mu\mathbf{H}, \\ \nabla \times \mathbf{H} &= j\omega\epsilon\mathbf{E}, \\ \nabla \cdot \mathbf{D} &= 0, \\ \nabla \cdot \mathbf{H} &= 0. \end{aligned} \quad (2-2)$$

Developing equation (2-2), the expressions for the components of the electric and magnetic field are found, which are expressed by

$$\frac{\partial E_x}{\partial z} - \frac{\partial E_z}{\partial x} = -j\omega\mu H_y, \quad (2-3)$$

$$-\frac{\partial H_y}{\partial z} = j\omega\epsilon E_x, \quad (2-4)$$

$$\frac{\partial H_y}{\partial x} = j\omega\epsilon E_z, \quad (2-5)$$

where the magnetic field component in the y -direction for medium 1 ($i = 1$, $z > 0$) and for medium 2 ($i = 2$, $z < 0$) is defined by

$$H_{yi} = B_i e^{k_{zi}z - jk_{xi}x}, \quad (2-6)$$

and the components of the wave vector are expressed by

$$k_{zi}^2 + k_{xi}^2 = k_i^2. \quad (2-7)$$

When the wave propagates along the boundary, its amplitude decreases exponentially in the z -direction. Therefore k_{z1} and k_{z2} are imaginary, and they are replaced by $-jk_1$ and $-jk_2$ [11]. Thus, the components of the electric field are given by

$$\begin{aligned}
E_{x1} &= -\frac{k_1}{j\omega\epsilon_1}B_1e^{(k_1z-jk_xx)}, \\
E_{x2} &= \frac{k_2}{j\omega\epsilon_2}B_2e^{(-k_2z-jk_xx)}, \\
E_{z1} &= -\frac{k_x}{\omega\epsilon_1}B_1e^{(k_1z-jk_xx)}, \\
E_{z2} &= -\frac{k_x}{\omega\epsilon_2}B_2e^{(-k_2z-jk_xx)}.
\end{aligned} \tag{2-8}$$

For the existence of a surface wave at the interface ($z = 0$), the following condition must be satisfied

$$B_1 = B_2, \tag{2-9}$$

$$\frac{-k_1}{\epsilon_1} = \frac{k_2}{\epsilon_2}. \tag{2-10}$$

The condition in (2-10) defines that k_1 and k_2 are both positive values, where ϵ_1 or ϵ_2 must have a negative value. Usually, negative electric permittivity is found in metals such as copper, which demonstrate its existence in this type of materials. With the condition in (2-7), a relationship between k_x and w is obtained by

$$k_x = \frac{\omega}{c} \sqrt{\frac{\epsilon_1\epsilon_2}{\epsilon_1 + \epsilon_2}}. \tag{2-11}$$

When the wave propagates along the interface, k_x must be real, where $\epsilon_1\epsilon_2 < 0$ and $\epsilon_1 + \epsilon_2 < 0$.

2.2

Leaky-Waves

Leaky-wave is a kind of traveling wave with an increase of energy in the transverse direction from a guide structure. Pioneer studies carried out by A. A. Oliner, in 1959, [5] allowed a mathematical comprehension about the behavior of leaky-waves, demonstrating its existence, being of great benefit for different applications, such as antennas, optical surface wave prism and grid couplers [12].

A leaky-wave is composed of a phase constant (β) in rad/m, and attenuation constant (α) in Np/m, being constant along the waveguide if the structure is uniform. For the existence of a leaky-wave, a closed waveguide with some slots or discontinuities is needed to produce the leakage energy, which contributes significantly to the radiation pattern. A detailed description will be presented in Chapter 3.

2.3

Background of Metamaterials

The study field of metamaterials start with the first publication made by the Russian physicist Victor Vesalago in 1968 [13], where it was presented

a theoretical possibility of modeling negatives electromagnetic parameters (electric permittivity and magnetic permeability) simultaneously. Also, he predicted that some electromagnetic phenomena, such as Snell's law, the Doppler effect, Vavilov-Cherenkov radiation, and others would be reversed, including the anti-parallel behavior of the wave vector [14]. However, due to the lack of available materials with such features and the computational capability of its time, the theory could not be tested experimentally. It was until the 1990s, when the physicist John Pendry generated a broad interest in the scientific community with the construction of the first metamaterial [15]. Periodic split ring resonators (SSRs) defined as a unit cell were used to create a particular magnetic response due to the effect LC modeled in the SSRs, producing a negative magnetic permeability ($\mu < 0$). Also, a conducting wire was used to provide the negative electric permittivity ($\epsilon < 0$) in a given frequency range. Figure 2.2 shows an example of the first metamaterial built.

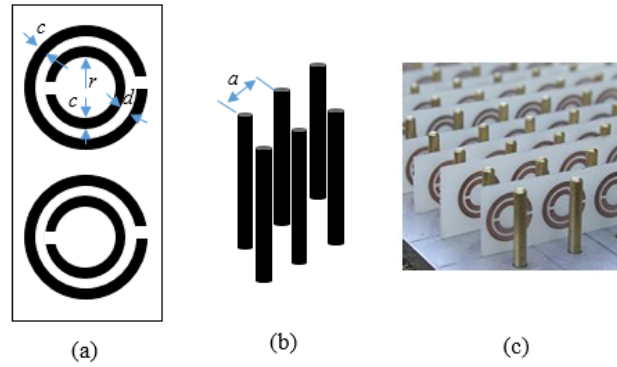


Figure 2.2: Structure of a metamaterial with properties: (a) negative magnetic permeability, (b) negative electric permittivity, and (c) realization of metamaterial with refractive negative index [15].

In 2005, an experimental realization of a gradient index lens to bend electromagnetic waves was reported [16], introducing the concept of negative refractive index as illustrated in figure 2.3.

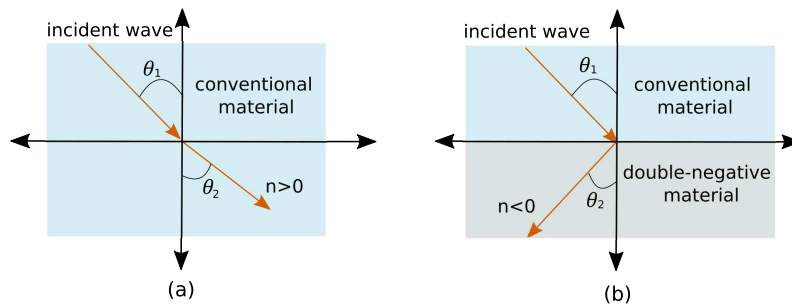


Figure 2.3: Effect of the Snell's law in: (a) conventional material, and (b) double-negative material.

There have been many contributions and experiments about the potential of metamaterials in the field of the optic, photonic, medicine, wireless power transmission (WPT), and others. However, one of its difficulties have been to define a universal concept to know what can be considered a metamaterial, perhaps by the different points of view of researchers to clearly define their most essential properties and features [17].

One of the first concepts of metamaterials commonly cited in the literature is: "artificial material with properties not found in the nature" [18], where the Greek word *meta* was associated by its meaning *beyond* the physical, and the term *artificial* is related to its geometry, not its chemistry control the electromagnetic response of the material. Usually, the metamaterials are made of metals and dielectrics.

A second published definition of metamaterial is: "artificial three-dimensional (3-D) periodic structure much smaller than the wavelength of interest, where its electromagnetic properties such as permittivity and permeability can be controlled" [11]. Another metamaterial concept is: "artificially structured materials that are designed to interact with electromagnetic waves and control them" [19].

The interaction of the electromagnetic wave with the metamaterial has been studied with the effective medium theory, which requires that the unit cell size must be much smaller than the operating wavelength, with the purpose to be modeled as atoms and molecules of conventional materials on a large scale. If the structure is bigger than the subwavelength, the radiation would be diffracted or refracted [20] without interaction with the medium. A generalized theory of metamaterials is described below. Applying Maxwell's equations in the time-harmonic form:

$$\begin{aligned}\nabla \times \mathbf{E} &= -j\omega\mu\mathbf{H}, \\ \nabla \times \mathbf{H} &= j\omega\epsilon\mathbf{E}.\end{aligned}\tag{2-12}$$

when the electric permittivity (ϵ) and the magnetic permeability (μ) are negative, equation (2-12) changes to

$$\begin{aligned}\nabla \times \mathbf{E} &= -j\omega(-\mu)\mathbf{H} \longrightarrow \nabla \times \mathbf{E} = -j\omega\mu(-\mathbf{H}), \\ \nabla \times \mathbf{H} &= j\omega(-\epsilon)\mathbf{E} \longrightarrow \nabla \times -\mathbf{H} = j\omega(\epsilon)\mathbf{E}.\end{aligned}\tag{2-13}$$

forming a left-handed triplet system of vectors [13], expressed by

$$\begin{aligned}\mathbf{k} &\perp \mathbf{E} \perp (-\mathbf{H}), \\ -\mathbf{k} &\perp \mathbf{E} \perp \mathbf{H}.\end{aligned}\tag{2-14}$$

There is a category of metamaterials that classifies them according to the electromagnetic parameters that define materials: electric permittivity (ϵ) and magnetic permeability (μ), as shown in figure 2.4. Usually, the materials

have positive values of ϵ and μ called double-positive, where the vector fields \mathbf{E} and \mathbf{H} , as well as the propagation constant (k) and the Poynting vector (\mathbf{S}) present the conventional behavior. In the case of ϵ or μ negative, the materials are called *epsilon-negative* or *mu-negative* or electric and magnetic plasma, respectively, that support evanescent waves. When the two parameters are negatives, the material is called double-negative, and the direction of the propagation constant is inverted.

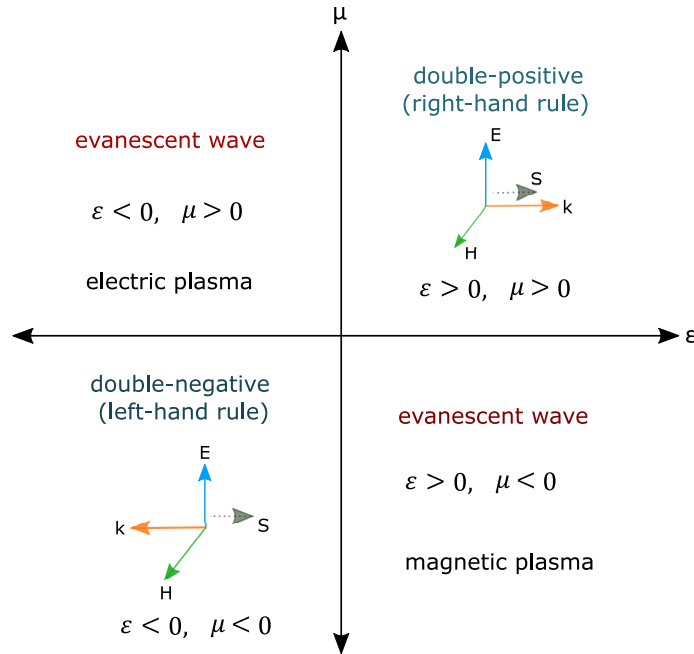


Figure 2.4: Categories of metamaterials based on their effective properties.

2.4

State-of-art: Artificial Impedance Surface

AIS began to be studied as photonic band gap (PBG) structures in one, two, or three periodic dimensions as illustrated in figure 2.5, known as a photonic crystal, composed of periodic dielectrics [21]. The behavior of the structure is studied with the Bloch's theorem that establishes the field inside the photonic crystal takes its symmetry and periodicity.

In 1999, D. Sievenpiper [8] published a pioneer work to model a corrugated high impedance surface (HIS), which shows that if a conductor is engineered with a certain geometric periodicity, it is possible to control the effective properties of the surface impedance with extremely high surface impedance values ($Z_s \gg Z_o$) in certain frequency range. The proposed structure in [8] is formed by a metal-dielectric substrate, where the dielectric substrate can include vias or not. Nowadays, different design approaches have been developed for these artificial impedance surfaces.

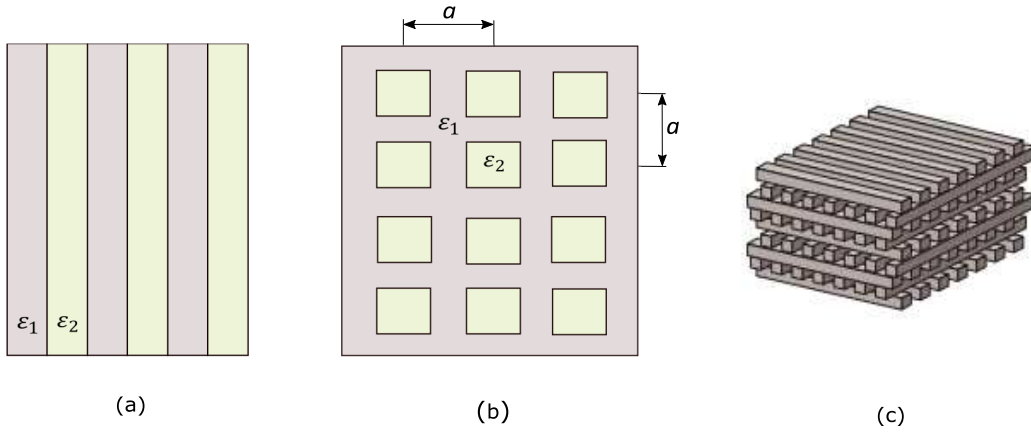


Figure 2.5: Examples of photonic crystals periodic in: (a) 1-D, (b) 2-D, and (c) 3-D.

When the surface impedance (Z_s) is high, it means that the surface has a particular texture able to provide greater control over the electric field due to its boundary condition. The surface impedance is represented as the ratio between the electric field and the magnetic field on the surface, which is defined in equation (2-15) for a plane yz . Thus, with the modeling of the surface impedance, the response of the electric field can be controlled.

$$Z_s = \frac{E_z}{H_y}. \quad (2-15)$$

Figure 2.6 shows the well-known AIS *Sievenpiper mushroom*, which consists of a metallic patch connected to a ground plane with vertical vias. The geometry of the unit cell was designed to provide the effect of a resonant LC circuit. The patch element behaves as capacitance and the conducting vias as an inductance.

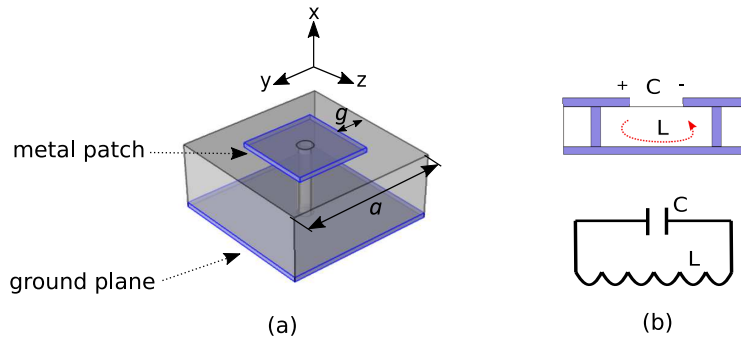


Figure 2.6: Sievenpiper mushroom surface: (a) unit cell, and (b) equivalent circuit.

The surface impedance of the unit cell is given by

$$Z_s = j \frac{\omega L}{1 - \omega^2 LC}, \quad (2-16)$$

and its resonant frequency is expressed by

$$\omega = \frac{1}{\sqrt{LC}}. \quad (2-17)$$

Consequently, these surfaces impedances have been defined in the literature as *metasurfaces*, regarded as a two-dimensional (2-D) version of metamaterials [2], [22] governed by the effective surface properties [23]. Thus, for metasurfaces, aspects such as amplitude, phase, and polarization response are the focus of interest, instead of permittivity, permeability, or refractive index control as in the case of metamaterials. Many applications using metasurfaces for polarization control and wavefront shaping have been rapidly elaborated due to their simple fabrication process compared to metamaterials [23].

As in the case of metamaterials, a metasurface requires that the surface must be much smaller than the wavelength to use the effective medium model as explained above. Another study in metasurfaces include the electrical tunability of the impedance by microelectronic technology to control the voltage and thus the surface impedance [24].

For many years, the presence of electric conductors and surface waves in devices such as reflector antennas have degraded its performance due to the phase shift between the reflected and transmitted wave in metal sheets or the ground planes, which causes destructive interference, as illustrated in figure 2.7. For example, when a dipole antenna is placed near the conductive surface, it requires a minimum distance of $\lambda/4$ to avoid the phase shift. However, this means less compact devices.

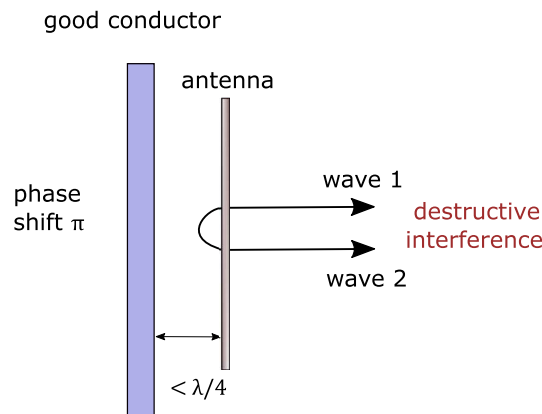


Figure 2.7: Reflection and transmission of a plane wave in an interface with metal conductor [8].

The inconvenient of phase shift was solved using a periodic array of Sievenpiper mushroom unit cell, as illustrated in figure 2.8. The high impedance reflects the wave in phase with constructive interference that makes it behave as artificial magnetic conductor (AMC). Surface impedance supports

the propagation of a TM surface wave mode with the magnetic field transverse to the propagation direction of the surface wave and a TE surface wave mode with the electric field transverse to the propagation direction. If a surface wave propagates in the $+z$ -direction, the field has a decrease in the x -axis as is exhibited in figure 2.9.

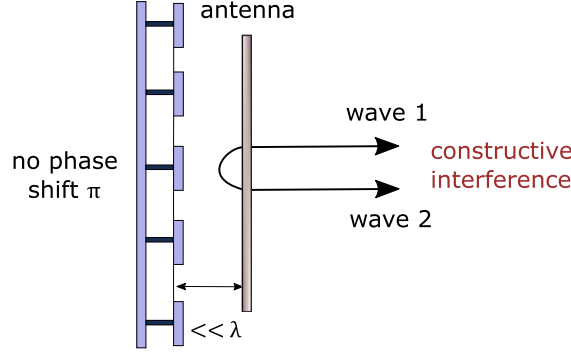


Figure 2.8: Reflection and transmission of a plane wave in an interface with AIS [8].

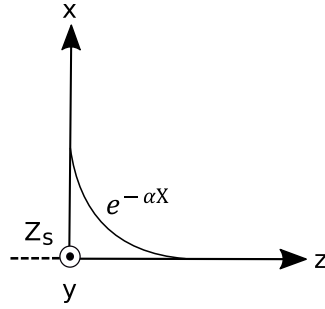


Figure 2.9: Propagation of a surface wave on a impedance surface [8].

The components of the electric and magnetic field are expressed by $H_x = H_z = E_y = 0$ for a TM surface wave mode. The z -component of the electric field with decay constant (α) and propagation constant (k) is given by

$$E_z = C e^{-jkz - \alpha x}. \quad (2-18)$$

The component of the magnetic field in the y -direction can be deduced from the Ampere-Maxwell law in the time-harmonic form:

$$\nabla \times \mathbf{H} = j\omega\epsilon\mathbf{E}, \quad (2-19)$$

and can be reduced to

$$\frac{\partial H_y}{\partial x} = j\omega\epsilon E_z, \quad (2-20)$$

where, by integrating both sides of equation (2-20), H_y is given by

$$H_y = \frac{-j\omega\epsilon}{\alpha} C e^{(-jkz - \alpha x)}. \quad (2-21)$$

By substituting (2-18) and (2-21) into (2-15), the impedance of a TM mode can be written as follows

$$Z_{s(TM)} = \frac{j\alpha}{\omega\epsilon}. \quad (2-22)$$

To determine the impedance in TE mode, assuming that the electric field is transverse to the surface and $H_x = H_y = E_z = 0$. The magnetic field in the z -component is given by

$$H_z = Ce^{-jkz - \alpha x}. \quad (2-23)$$

The component of the electric field in the y -direction can be deduced from the Faraday's law in the form time-harmonic, defined by

$$\nabla \times \mathbf{E} = -j\omega\mu\mathbf{H}, \quad (2-24)$$

$$\frac{\partial E_y}{\partial x} = -j\omega\mu H_z, \quad (2-25)$$

where, by integrating both sides of the equation (2-25), E_y is given by

$$E_y = \frac{j\omega\mu}{\alpha} Ce^{-jkz - \alpha x}. \quad (2-26)$$

For a TE mode, the correct expression contains a negative sign, which is expressed by

$$Z_{s(TE)} = -\frac{E_y}{H_z}. \quad (2-27)$$

Therefore, the impedance surface for a TE mode is given below

$$Z_{s(TE)} = \frac{-j\omega\mu}{\alpha}. \quad (2-28)$$

The imaginary value of Z_s represents the reactive part of the impedance, capacitive or inductive. From equation (2-22) and (2-27), it is seen that TM surface wave has a positive impedance associated with an inductive surface, and TE surface wave has a negative impedance attributed to a capacitive surface [8].

2.5

Scalar and Tensor Surface Impedance

AIS uses a periodic array of geometries with dimensions smaller than the operating wavelength. Due to this periodicity, its analysis can be characterized with a single unit cell of lattice dimension a and gap g formed by an arbitrary metal patch on a dielectric substrate of height h connected to a ground plane, as illustrated in figure 2.10, producing a capacitive impedance [25]. Depending on the geometry of the metal patch, the surface impedance can be scalar or

tensorial according to the relationship between the electric field and the surface current in the structure.

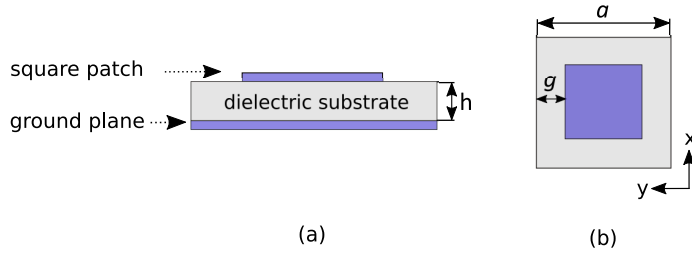


Figure 2.10: Example of a AIS unit cell for application in antennas: (a) frontal view, and (b) top view.

2.5.1

Scalar AIS

Scalar AIS emerges to control the propagation of the electric field through the modeling of an isotropic surface impedance. The impedance boundary condition is given by

$$\mathbf{E} = Z_s \mathbf{J}, \quad (2-29)$$

where J is the surface current and Z_s is the surface impedance. A scalar impedance can support the propagation of either a TM or TE surface wave mode by the unit cell characterization [26] with linear polarization for antenna applications. In the TM mode, the electric field is oriented vertically to the surface without the existence of magnetic surface wave mode. In the TE mode, the electric field is oriented horizontally [2], as illustrated in figure 2.11.

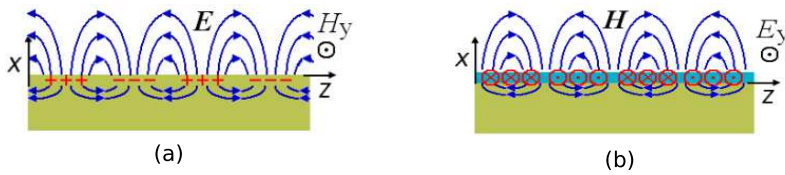


Figure 2.11: Schematic propagation of the surface wave mode: (a) TM-polarization, and (b) TE-polarization [27].

Therefore, the type of propagation of the surface wave mode defines the polarization of the radiated wave in the HAIA, either vertically or horizontally polarized electric fields [2]. The TM guided mode is considered in this dissertation for its application in antennas [5].

The electromagnetic field of the unit cell can be solved using an analytical model as presented in [28] and [29] with a transmission line approach or with a commercial full-wave electromagnetic simulation [4], such as HFSS, where it

has different solvers solution that can be used. Some geometry shapes, such as square, triangles, and circles, behave as scalar impedance. In this work, these geometries are setup on HFSS using a Driven Modal solution with a wave port excitation in the $+x$ -direction to obtain the magnitude of the electric field (V/m) and the surface current vector (A/m) presented in figure 2.12 and 2.13, respectively. The lattice a and gap g of the unit cell were kept constant ($a = 3$ mm, $g = 0.2$ mm). It is noted that the surface current vector follows the same direction of the polarization of the incident wave.

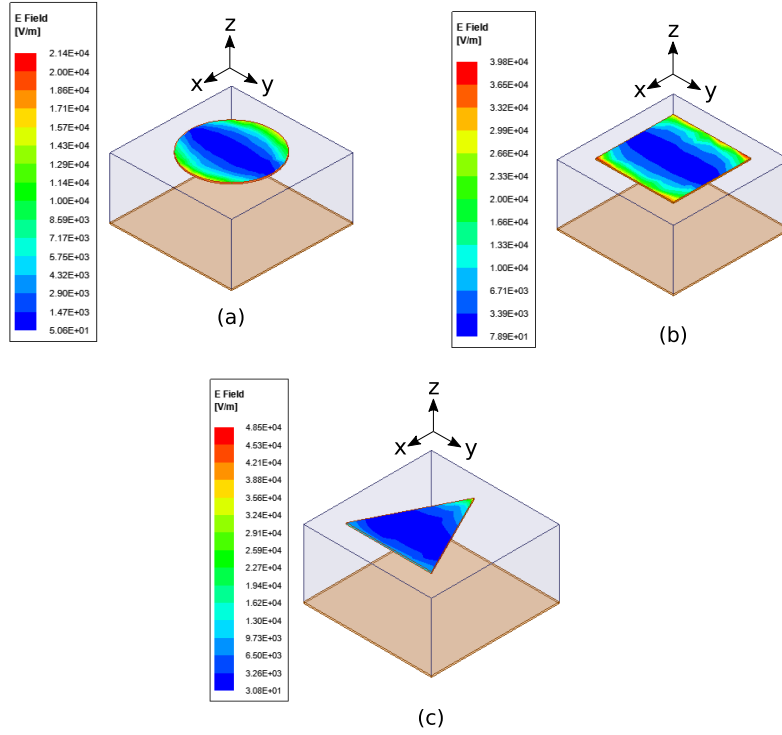


Figure 2.12: Magnitude of the electric field in V/m of the evaluated geometries: (a) circular unit cell, (b) square unit cell, and (c) triangle unit cell.

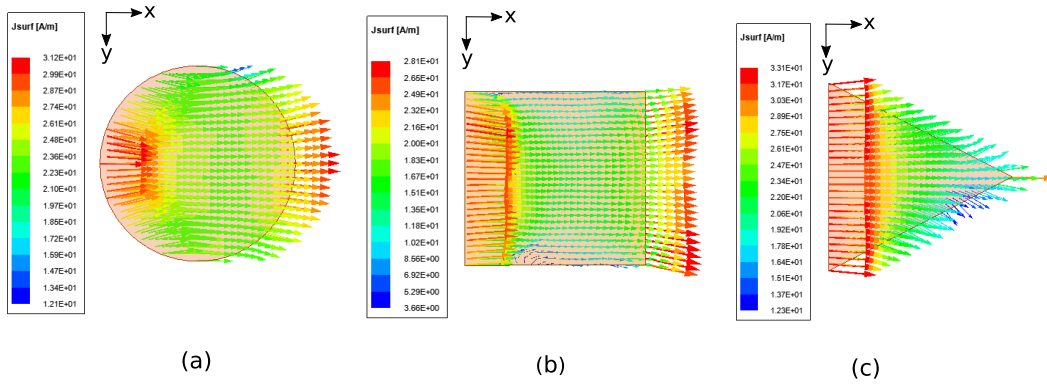


Figure 2.13: Surface current vector in A/m of the evaluated geometries: (a) circular unit cell, (b) square unit cell, and (c) triangle unit cell.

Figure 2.14 shows the phase of the reflection coefficient of the geometries studied. The phase decreases with increasing frequency. The behavior response can be controlled by modifying the lattice dimension of the unit cell or the gap value to obtain higher resonance frequencies.

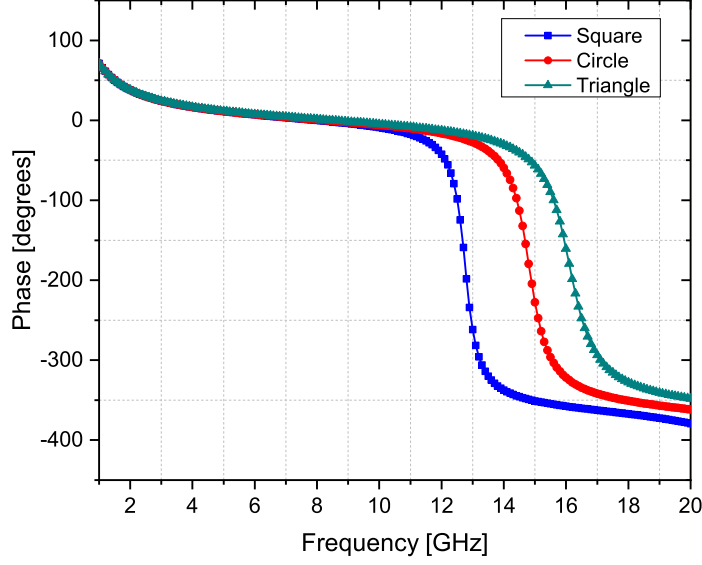


Figure 2.14: Phase of the reflection coefficient of the evaluated geometries.

2.5.2

Tensor Surface Impedance

Tensor surface impedance is an anisotropic impedance able of producing a circular polarization that supports both modes TE and TM [2], with direction-dependent impedance properties represented by a tensor 2x2 for a surface on the plane xy [4], defined as

$$Z_s = \begin{pmatrix} Z_{xx} & Z_{xy} \\ Z_{yx} & Z_{yy} \end{pmatrix}, \quad (2-30)$$

where the values of the tensor are imaginary impedances with the condition $Z_{xy}=Z_{yx}$. The boundary condition on the surface is expressed by

$$\mathbf{E} = \bar{\bar{Z}}_s \hat{\mathbf{z}} \times \mathbf{H}, \quad (2-31)$$

$$\mathbf{E} = \bar{\bar{Z}}_s \mathbf{J}. \quad (2-32)$$

Thus, the relationship of the surface impedance and the surface current can be expanded as represented in equation (2-33).

$$\begin{pmatrix} E_x \\ E_y \end{pmatrix} = \begin{pmatrix} Z_{xx} & Z_{xy} \\ Z_{yx} & Z_{yy} \end{pmatrix} \begin{pmatrix} J_x \\ J_y \end{pmatrix}. \quad (2-33)$$

Some geometric shapes, such as a rectangle, an ellipse, and a square sliced gap behave as a tensorial impedance, as can be seen in figure 2.15.

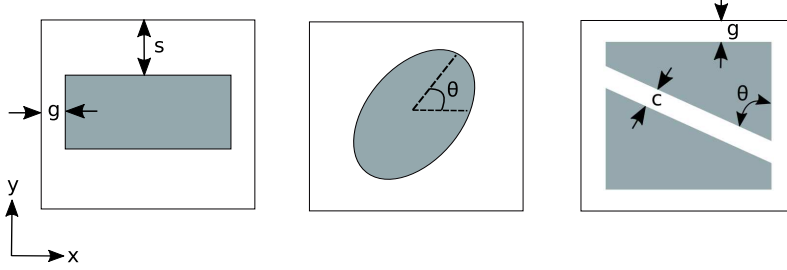


Figure 2.15: Examples of AIS unit cell with tensorial impedance.

Tensor AIS modeling methods are proposed in [4], [29] and [30], where the characterization of the electric field in the geometric pattern is performed to solve the tensor impedance. However, its characterization still has challenges due to the calculation of the tensor impedance in Z_{xx} , Z_{xy} , Z_{yx} , Z_{yy} and the surface distribution in the antenna. Figure 2.16 shows an example of a holographic surface with square slice gap able of producing a circular polarization. Some studies have developed alternative methods using scalar impedances with spiral modulation [31].

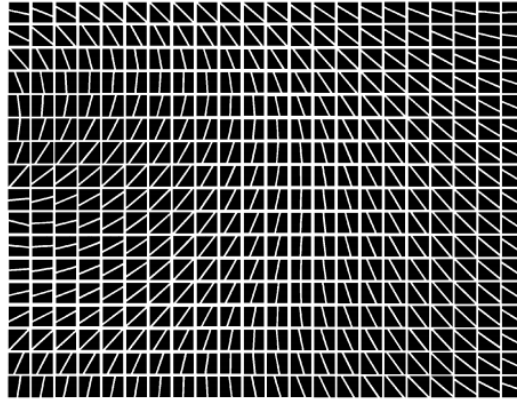


Figure 2.16: Example of a tensor impedance distribution using square sliced gap unit cell [4].

3

Fundamental Theory of Leaky-Wave Antennas

In this chapter, a theoretical review of LWAs is presented to study their features, operation principles, and design approaches. A series of equations that explain the physical behavior of the leakage energy are studied to produce the conversion of a surface wave into a leaky-wave.

3.1

Approaches of LWAs Design

The study field of LWAs is extensive and contributions around the world on this topic increase with each passing day due to its interesting operation principle. Its unique radiation characteristics allow the design of a compact structure, with high gain, narrow beam, and beam scanning without the employment of complex feed network as a phased array system.

LWA is a kind of scannable and traveling wave antenna [32]. The direction of radiation can be controlled electronically with active devices or frequency variation [33]. A diagram of dispersion is shown in figure 3.1, where is presented the existence condition for the forward radiation (region I and II) and backward radiation (region III and IV). The maximum beam angle can be controlled from near backfire to near endfire. Typically, LWAs have been restricted with a scan range of 5° to 80° in the forward radiation region [34].

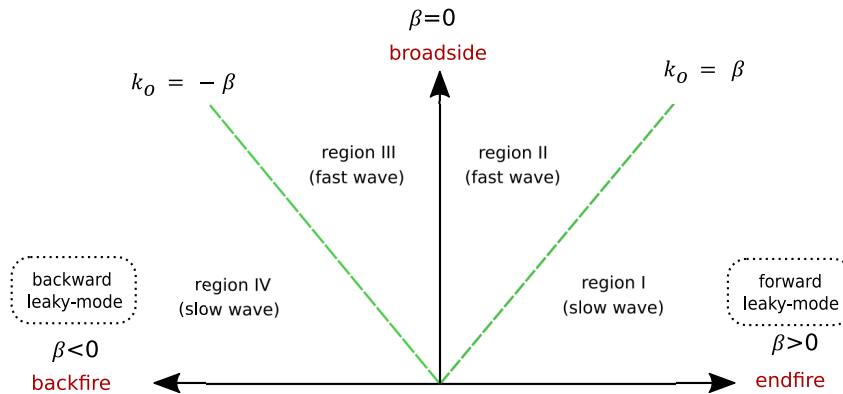


Figure 3.1: Dispersion diagram of the condition for the backward and forward radiation of an LWA.

LWAs are generally categorized as uniform and periodic structures for the conversion of a surface wave mode into a leaky-wave mode. The operating

principles of the two structures are similar. However, the features of each design technique vary their regions of scanning angle. For a uniform LWA, radiation is only possible in the forward region, different to the periodic LWA where there may be radiation from the backward to the forward region. A description of the physical behavior of both design approaches is explained in detail in the following sections.

3.2

Uniform LWA

The radiation characteristic in a uniform LWA was studied analytically, in 1959, by L. O. Goldstone and A. A. Oliner in rectangular [35] and circular [36] waveguide with a slot in one of its walls as shown in figure 3.2, being the simplest design to produce the effect of leakage energy. Later, other ideas were incorporated as multi-layered dielectric [37] and metal strips on a dielectric waveguide [38].

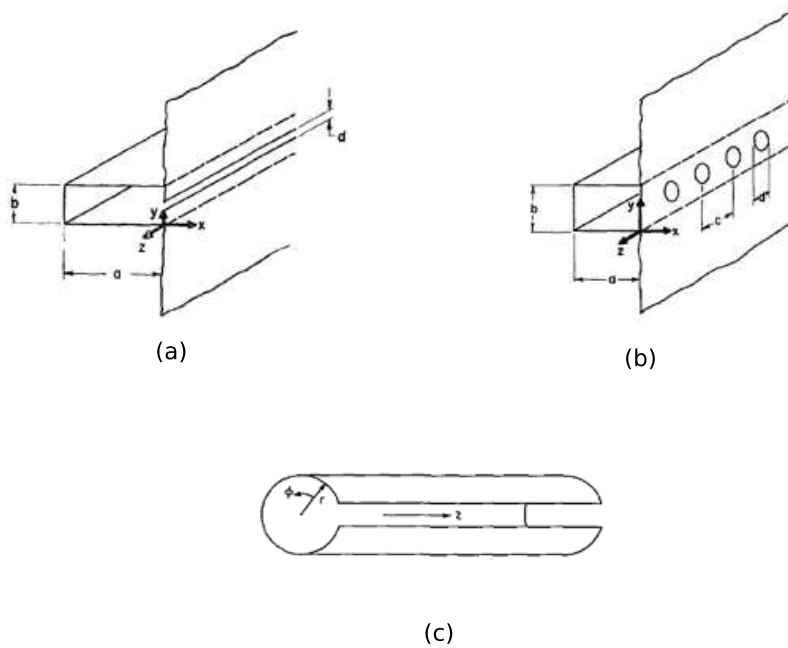


Figure 3.2: Illustration of a uniform LWA: (a) rectangular waveguide with a continuous slot [35], (b) rectangular waveguide with circular slots, and (c) circular waveguide with a continuous slot [36].

An example of the radiation mechanism of a uniform LWA is shown in figure 3.3, where k_z and k_x are the longitudinal and transverse wavenumbers, respectively. The propagation constant is invariant along the waveguide surface due to its uniform aperture.

The component of the electric field in the y -direction ($x = 0$) is given by

$$E_y(0, z) = Ae^{-jk_z z}, \quad (3-1)$$

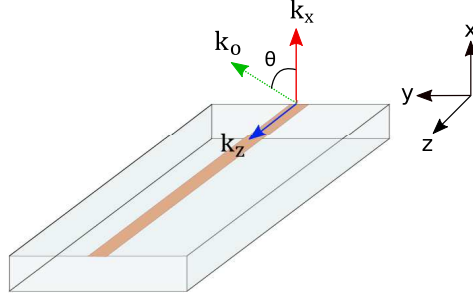


Figure 3.3: Uniform LWA in the form of a rectangular waveguide with a continuous aperture slot in the top wall for the leakage energy.

where k_z is the wavenumber of the leaky-wave, which is expressed by

$$k_z = \beta - j\alpha, \quad (3-2)$$

being β the phase constant (or phase delay), and α is the attenuation constant. In an LWA, α represents the losses due to the leakage energy along the waveguide. Both constant parameters establish the radiation condition that defines whether a wave is propagating ($\beta > 0$ and $\alpha > 0$) or evanescent ($\beta < 0$ and $\alpha < 0$).

So, to explain the fundamental electromagnetic behavior of a leaky-wave, only the real part of k_z will be considered [8]. In the region $x > 0$, the electric field E_y is given by

$$E_y(x, z) = e^{-jk_z z} e^{-jk_x x}. \quad (3-3)$$

The phase vector has the following expression

$$\beta = \beta_x \hat{x} + \beta_z \hat{z} = \text{Re}(k_x \hat{x} + k_z \hat{z}), \quad (3-4)$$

where $k_z = \beta$ and, thus, the equation (3-3) is transformed into

$$E_y(x, z) = e^{-j\beta z} e^{-j\sqrt{k_o^2 - \beta^2} x}. \quad (3-5)$$

where k_o is the free-space wavenumber denoted by $k_o = \sqrt{k_x^2 + k_z^2}$. Thus, equation (3-5) gives the radiation conditions of a leaky-wave: when $\beta < k_o$, the term $\sqrt{k_o^2 - \beta^2}$ is real and the wave propagates in the z -direction, known as *fast wave*, equivalent to the phase velocity higher than the speed of light in vacuum ($v_p > c$). When $\beta > k_o$, the term $\sqrt{k_o^2 - \beta^2}$ is complex, transforming the propagating wave into an evanescent wave, thus the phase velocity is lower than the speed of light in vacuum ($v_p < c$), known as *slow wave*. In the case of a fast wave where there is radiation along z -direction, the radiated field is characterized using the *Helmholtz* equation by the transverse wavenumber, expressed by

$$k_x = \sqrt{k_o^2 - k_z^2} = \beta_x - j\alpha_x. \quad (3-6)$$

From equation (3-6) is obtained the following condition:

$$\beta\alpha = -\beta_x\alpha_x. \quad (3-7)$$

In the forward leaky-mode ($\beta > 0$), the attenuation constant must be $\alpha_x < 0$. Negative values of α_x imply an exponential increase of the wave when it is propagating in the x -direction. Therefore, there is an increase of the wave along $+z$ -direction and attenuation along x -direction [39] as illustrated in figure 3.4, and in free-space, this behavior is considered in opposition to the conventional radiation condition for the solution of Helmholtz equation. It has a nonphysical characteristic described as improper wave [35]. However, its radiation condition can be studied with a ray diagram, which shows consistency with equation (3-7) [39]. Besides, the theoretical understanding described in the work of A. A Oliner [5] allowed to solve the problem of the physical comprehension of leaky-wave behavior.

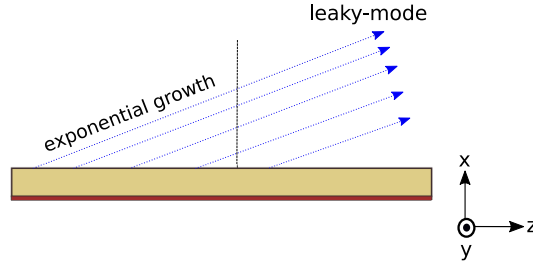


Figure 3.4: Ray diagram of power flow in free-space with exponential growth [39].

For backward leaky-mode ($\beta < 0$), which means that the phase velocity and group velocity are in opposite directions, the direction of the power flow is in the negative z -direction, with positive values of the attenuation constant ($\alpha_x > 0$). In this case, the fields decay exponentially in the x -direction with proper physical behavior as illustrated in figure 3.5.

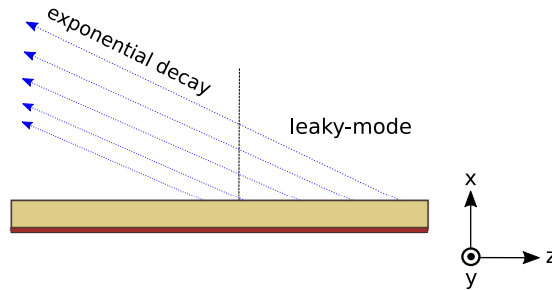


Figure 3.5: Ray diagram of power flow in free-space with exponential decay [39].

The fundamental mode in a uniform LWA is a fast wave with $\frac{\beta}{k_o} > 1$, which is expressed by

$$\frac{\beta}{k_o} = \sqrt{1 - \left(\frac{\pi}{k_o a}\right)^2}. \quad (3-8)$$

3.3 Periodic LWA

Closed waveguides in millimeter waves have an inefficient performance due to high losses. For this reason, an open waveguide is used, such as microstrip line, dielectric guide, and others [40]. However, open waveguides support the propagation of slow waves, where the dominant mode is bound on the surface. Therefore, to produce a fast wave, some surface alterations are necessary with periodic discontinuities (a) as illustrated in figure 3.6.

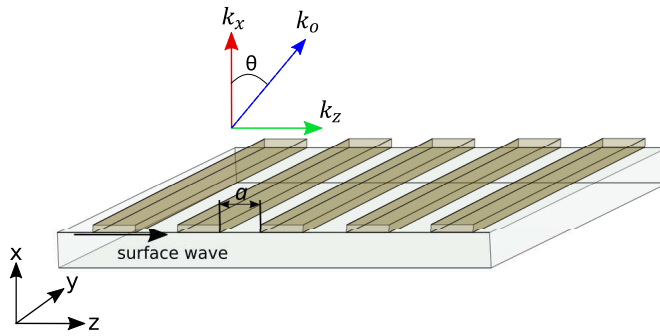


Figure 3.6: Example of an open waveguide with periodic discontinuities on the surface.

When those discontinuities are added, a set of space harmonics ($n = 0, \pm 1, \pm 2, \dots$) is generated, which are defined by

$$\beta_n = \beta + \frac{2\pi n}{a}, \quad (3-9)$$

where β is the fundamental phase constant, as in the case of a uniform LWA. Thus, the transverse wavenumber is transformed into

$$k_x = \sqrt{k_o^2 - \beta_n^2}. \quad (3-10)$$

The fast wave in free-space is obtained when k_x is real positive, and established by

$$\beta + \frac{2\pi n}{a} < k_o. \quad (3-11)$$

The condition in (3-11) is fulfilled when the space harmonics are negative. Also, it is desirable that there is only one radiated mode for the reduction of side lobes. Usually, the $n = -1$ mode is chosen to achieve radiation in a specified direction for a single main beam radiation [41]. The presence of other modes can be avoided with the appropriate value of the period a and, therefore, to ensure the propagation of only the first harmonic: $\beta_{-1} = \beta - \frac{2\pi}{a}$.

Figure 3.7 shows the behavior of the frequency and the phase constant in a conventional rectangular waveguide. There is a radiation cone between the short dash red line (k_o and $-k_o$), which represents the limits for the existence of free-space propagation: $-k_o < \beta_{-1} < k_o$. The solid blue line (k_1) represents the propagation constant in the dielectric medium of the waveguide. Inside of the radiation cone, there are the regions for the existence of forward and backward waves. The existence of the mode $n = -2$ has the condition: $\beta_{-2} = \beta_{-1} - \frac{2\pi}{a} < -k_o$ [41].

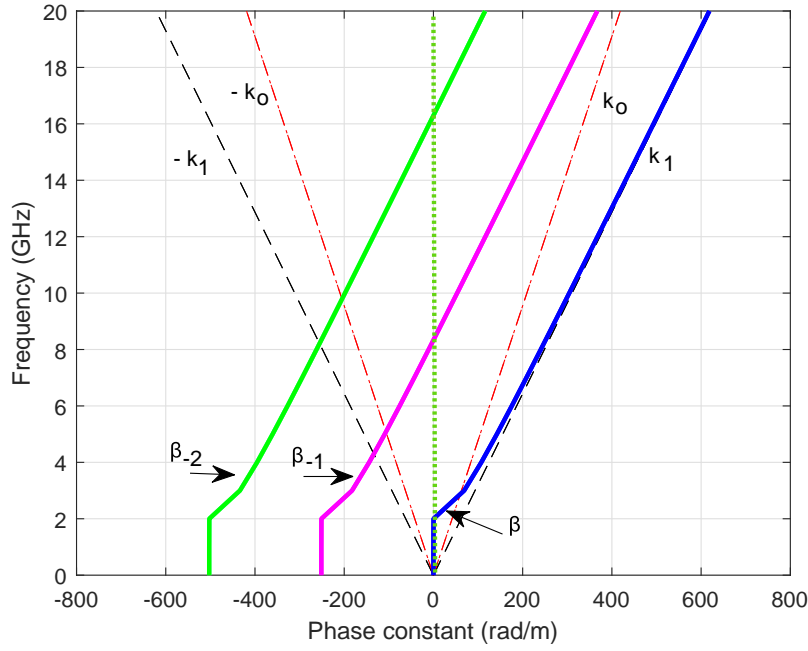


Figure 3.7: Dispersion diagram in a conventional rectangular waveguide.

3.4

Modulation of the Surface Impedance

As presented in the previous section, the behavior of the leaky-wave depends on the frequency and periodicity of the discontinuities on the surface. Therefore, to create the leakage energy is necessary a periodic modulation of length a in the direction of propagation, in one (1-D) or two (2-D) dimension, known as *modulation of the surface impedance*, where the dominant mode is a non-radiant slow wave, and with the modulation, the space harmonics can be radiated.

Modulation of the surface impedance is a theory with more than 50 years of existence, and it was reported for the first time by Thomas and Zucker in 1959 [42], which demonstrates that modulating the phase velocity or amplitude of the surface wave, a leaky-mode is generated and radiated at a specific angle.

However, an analytical comprehension about its effect was not possible until 1963, where A. A. Oliner and A. Hessel developed a numerical solution in [5] for the conversion of a surface wave mode into a leaky-wave mode using a surface texture with variation in the periodic modulation.

The physical behavior of the leakage energy in the modulation of the surface impedance has the fundamental mechanism of uniform LWAs, explained below. The analysis is performed using a sinusoidal modulation for the distribution of the surface impedance made in one-dimension (1-D) [5].

If the propagation direction of the leaky-wave is along the z -axis as illustrated in figure 3.8, the impedance on the surface is defined by

$$Z_s(z) = X_s[1 + M\cos(\frac{2\pi z}{a})], \quad (3-12)$$

where X_s is the average value of the impedance surface, M is the modulation factor, and a is the period of the sinusoidal modulation.

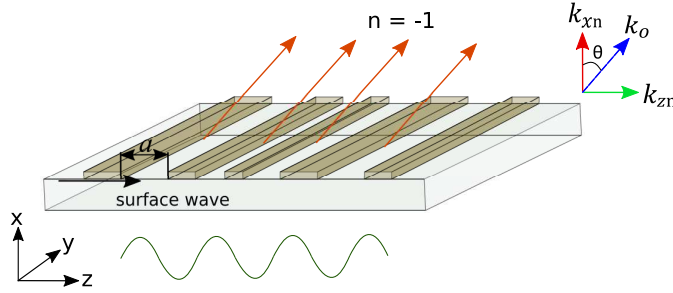


Figure 3.8: Sinusoidal modulation in one-dimension (1-D) of the surface impedance and its propagation constants.

Thus, as the geometric pattern is periodic, the electric and magnetic fields are also periodic, represented as an infinite sum of modes called Floquet modes, and with the modulation effect, some of these modes will be radiated [5].

The propagation constant on the surface of each Floquet mode (k_{xn}) is defined by equation (3-13) for the different harmonic spaces $n = 0, \pm 1, \pm 2 \dots$ [43], which are represented by

$$k_{xn} = \sqrt{k_o^2 - (k + \frac{2\pi n}{a})^2}, \quad (3-13)$$

where k_o is the propagation constant in the free-space and k is the fundamental wavenumber on the surface when $n = 0$ ($k_{z0} = k = \beta + j\alpha$). The phase constant along the surface is associated to the surface impedance [2]. The n th spatial harmonic is expressed by

$$k_{zn} = k + \frac{2\pi n}{a}. \quad (3-14)$$

The variation of the period a directly affects the fundamental wavenumber. Therefore, the phase constant varies along the surface. In [5], an analyti-

cal solution was defined to determine the variation of k for different values of X_s , M , and a , being a fundamental solution for the conversion of surface waves into leaky-waves, presented below

$$1 - \frac{j}{X_s} \sqrt{1 - \left[\frac{k}{k_o} + \frac{2\pi n}{ka} \right]^2} = \frac{M^2/4}{1 - \frac{j}{X_s} \sqrt{1 - \left[\frac{k}{k_o} + \frac{2\pi(n-1)}{ka} \right]^2}} - \frac{M^2/4}{1 - \frac{j}{X_s} \sqrt{1 - \left[\frac{k}{k_o} + \frac{2\pi(n-2)}{ka} \right]^2}} - \frac{M^2/4}{1 - \frac{j}{X_s} \sqrt{1 - \left[\frac{k}{k_o} + \frac{2\pi(n+1)}{ka} \right]^2}} - \frac{M^2/4}{1 - \frac{j}{X_s} \sqrt{1 - \left[\frac{k}{k_o} + \frac{2\pi(n+2)}{ka} \right]^2}} \dots \quad (3-15)$$

A good approximation of equation (3-15) is obtained with the mode $n = 0$ and $n = -1$, which shows that the radiation occurs through the mode $n = -1$ [44]. Therefore, a diagram of dispersion can be performed using equation (3-15) solving numerically for k , as illustrated in figure 3.9.

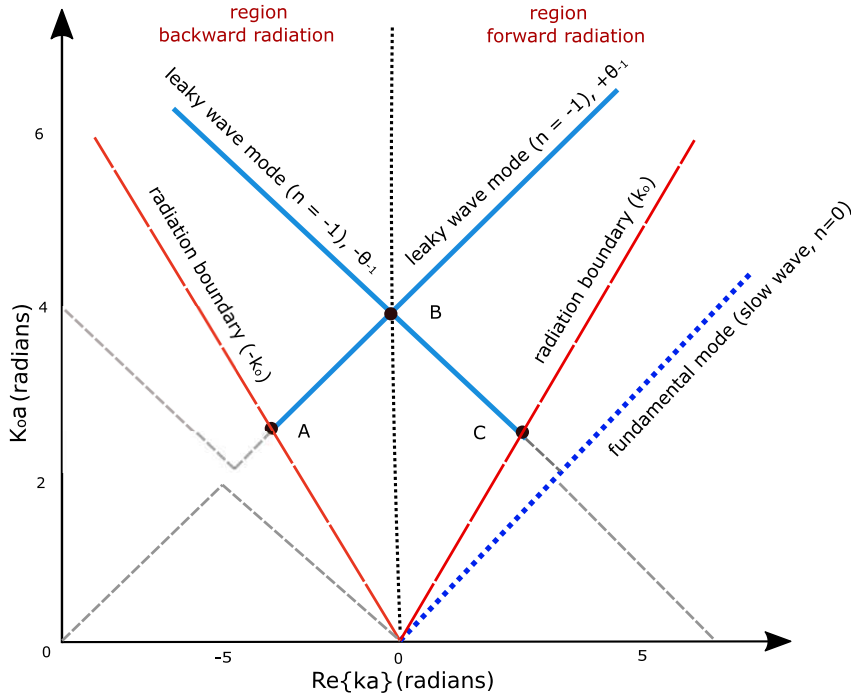


Figure 3.9: Illustration of forward and backward leaky-wave modes in a periodic LWA.

In the previous graphic, for small values of a compared to the wavelength and $k > k_o$, k_{xn} will be imaginary and the mode will be *slow wave*. For large values of a and $k < k_o$, k_{xn} will be real, generating a leaky-wave mode or fast wave, showing that the energy is radiated to free-space. The edges of the triangles are the regions allowed for the existence of surface waves. When $k_o a$ increases, the wave changes from the surface wave into a leaky-wave back to

a surface wave, forming stop bands. Therefore, a radiation cone is created to allow radiation. The fundamental mode occurs in the dot blue line ($n = 0$) being a slow wave.

The n th harmonic radiates at an angle

$$\theta_n = \sin^{-1}\left(\frac{ka + 2\pi n}{k_o a}\right). \quad (3-16)$$

3.5

Applications in LWAs

Due to LWAs have demonstrated powerful abilities to achieve versatile functionalities on antennas, each passing day, multiple ideas are proposed, where only a few examples are mentioned below with the purpose to see different strategies that can be explored.

In 2007, D. Sievenpiper [4] and his team demonstrated the operation of an antenna with sinusoidal modulation in 2-D, using the holographic principle, where a monopole feeding generates the surface wave. Scalar and tensor impedance were modeled to produce a linear and circular polarization, respectively.

Another study of periodic LWA was made by A. Patel [43], in 2011, with a scalar impedance for a sinusoidal modulation in 1-D, using a microstrip line feeding. A variation of the parameter β and α was made with changes in the values of X_s , M and a , reporting the control of the scan angle and side lobe levels. In 2011, a spiral modulation of surface impedance was developed [31] to obtain a gain of 20 to 25 dB, with circular polarization using a vertical probe to excite the surface wave. In 2012, an LWA in SIW technology was reported [45], illustrated in figure 3.10. In this design, the leakage energy is the result of a periodic transverse slot.

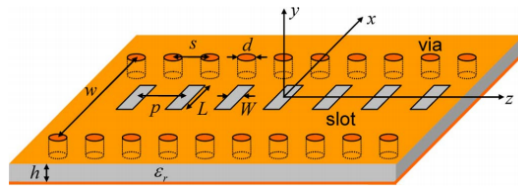


Figure 3.10: Slotted SIW leaky-wave antenna [45].

Another approach was developed in [6] using a right/left-handed meta-material based on equivalent circuit models to fabricate a 180° scanning beam antenna, from backfire to endfire, including broadside direction operating in the fundamental frequency. The structure of the antenna is illustrated in figure 3.11.

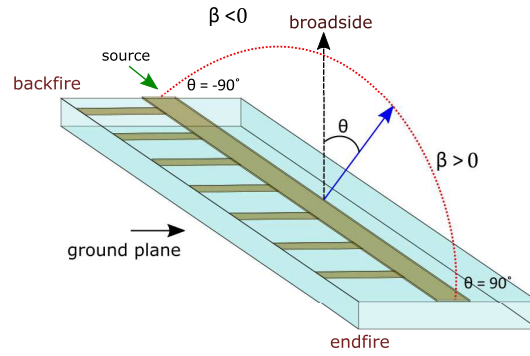


Figure 3.11: LWA based on a right/left-handed metamaterial.

3.6 Terahertz LWA

Advances in the field of metamaterials and metasurfaces have attracted attention in several applications, and recently in the terahertz spectrum (0.1 - 10 THz), with a focus on the wireless communication system for high data transmission and wide bandwidth, as well as the interaction of materials at high frequencies for sensor applications or imaging approach [46].

LWAs have been explored in terahertz frequencies with promissory response to create antennas with high gain and good performance in a very low profile, focused in beam steering, directive beam pattern and polarization control [46]. Some antennas are configured with tunable metamaterial using graphene and liquid crystal, and other are based in metasurfaces modulated [47].

Recent studies using the holographic principle in terahertz range have been explored in [48], [49] and [50], where the radiation behavior is the same as that obtained in microwave frequencies due to its easy scalability. However, some challenges have been approached in the manufacture and testing of devices that operate at terahertz frequency. Some contributions, such as characterization of materials for the manufacture of devices in these frequencies were made in [51], presenting information of dielectric constant, loss tangent and frequency range in common substrates.

4

Holographic Artificial Impedance Antenna

This chapter describes the theory of the holographic principle, from its first use in optical systems to its evolution in the field of microwave devices such as antennas. Furthermore, the properties that control the radiation characteristics in this type of antennas, and other performance parameters for the evaluation of the results are explained.

4.1

Background of Holography in Microwave System

In 1968, P. Checcaci applied for the first time the optical holography in microwave systems [52] used to produce a desired radiation pattern in a new kind of structure called holographic antenna. The invention was not successful due to its low efficiency and the need for an external feeding. However, since then, ways of using the holography in the domain of microwave devices have been discovered.

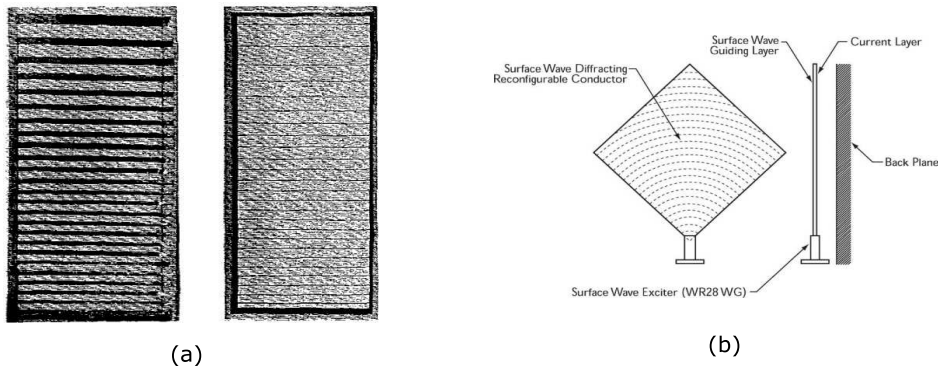


Figure 4.1: Examples of holographic antennas with (a) linear metallic film [52], and (b) curve metallic film [53].

As was previously mentioned, it was until 2007, when D. Sievenpiper [4] made a relevant study that combined the impedance modulation performed by A. A. Oliner and the holographic principle to control the angle of the maximum beam direction of the antenna. Thus, holographic antennas can be considered as 2-D leaky-wave structures. That work opened an essential study field for the development of holographic antennas with an integrated feeding implemented in dielectric substrates.

4.2

Principles of Holography

Dénes Gábor invented the holography in 1948 [6] as a method to improve the resolution in the electron microscope. In his experiments, a beam of light was used to capture the photograph of an object in an interference pattern or plane that would allow reconstructing the image in three-dimensions (3-D). Upon his discovery, he won the Nobel Prize for Physics in 1971. An example of the image formed by the holographic technique is illustrated in figure 4.2.

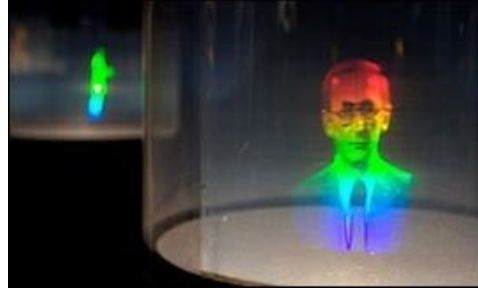


Figure 4.2: Example of a hologram image [54].

In optical systems, the holographic process consists of two steps [55]: recording and reconstruction of the object. In the recording step, a light source (reference wave) is directed to the interference plane, as is shown in figure 4.3, and at the same time, the object is illuminated by the same source to produce the hologram [56].

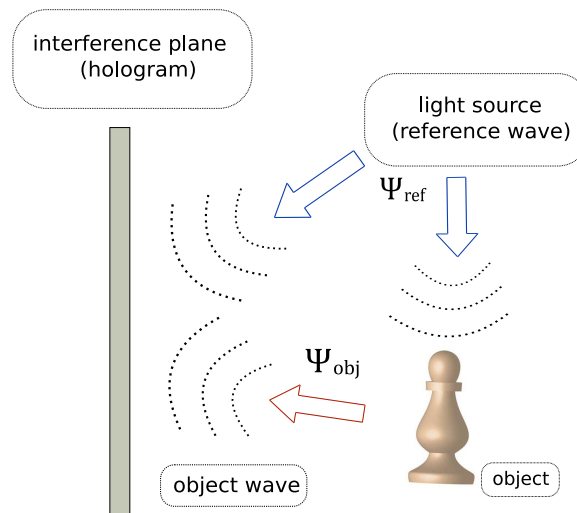


Figure 4.3: Recording process of the hologram.

The object reflects waves with phase variation (height information) according to the position of the reflected point on the surface of the object. The reference wave gives information of intensity similar to the photography (brightness contrast). Therefore, the hologram will be formed by different phase

values of the waves object and intensity of the light source, which will contain a proportional term to the object wave (Ψ_{obj}) and other proportional to the conjugate complex of the reference wave (Ψ_{ref}^*) [4] given by

$$\Psi_{obj}\Psi_{ref}^*. \quad (4-1)$$

In the reconstruction step, the plane is illuminated with the same light source, as illustrated in figure 4.4, forming a superposition between the reference wave and the proportional term recorded in the hologram that allows recovering a copy of the object in 3-D as expressed below

$$(\Psi_{obj}\Psi_{ref}^*)\Psi_{ref} = \Psi_{obj}|\Psi_{ref}|^2. \quad (4-2)$$

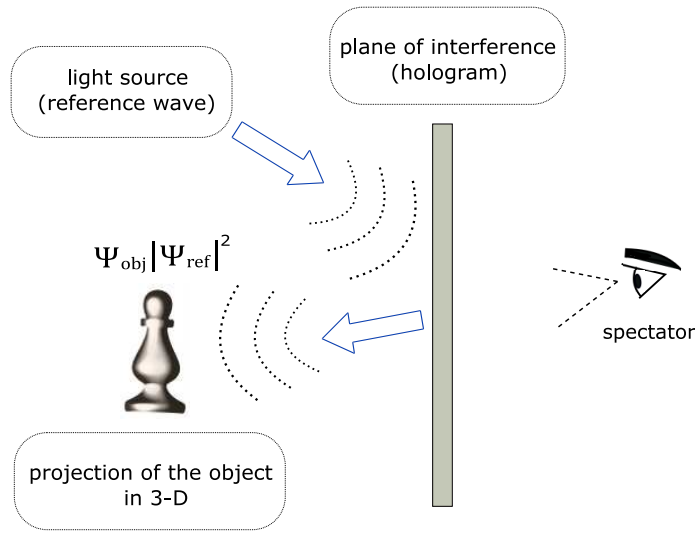


Figure 4.4: Reconstruction process of the hologram.

In antenna systems, the holographic technique is applied as described above. A feeding source generates a surface wave (Ψ_{surf}) considered as the reference wave, and the desired radiation pattern is the wave of the object (Ψ_{obj}) [4]. Both information are recorded in the hologram, as illustrated in the figure 4.5, and given by

$$\Psi_{rad}\Psi_{surf}^*. \quad (4-3)$$

Finally, when the surface wave is excited on the surface of the hologram, the desired field will be radiated, as defined below

$$(\Psi_{rad}\Psi_{surf}^*)\Psi_{surf} = \Psi_{rad}|\Psi_{surf}|^2. \quad (4-4)$$

The surface wave can be expressed as a cylindrical wave [4]:

$$\Psi_{surf} = e^{-jknr}. \quad (4-5)$$

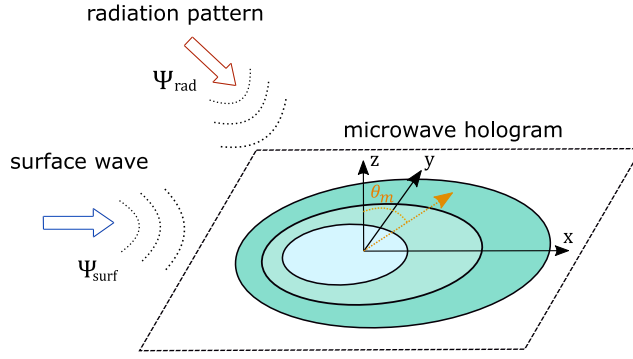


Figure 4.5: Illustration of the holographic principle in microwave system.

where n is the effective index seen by the surface current, and r is the distance from the feeding position. The desired field is defined to radiate at a specific angle (θ_m) from the normal to the surface, represented in equation (4-6):

$$\Psi_{rad} = e^{-jk_x \sin(\theta_m)}. \quad (4-6)$$

With the modulation of the surface impedance explained above and the holographic technique, it is possible to complete the design of the antenna, where the surface impedance will be distributed in 2-D, according to equation (3-12) and (4-3), given by

$$Z_s(x_t) = j[X_s + MRe(\Psi_{rad}\Psi_{surf}^*)], \quad (4-7)$$

where X_s is the average value of the impedance distribution, M is the modulation factor, and x_t is the point on the surface (plane xy). The leaky-wave mode propagating along of the holographic pattern determines the distribution of the aperture field of the antenna [33].

4.3

Parameters of Radiation Efficiency

The maximum radiation angle, beamwidth, and the side lobe levels characterize the performance of the HAIA [33], which can be tailored controlling the phase constant and the attenuation constant, both dependents on the geometry of the antenna and the frequency [39], [43].

The maximum radiation angle belongs to the main lobe, which is approximated by the following relationship

$$\theta_m \cong \sin^{-1}\left(\frac{\beta}{k_o}\right), \quad (4-8)$$

where θ_m is the angle formed with the normal to the surface of the antenna, as described above, and β is the phase constant of the leaky-wave mode traveling along of the holographic pattern, being dependent on the frequency. For illustration purpose, the maximum radiation angle is showed in figure 4.6.

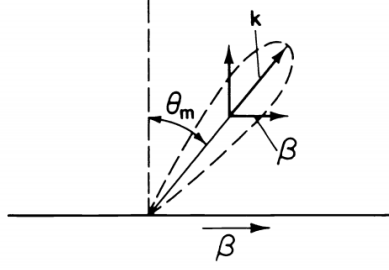


Figure 4.6: Representation of the maximum radiation angle of the antenna [33].

In [43], it was reported that by varying the modulation parameter X_s and the periodicity a in the holographic pattern it is possible to adjust the behavior of the phase constant without affecting the attenuation constant. The value of β must be kept constant along the surface length to have the radiation of all parts of the antenna points in the same direction [12].

Since the theory is established for a uniform LWA, it is possible to study the behavior of the rate of leakage per unit length along the surface, where the attenuation constant controls the beamwidth of the main beam radiation. Thus, to obtain a narrow beam, if the attenuation constant is large, a small surface length (L_s) will be required to radiate the energy rapidly. If the attenuation constant is small, the surface length may be longer for the leakage energy to be more efficient [33].

A recommendation to define the value of L_s is explained in [39] to radiate the power around 90% before the surface wave reaches the end of the whole surface, which means that at the end of the surface, the power level will be 10 dB lower than its initial level.

The value of α in dB per wavelength is given by

$$2\pi(8.686)\left(\frac{\alpha}{k_o}\right) = 54.60\left(\frac{\alpha}{k_o}\right). \quad (4-9)$$

An approximation of the length L_s is found by [39]

$$\frac{L_s}{\lambda_o} \approx \frac{10}{54.10}\left(\frac{1}{\alpha/k_o}\right) \approx \frac{0.18}{\alpha/k_o}, \quad (4-10)$$

$$L_s \approx \frac{0.18(\lambda_o)}{\alpha/k_o}. \quad (4-11)$$

In this kind of antenna, the beamwidth (Δ_θ) in the half-power measurements (3 dB) depends on the surface length, where it can be approximated from equation (4-11), as represented by [39]

$$\Delta_\theta \approx \frac{1}{L_s \cos(\theta_m)}. \quad (4-12)$$

In addition, in [43] it was studied that the parameter α allows the control of the side lobe level with its distribution along the antenna by varying the

value of the modulation factor M . A very low attenuation rate and large effective antenna aperture produce a high directivity.

4.4

Fundamental Performance Parameters

From the theory of antennas, different parameters and figure of merits are evaluated to describe the performance of the HAIA, which are presented in detail in the following sections.

4.4.1

Return Loss and Reflection Coefficient

Return Loss is the relation of energy fed from the input terminal (P_i) and the power reflected (P_r) by the antenna as result of an impedance mismatch, represented in dB, where is positive when $P_i > P_r$, which occurs in passive devices [57], given by

$$RL(dB) = 10\log_{10}\frac{P_i}{P_r}. \quad (4-13)$$

Also, the return loss is associated with the reflection coefficient (Γ), determined by the impedance at the input terminal (Z_{in}) and the characteristic impedance (Z_o), which are related by

$$\Gamma = \frac{Z_{in} - Z_o}{Z_{in} + Z_o}. \quad (4-14)$$

The reflection coefficient can be expressed in terms of the incident and reflected field in dB, presenting a negative value, and expressed by

$$\Gamma(dB) = 20\log_{10}\left(\frac{E_r}{E_i}\right), \quad (4-15)$$

where it can be presented by

$$\Gamma = 10\log_{10}\left(\frac{E_r}{E_i}\right)^2 = 10\log_{10}\left(\frac{P_r}{P_i}\right). \quad (4-16)$$

From equation (4-16) is seen than return loss is the negative magnitude of the reflection coefficient [57], expressed in dB, given by

$$RL(dB) = -20\log_{10}|\Gamma|. \quad (4-17)$$

In this dissertation, the term of reflection coefficient is used to measure the performance level of the antenna. The goal operation of this parameter in the antenna is lower than -10 dB, which means the antenna has an impedance mismatch that reflects lower than 10% of the input power into the transmission line [58].

4.4.2 Scattering Parameter

Scattering parameter (S-parameter) represents the relationship between the incident and reflected wave in the ports of a n-port Network. A schematic representation of a two-port is shown in figure 4.7.

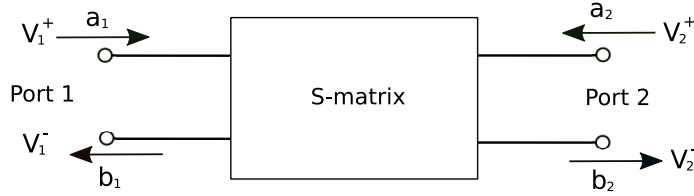


Figure 4.7: S-matrix.

The variables a_1 , a_2 and b_1 , b_2 are the incident and reflected wave, respectively. Thus, the scattering matrix denominated S-matrix relates each port by

$$\begin{aligned} S_{11} &= \frac{b_1}{a_1} \Big|_{a_2=0}, \\ S_{21} &= \frac{b_2}{a_1} \Big|_{a_2=0}, \\ S_{12} &= \frac{b_1}{a_2} \Big|_{a_1=0}, \\ S_{22} &= \frac{b_2}{a_2} \Big|_{a_1=0}. \end{aligned} \quad (4-18)$$

For the condition $a_2 = 0$ which means a perfect match of impedance, there is no reflected wave in port 2. In the condition $a_1 = 0$ there is no incident wave in port 1. The parameters S_{11} and S_{22} are known as reflection coefficients, and S_{12} and S_{21} are the transmission coefficients.

4.4.3 Voltage Standing Wave Ratio

Voltage Standing Wave Ratio (VSWR) is a measure to know how much power is reflected due to the impedance matching between the load, for example an antenna, and the characteristic impedance of the transmission line. The variation of voltage across the transmission line is measured. A low value of VSWR indicates that most of the incident power is delivered to the antenna, and reflections are almost avoided. A typical value for the performance of the antennas is VSWR lower than 2.

4.4.4 Efficiency

The efficiency of the antenna is the product of different losses at the input terminal of the antenna [59], defined by

$$e_o = e_r e_c e_d, \quad (4-19)$$

where e_r is the reflection efficiency ($1 - |\Gamma|^2$), e_c is the conduction efficiency and e_d is the dielectric efficiency. Using equation (4-20), the antenna radiation efficiency is expressed by

$$e_{cd} = e_c e_d. \quad (4-20)$$

4.4.5

Aperture efficiency

Aperture efficiency relates the maximum gain of the antenna and its physical size. Also, it is a parameter to know the efficiency of the antenna at receiving the radiated waves. In an HAIA, the aperture efficiency is low, commonly from 0 to 20% due to the leaky-wave behavior [31]. The relationship is given by

$$\epsilon_a = \frac{\lambda^2}{4\pi A_p} G_o, \quad (4-21)$$

where G_o is the maximum gain of the antenna and A_p is the physical aperture. In an HAIA, when the physical area is reduced, it is produced a reduction of gain. Some variation in the distribution of the impedance surface can be performed in order to avoid the effect and to enhance this parameter [2].

4.4.6

Directivity

Directivity is the ratio between the radiated power (U) in a given direction and the intensity of radiation (P_{rad}) averaged in all directions [59], expressed by

$$D = \frac{4\pi U}{P_{rad}}. \quad (4-22)$$

In that sense, directivity only describes the directional properties of the radiation pattern [59].

4.4.7

Gain

The gain of the antenna is related to the directivity. It is defined how well the input power (P_{in}) is converted into a radiated wave in a specific direction [59]. The gain is expressed as the ratio between the intensity in the maximum radiation and the intensity of radiation if the input power by the antenna were radiated isotropically, measured in a logarithmic scale. The unit

of measurement adopted in this dissertation is dB [59]. The components in the plane θ and ϕ are defined by

$$G_\theta = \frac{4\pi U_\theta}{P_{in}}, \quad (4-23)$$

$$G_\phi = \frac{4\pi U_\phi}{P_{in}}, \quad (4-24)$$

where U_θ and U_ϕ are the intensities of the radiation in the components E_θ and E_ϕ , respectively. The gain takes into account the radiation efficiency (e_{cd}) and its directivity property [59], related by

$$P_{rad} = e_{cd}P_{in}, \quad (4-25)$$

where the components in the direction θ and ϕ are given by

$$G_\theta = e_{cd} \left(\frac{4\pi U_\theta}{P_{rad}} \right), \quad (4-26)$$

$$G_\phi = e_{cd} \left(\frac{4\pi U_\phi}{P_{rad}} \right). \quad (4-27)$$

4.4.8 Beamwidth

Beamwidth is the aperture angle of the main lobe in the radiation pattern, where the maximum power is radiated [59]. The beamwidth is defined by the half-power beamwidth (HPBW) parameter and the first null beamwidth (FNBW) as illustrated in figure 4.8. HPBW is the angular separation where the power decreases by 50 % from the main beam (-3 dB) and FNBW is the angular separation between the first nulls adjacent to the main lobe.

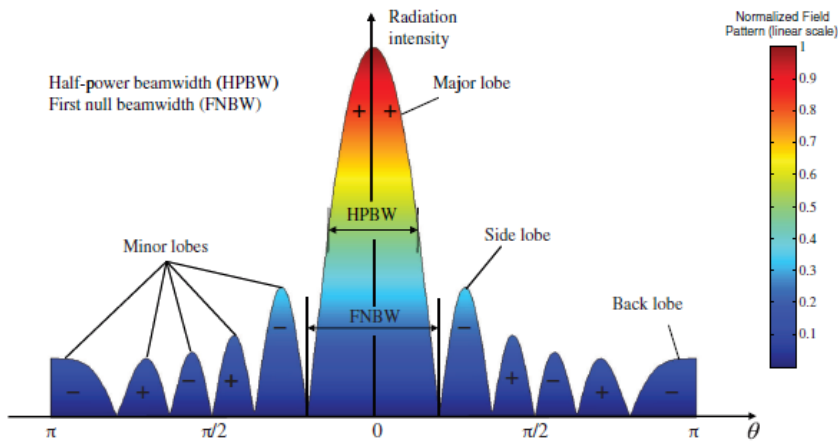


Figure 4.8: 2-D Radiation pattern [59].

4.4.9 Radiation Pattern

The radiation pattern is a spacial representation in the two-dimensional or three-dimensional plane of the fields radiated by the antenna [59]. The distribution of the space used as a reference is the spherical coordinate system, where the angle θ starts on the z -axis, and the ϕ angle on the x -axis, as illustrates in figure 4.9. The main patterns commonly used to measure the direction of the maximum radiation are the E-plane and the H-plane. The spatial distribution of the HFSS software used in this dissertation corresponds to the same reference described above.

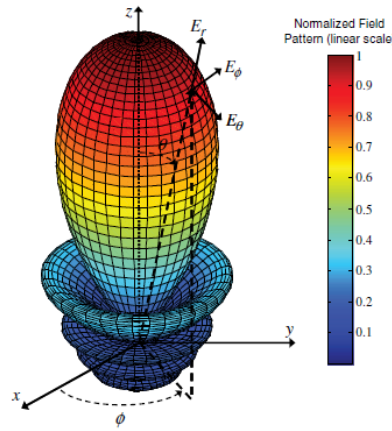


Figure 4.9: 3-D Radiation pattern [59].

4.4.10 Bandwidth

Bandwidth is the frequency range in which the performance of the antenna has acceptable values to transmit or receive energy according to its application, where the operating characteristics of the antenna are practically constant in the whole frequency range [59]. A criterion to define the bandwidth adopted in this dissertation is the band limited by the point where the reflection coefficient is equal to -10 dB. Bandwidth can also be expressed in terms of percentage concerning the central frequency, given by

$$BW(\%) = 100\left(\frac{F_H - F_L}{F_C}\right), \quad (4-28)$$

where F_C is the central frequency and F_H and F_L are the highest and lowest frequencies in the band, respectively. Also, it can be expressed in absolute values, defined by

$$BW = F_H - F_L. \quad (4-29)$$

4.4.11

Front-to-back ratio

Front-to-back ratio (FTBR) is an important parameter to measure the ratio between the maximum power radiated by the antenna (P_1) and the power radiated in the opposite direction (P_2), expressed in dB as presented in equation (4-30). A higher ratio means that more energy is radiated in the frontal direction.

$$FTBR = 10\log_{10}\left(\frac{P_1}{P_2}\right). \quad (4-30)$$

4.4.12

Polarization

The polarization of a radiated electromagnetic wave is determined by the time-varying direction and magnitude of the electric field [59]. The most common polarizations in antennas are linear and circular. The polarization is linear when the electric field vector is always oriented in a straight line in the same direction of a single plane. This orientation can be vertical, where the electric field is perpendicular to the direction of propagation, or horizontal, where the electric field is parallel to the direction of propagation.

In circular polarization the electric field has two components perpendicular to each other with the same amplitude and a phase difference of 90° between them, resulting in a circle rotation when the wave propagates. According to the direction of rotation, the wave is left- or right-handed circular polarized. For conventional HAIAs, the polarization of the feeding determines the polarization of the antenna [2]. In Chapter 6, the polarization evaluation of the surface wave source is presented.

4.5

Co-polarization and Cross-polarization

The co-polarization represents the reference polarization of the radiated electric field. Therefore, cross-polarization is the orthogonal component to a reference polarization [59]. In this dissertation is used the third definition of A. Ludwig presented in [60] to solve the cross-polarization of the HAIA.

Works found in the literature about HAIAs report cross-polarized components with significantly small values [2], [43]. In [2], an analysis is performed for the cross-polarized component of the electric field in the E-plane.

4.6

Axial Ratio

The axial ratio measures how circularly polarized is an antenna, commonly used to define its polarization [59]. This parameter is expressed as the ratio between the minor and major axis of the polarization ellipse, as illustrated in figure 4.10, due to, the electric field vector traces an elliptical trajectory, in general. For an axial ratio of 0 dB, the antenna is circularly polarized ideally. In practical terms, an axial ratio below than 3 dB means a circularly polarized antenna. Infinite values represent a perfect linear polarization due to the orthogonal component of the electric field is zero. Therefore, for large values of this parameter, the antenna polarization can be considered as linear.

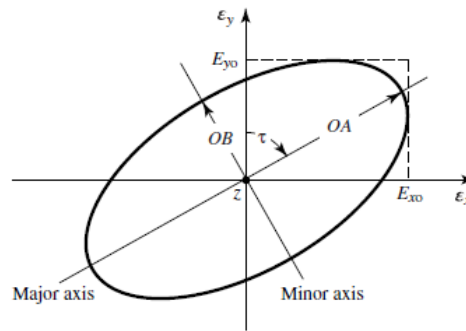


Figure 4.10: Polarization ellipse [59].

4.7

Field Regions of the Antenna

The regions surrounding an antenna are classified into the reactive near-field, radiating near-field and far-field, which depend on the distance between the antenna and the point of measurement. Table 4.1 summarizes the distance condition of the antenna radiation, where D is the maximum dimension of the antenna, r is the measurement point and λ is the wavelength in the free-space.

Table 4.1: Field regions of an antenna [59].

Reactive near-field	Radiating near-field	Far-field
$r < 0.62\sqrt{\frac{D^3}{\lambda}}$	$r \geq 0.62\sqrt{\frac{D^3}{\lambda}}$	$r > \frac{2D^2}{\lambda}$

In the reactive near-field, the field is purely reactive. In the radiating near-field, the field is less reactive and a percentage of the energy is radiated. In the far-field, the radiating fields are dominants and the radiation pattern does not change with the distance [59].

5

Planar Surface Wave Feeding

This chapter outlines the feeding characteristic of the proposed planar source of the HAIA to generate a surface wave on the surface. Its advantages are explained according to other conventional feedings. The fundamental theory is reviewed, and equations for its design are presented.

5.1

Characteristics of Surface Wave Feeding

A surface wave in a holographic antenna can be excited with the electric field perpendicularly (TE mode) or parallelly (TM mode) polarized to the propagation direction. A planar launcher is able of producing this kind of surface wave, such as a microstrip transmission line [43], slotted quasi-Yagi-Uda [61], antipodal feed [62] and Vivaldi antenna [3] as illustrated in figure 5.1. Another planar launcher is the SIW H-plane sectoral, which is the interest in this dissertation due to its simple design widely studied in the literature [63], [64] and easy integration with the holographic surface.

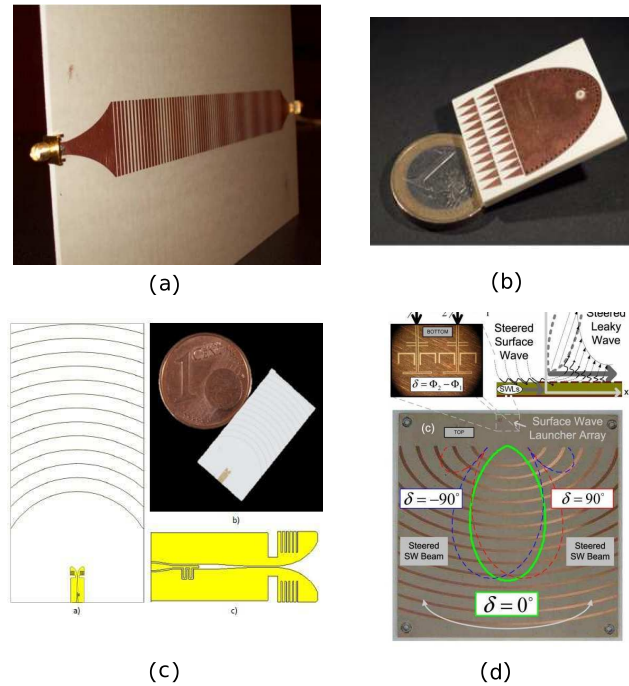


Figure 5.1: Types of planar feeding using: (a) microstrip line [7], (b) SIW H-sectoral antenna [8], (c) Vivaldi antenna [9], and (d) quasi-Yagi antenna [10].

In an HAIA, the surface wave needs a surface with a suitable dimension to be propagated according to type of the feeding. When that surface is reduced, the antenna gain at the desired beam angle is affected. To obtain a narrow beam with a gain higher than 20 dB using a conventional modulation impedance, in [4], a holographic surface of 40.64 cm x 25.4 cm was reported, and in [2], a surface of 23.87 cm x 19.81 cm was used to generate 16 dB of gain, both with a monopole feeding.

Therefore, a planar source is studied to provide higher directivity, which represents essential advantages, such as:

- A more directive surface wave excitation, where the antenna is fed with higher power level;
- To avoid the phenomenon of the main lobe splitting when the antenna operates in different design frequencies [65];
- To allow the reduction of the area on the holographic surface without affecting the antenna performance. An example of miniaturization of the holographic pattern using a planar source is found in [66].

In the following sections, the fundamental theory of conventional H-plane sectoral antenna and its development in the SIW technology will be explained in detail.

5.2 Conventional H-plane Sectoral Antenna

The conventional H-plane sectoral antenna belongs to a group of horn antenna [59], formed by an opening in the walls of the waveguide in the direction of the magnetic field, where the radiation is focused on the H-plane, keeping the vertical dimension constant as shown in figure 5.2. This antenna is characterized by wide gain and bandwidth, and the theory of waveguide aperture is used for its design [6].

To ensure the existence of a single propagation mode inside the waveguide, the width a must satisfy the following relationship

$$\frac{\lambda_o}{2\sqrt{\epsilon_r}} < a < \frac{\lambda_o}{\sqrt{\epsilon_r}}. \quad (5-1)$$

The cutoff frequency of propagating modes inside the waveguide is defined by

$$f_{mn} = \frac{1}{2\pi\sqrt{\mu\epsilon}} \sqrt{\left(\frac{m\pi}{a}\right)^2 + \left(\frac{n\pi}{b}\right)^2}, \quad (5-2)$$

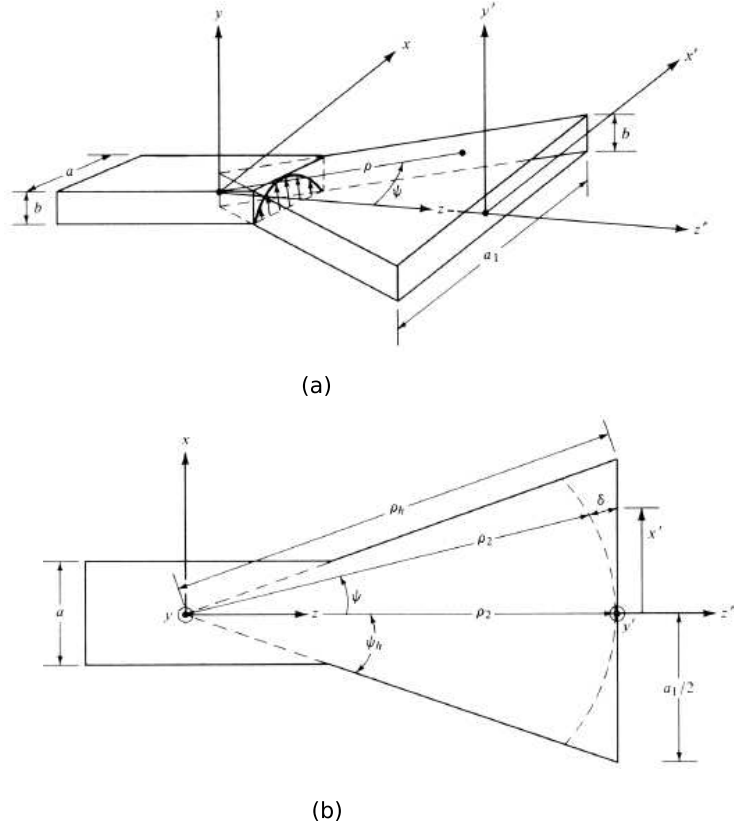


Figure 5.2: Structure of a conventional H-plane sectoral antenna: (a) frontal view, and (b) top view [59].

where a and b are the width and height dimensions of the waveguide, μ and ϵ are the permeability and permittivity of the substrate, respectively. Inside of the guide, m and n are related to the modes of propagation.

Thus, for the fundamental mode (f_{10}), the equation (5-2) is reduced to [67]

$$f_{10} = \frac{c_0}{2\sqrt{\epsilon_r}a}. \quad (5-3)$$

The aperture dimension a_1 , which determines the maximum directivity of the antenna, is expressed by

$$a_1 \cong \sqrt{3\lambda\rho_2}, \quad (5-4)$$

and the following relationships in the geometry are used for construction of the waveguide aperture

$$\rho_h^2 = \rho_2^2 + \left(\frac{a_1}{2}\right)^2, \quad (5-5)$$

$$\psi = \tan^{-1}\left(\frac{a_1}{2\rho_2}\right), \quad (5-6)$$

$$L_h = (a_1 - a)\sqrt{\left(\frac{\rho}{a_1}\right)^2 - \frac{1}{4}}. \quad (5-7)$$

The radiation pattern that characterizes a conventional H-sectoral antenna is shown in figure 5.3 for its corresponding E- and H-plane. In the H-plane, the antenna radiates with a narrow pattern [59].

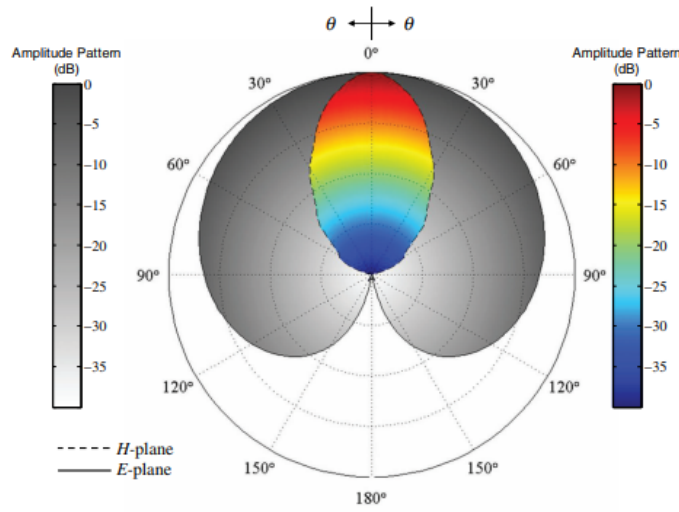


Figure 5.3: Radiation pattern of the E- and H-plane of a conventional H-plane sectoral antenna [59].

With the purpose to supply the microwave energy to the conventional H-sectoral antennas, a small coaxial probe is inserted, acting as a quarter-wave antenna, where the highest efficiency point is located at a distance of $\lambda/4$ from the bottom wall of the waveguide. In this position, the electric field has a maximum coupling in its fundamental mode.

5.3 SIW H-plane Sectoral Feeding

The evolution of the SIW technology since its invention [68], in 2001, allowed the development of the H-plane sectoral antenna based on that approach. The structure is composed of a rectangular waveguide formed by vias embedded in a two-layer dielectric substrate that act as side walls to generate the propagation of a guide mode. The waveguide is opening in the direction of the magnetic field as illustrated in figure 5.4, applying the same rules of the geometric construction as the conventional H-plane horn antennas [63]. The modes allowed inside the waveguide are the TE_{n0} , ($n = 1, 2, \dots$), where the fundamental mode is TE_{10} . Due to the gap between the metalized vias, the transverse magnetic mode (TM) is not supported [69].

The equations to parameterize the dimensions of the structure are presented below [69]: an effective length of w_{eff} is calculated to relate the characteristics of the conventional waveguide with the SIW defined in equation (5-8).

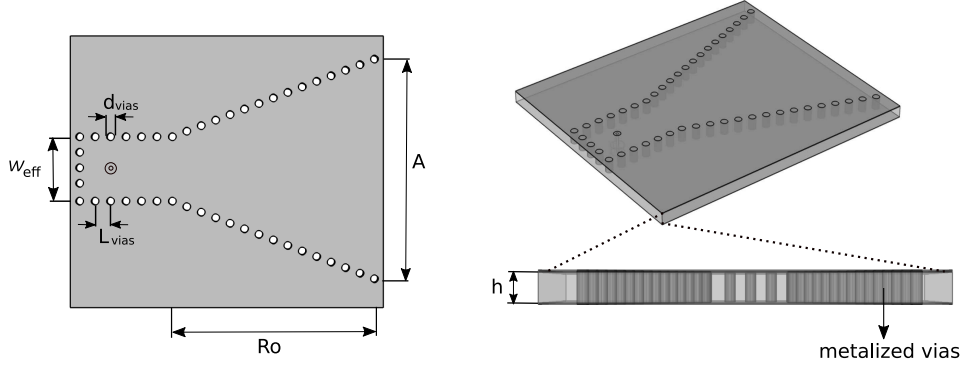


Figure 5.4: Geometry of a SIW H-plane sectoral feeding.

$$w_{eff} = a - \frac{d_{via}^2}{0.95L_{via}}. \quad (5-8)$$

Another approximation to solve w_{eff} is given by

$$w_{eff} = a - 1.08 \frac{d_{via}^2}{L_{via}} + 0.1 \frac{d_{via}^2}{a}, \quad (5-9)$$

where a is the distance between the walls of the waveguide, d_{via} is the diameter of the metalized vias, and L_{via} is the center-to-center distance between the vias. To avoid the leakage energy between the vias, values of $d_{vias}/L_{vias} < 2.5$ are recommended.

As in conventional waveguide, the width a for the fundamental mode is given by

$$a = \frac{c_o}{2\sqrt{\epsilon_r}f_{10}}. \quad (5-10)$$

The parameters A and R_o determine the gain and the aperture pattern in the same way as those defined for the conventional H-sectoral antenna [59]. The curves that relate the parameters R_o and A to estimate the gain are illustrated in figure 5.5 [67].

5.4 Printed Transition Zone

An H-plane antenna in SIW technology that operates in millimeter waves presents poor radiation when the thickness of the substrate is smaller than the wavelength. At frequencies below 20 GHz in substrates thinner than $\lambda/6$, a mismatch in the output of the structure is noted, which produces unwanted back radiation. A practical solution was presented in [63] and [64] to overcome the above limitations, using a printed transition zone after the aperture of the antenna, keeping the compact design and easy implementation. With that solution, parameters such as FTBR, gain and reflection coefficient are improved.

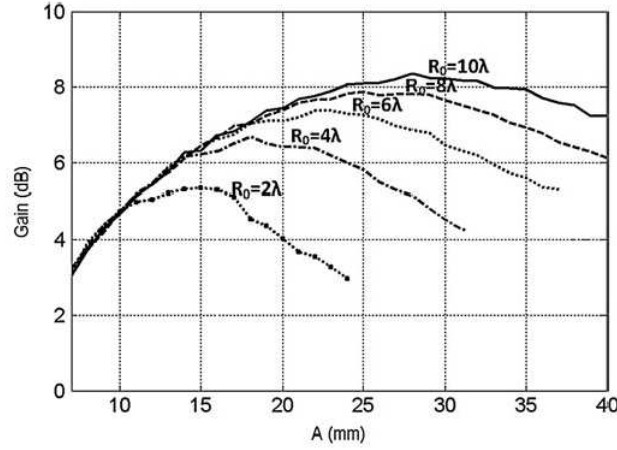


Figure 5.5: Values of gain for different lengths and waveguides aperture for the SIW-H sectoral feeding [67].

A basic transition zone consists of two blocks, seen as radiating elements presented in figure 5.6. Parallel blocks can be printed at the top and bottom of the copper thickness substrate. The field at the edge of the elements A , B and C (dot red line) contributes to the radiation pattern with amplitudes A_o , A_1 and A_2 , respectively.

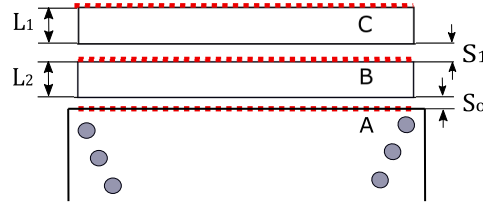


Figure 5.6: Transition zone with parallel blocks.

The gaps between the blocks S_o and S_1 affect the amplitude fields A_i and A_{i+1} . Also, there is a phase difference among the elements A , B and C controlled by the length L_1 and L_2 , where $L_i \gg S_i$. The phase difference in each element ($\alpha_{i,i+1}$) is given by

$$\alpha_{i,i+1} = \beta_{pp} L_{i+1}, \quad (5-11)$$

where β_{pp} is the propagation constant in the parallel blocks, expressed by

$$\beta_{pp} = \frac{2\pi\sqrt{\epsilon_{rpp}}}{\lambda_o}. \quad (5-12)$$

The effective dielectric constant (ϵ_{rpp}) is solved with an approximation presented in [70], defined by

$$\epsilon_{rpp} = \frac{\epsilon_r + 1}{2} + \frac{\epsilon_r - 1}{2} \left(1 + \frac{10h}{w}\right)^{-1/2}. \quad (5-13)$$

The total radiation field is expressed by

$$f(\phi) \approx A_o g(\phi) + A_1 e^{-j\alpha_1} g(\phi) e^{j(\frac{2\pi}{\lambda_o})L_1 \sin(\phi)} + A_2 e^{-j(\alpha_1+\alpha_2)} g(\phi) e^{j(\frac{2\pi}{\lambda_o})(L_1+L_2) \sin(\phi)}, \quad (5-14)$$

where $g(\phi)$ is the radiation pattern of each element.

The equation (5-14) can be simplified if $L_1 = L_2 = L$, and thus, $\alpha_{01} = \alpha_{12} = \alpha$, which results in

$$f(\phi) \approx (A_1 + A_2 e^{j\alpha} e^{-j(\frac{2\pi L}{\lambda_o}) \sin(\phi)}) g(\phi). \quad (5-15)$$

With a value of S_1 capable of making the field amplitude $A_1 \approx A_2$, there is a relationship that minimizes the backward radiation in $f(-\pi/2)$ given by

$$\frac{2\pi L}{\lambda_o} + \beta_{pp} L = (2n + 1)\pi, n \in Z. \quad (5-16)$$

Therefore, from equation (5-16), the value of L that strongly optimizes the FTBR in the antenna is given by

$$L = \frac{c_o}{2f_{FTBR}(1 + \sqrt{\epsilon_{rpp}})}, \quad (5-17)$$

where f_{FTBR} is the frequency to reach a high value of FTBR. However, to obtain a match between a good FTBR and coefficient reflection (S_{11}), the following condition is necessary

$$f_{FTBR} \approx f_o, \quad (5-18)$$

where f_o is the operating frequency of the H-plane antenna. The value of ϵ_{rpp} can be decreased by using a grid of small patches, as shown in figure 5.7.

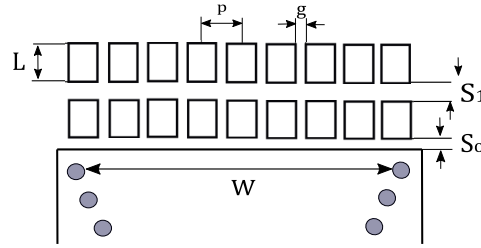


Figure 5.7: Transition zone with small rectangles.

In equation (5-17), it is noted that the effective permittivity has a greater effect in f_{FTBR} , and, therefore, by decreasing the value of ϵ_{rpp} , it is possible to comply with the condition (5-18). The appropriate value of p and g can be adjusted with simulation software until it fulfills the condition (5-16). The recommended values are $g < p/2$ and $p < W/10$, where W is the aperture length of the waveguide as illustrated in figure 5.7.

6

Design Procedure of the HAIA

This chapter presents a step-by-step procedure to implement the HAIA as a proof of concept in the K band, modeling the surface wave launcher and the holographic surface. A comparative study is performed among three types of feeding, and design goals are established to guide the analysis of results. The components of the antenna are designed using the full-wave electromagnetic simulator HFSS based on the finite element method (FEM).

6.1

Design Goals

The design goals established in this dissertation are based on the operating performance found in the literature for this kind of LWAs, listed in table 6.1. Different scenarios are modeled according to these requirements to choose the prototype with the best performance.

Table 6.1: Design requirements of the HAIA.

Parameter	Specification
Angle of the main beam (θ_m)	different angles tested.
Reflection coefficient (S_{11})	lower than -10 dB.
Gain of the maximum beam	greater than 20 dB.
HBPW	lower than 5°.
VSWR	lower than 2.
Cross-polarization	lower than -30 dB.

6.2

Modeling of the AIS

The design goal of the AIS unit cell is to provide high surface impedance values with changes in each size variation of the metal patch. A scalar impedance is modeled to support a TM surface wave mode along the surface. In this project, the method developed in [4] is used, where a unit cell is characterized by periodic boundary conditions to find the refractive index n in the surface.

The unit cell consists of a dielectric substrate with a copper thickness formed by a metallic patch on a ground plane. An example of this structure is illustrated in figure 6.1. The response of the AIS is evaluated in the shape of a circle, triangle, and square, presented in section 6.2.2. The lattice of the unit cell a is constant, and the metallic patch varies in the gap g using a parametric sweep on HFSS. The height of the air box is recommended to be $\lambda/2$ to avoid the propagation of other modes. The radiation boundary condition used is a master/slave applied on the lateral sides (xy plane), choosing the eigenmode solution on HFSS.

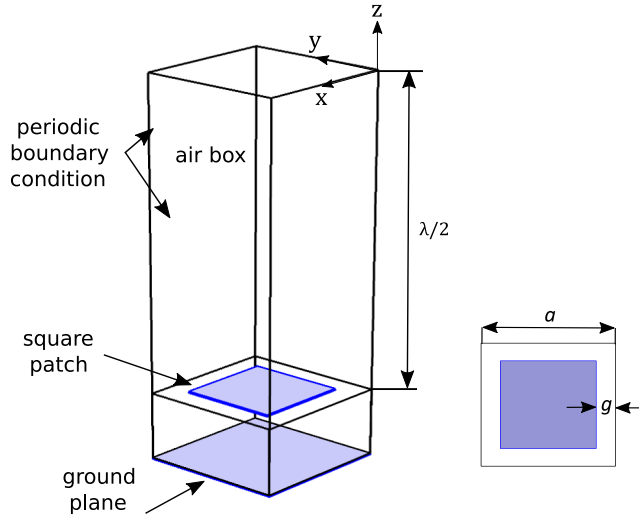


Figure 6.1: Setup used in the full-wave simulation of the unit cell on HFSS.

The eigenmode solution is used to find the resonance frequency that satisfies the boundary condition of the unit cell in each variation of g . The first resonance mode of the structure is chosen. Thus, the refractive index on the surface can be solved by

$$n = \frac{k_t}{k}, \quad (6-1)$$

where k_t is the propagation wavenumber on the surface and k is the propagation constant ($k = 2\pi/\lambda_w$) where λ_w is the wavelength of the eigenfrequency for a given value of g in the metallic patch.

In the boundary condition on HFSS, a phase difference (ϕ) is arbitrarily chosen to calculate k_t . According to equation (6-2), this phase difference implies in a radiated wave phase offset.

$$k_t = \frac{\phi}{a}. \quad (6-2)$$

Thus, the refractive index in equation (6-1) can be solved. The surface impedance for a TM surface wave mode is given in equation (6-3):

$$Z_s = jZ_o \frac{k_z}{k}, \quad (6-3)$$

where Z_o is the impedance of the free-space and k_z is the decay constant along z -direction, given by

$$k_z = \sqrt{k_t^2 - k^2}. \quad (6-4)$$

By substituting the equation (6-4) into (6-3), the final equation of impedance related to the refractive index is found, which is expressed by

$$Z_s = Z_o \sqrt{1 - n^2}. \quad (6-5)$$

6.2.1

Influence of the phase difference in the Unit Cell

The influence of the phase difference in the unit cell is studied in this subsection. In the simulations is used a dielectric substrate RT/duroid 5880 with electric permittivity $\epsilon_r = 2.2$, loss tangent $\tan\delta = 0.0009$, with thickness copper of $35 \mu\text{m}$ and height of 1.57 mm . The phase difference in the boundary condition varies in three values: 60° , 70° , and 72° . The gap in the unit cell is set from $g = 0.2 \text{ mm}$ to $g = 1 \text{ mm}$, taking into consideration the smallest gap allowed for fabrication facility. The eigenmode frequencies for each gap variation are presented in figure 6.2. With a higher value of ϕ , the resonance frequency increases, producing higher values of surface impedance. Thus, this parameter can be tailored according to the operating frequency of the antenna.

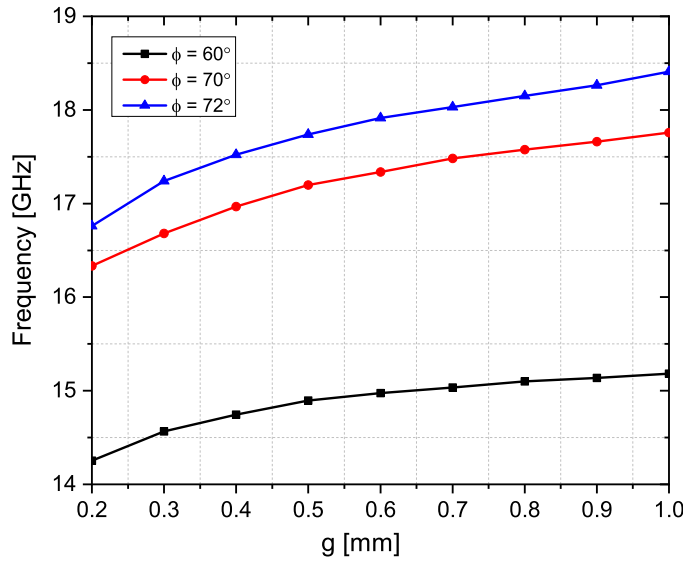


Figure 6.2: Resonance frequencies of the unit cell with variation of the phase difference.

6.2.2

Modeling of the Scalar Surface Impedance

A comparative analysis between different dielectric substrates is performed to model the surface impedance of a square patch. For study purposes, the loss tangent ($\tan\delta$) is fixed to an arbitrary value to evaluate the influence of the electric permittivity (ϵ_r) of the substrate. Table 6.2 shows the properties of the materials tested. The height in all the dielectric substrates is 1.57 mm with a copper thickness of 35 μm .

Table 6.2: Properties of the materials tested.

Material	ϵ_r	$\tan\delta$
RT/duroid 5880	2.2	0.0009
FR-4	4.6	0.0009
RT/duroid 6006	6.15	0.0009
RT/duroid 6010	10.2	0.0009

The surface impedance in the unit cell is solved using the equations (6-1), (6-2) and (6-5), and applying the setup of HFSS used in section 6.2.1, with a phase difference of 72° given the frequency range of interest in this work. The result among the dielectric substrates under analysis is shown in figure 6.3.

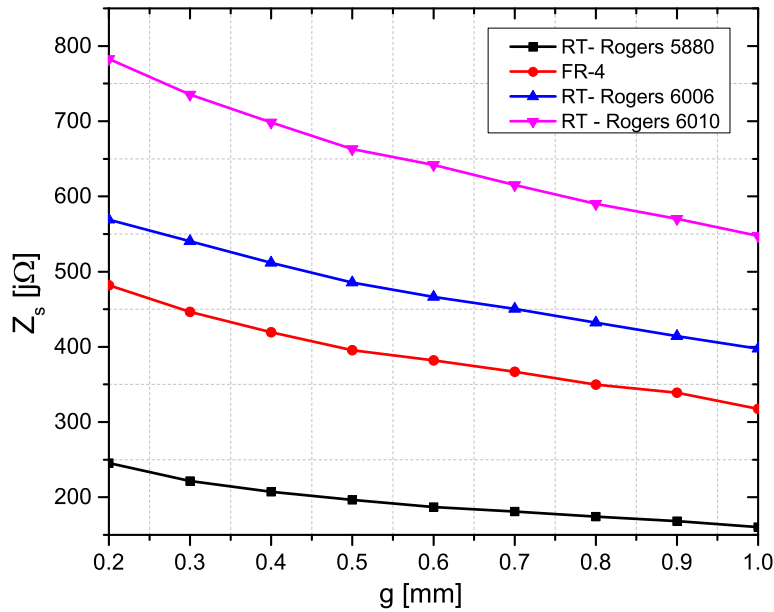


Figure 6.3: Surface impedance of the unit cell for the different material tested.

Also, in [4], it is reported that high impedance values are obtained with lower values of g , a thicker substrate, narrow gap, and larger period a . In the previous graph, it is noted that the higher electric permittivity generates a high impedance value. However, a higher concentration of the electric field can appear affecting the propagation of the surface wave along the antenna. The response of the resonance frequencies of the materials tested is shown in figure 6.4. The dielectric substrate with the lowest electric permittivity presents the highest resonance frequencies.

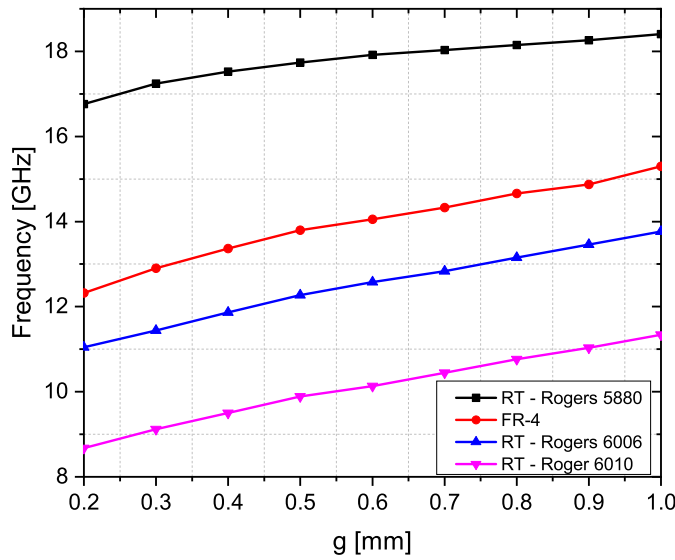


Figure 6.4: Resonance frequencies for the different materials tested.

It is essential to mention that any of the dielectric substrates investigated above can be used for the tailored design of the HAIA, according to the performance tolerances of the antenna and frequency range of interest. However, a dielectric substrate with low loss tangent and low electric permittivity is recommended to enhance the antenna efficiency. Thus, the final design goal of the unit cell is to model a periodic variation of the impedance to produce controlled leaky-wave radiation, as explained in Chapter 3.

In this dissertation, the dielectric substrate RT/duroid 5880 is chosen due to its good performance efficiency in antennas at high frequencies and low loss tangent, fulfilling with the operating goals of the project. The surface impedance is also solved for a circle and triangle patch and a comparative result with the square patch is shown in figure 6.5. The square patch presents the best response of high values of impedance with higher variation concerning the other geometries. Furthermore, due to its simple design, this structure is chosen in this work.

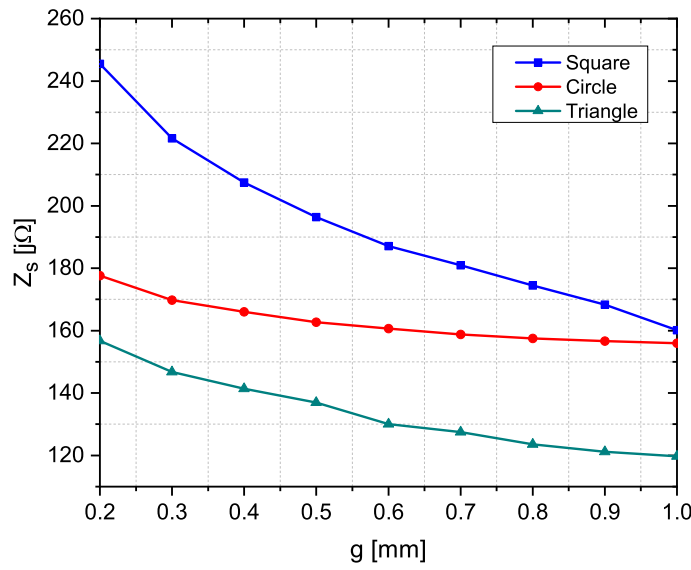


Figure 6.5: Relationship between gaps and surface impedance of the unit cell for different geometries tested.

The final curve of impedance of the square patch is presented in figure 6.6, where a polynomial approximation is calculated to obtain the relationship with the gap of the lattice square, given in equation (6-6).

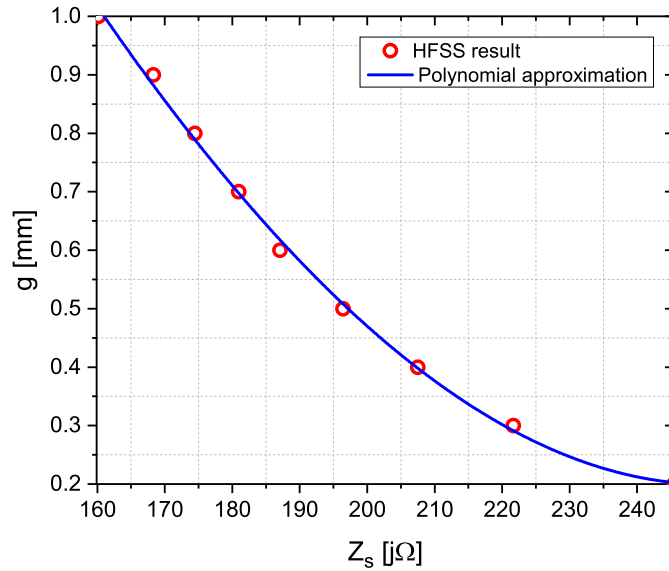


Figure 6.6: Relationship between gaps and surface impedance of the unit cell with square patch.

$$g = -2.833 \cdot 10^{-7} (Z_s^3) + 2.729 \cdot 10^{-4} (Z_s^2) - 0.085 (Z_s) + 8.839. \quad (6-6)$$

6.3

Modeling of the Holographic Pattern

The polynomial approximation in equation (6-6) and the holographic surface impedance in equation (4-7) allow performing the impedance distribution in the holographic pattern. The holographic model will have recorded the information of the desired field at a specific angle of radiation included in the term $\Psi_{rad} = e^{jk_x \sin(\theta_m)}$, where the phase constant along the surface will be related to the surface impedance. Therefore, the impedance distribution allows performing a phase distribution on the surface [2]. Figure 6.7 shows a flow diagram of the steps to make the spatial distribution of the impedance in a plane xy .

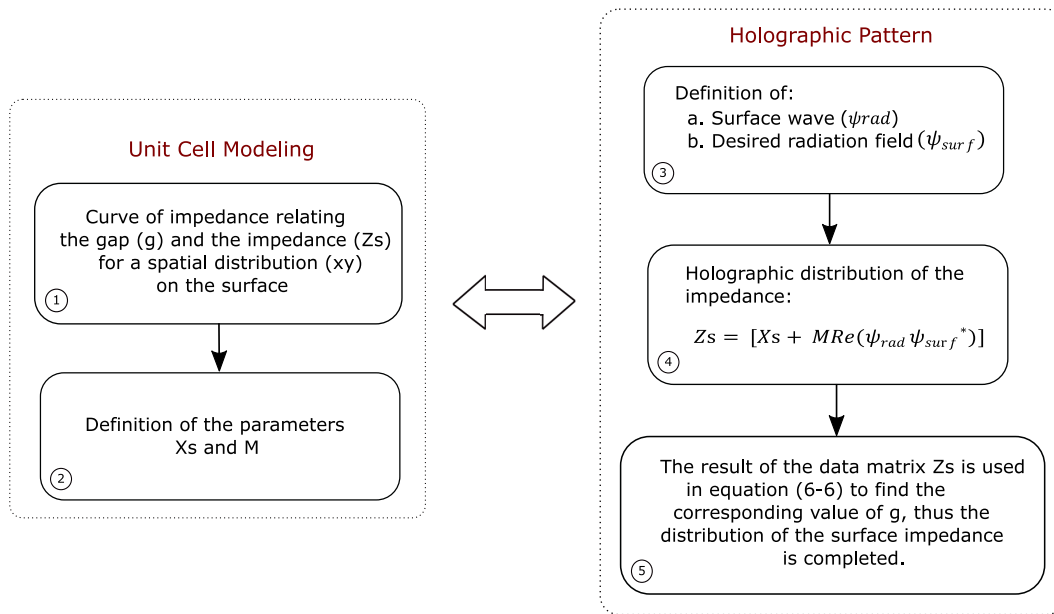


Figure 6.7: Flow diagram of the distribution of the surface impedance.

In the step (1) and (2), the curve of impedance is found, and the parameters X_s and M can be defined, where X_s is taken as the average value of the impedance range and M is the modulation factor that can be adjusted to obtain the desired aperture field [4]. According to figure 6.6 and following the same relationship in [4], the impedance range of the unit cell is between $245.47 \text{ j}\Omega$ and $162.06 \text{ j}\Omega$. Thus, X_s is $193.76 \text{ }\Omega$, and M is chosen to be $51.70 \text{ }\Omega$. Also, the design frequency of the antenna is defined in the hologram.

In the step (3) and (4), the surface wave and the desired radiation field are defined to make the holographic distribution on the surface, where the impedance will acquire values between X_s and M , which combined with equation (6-6) will generate a pattern of squares patches with different sizes and positions depending on the gap of the unit cell.

Thus, the holography fulfills the function of making a systematic and smart impedance distribution, because if the equations that represent the generated surface wave and the desired field are known, the impedance distribution required to convert a surface wave into a leaky-wave would be known in controlled radiation.

The algorithm of the impedance distribution is processed in MATLAB, and an example of the holographic pattern is illustrated in figure 6.8 formed by concentric ellipses. The resulting data are converted to a drawing exchange format (DXF) to be imported into HFSS. In this project, to test the theory of control of the maximum beam direction in the proposed designs, different angles will be studied: $\theta_m = 0^\circ$, 20° and 90° .

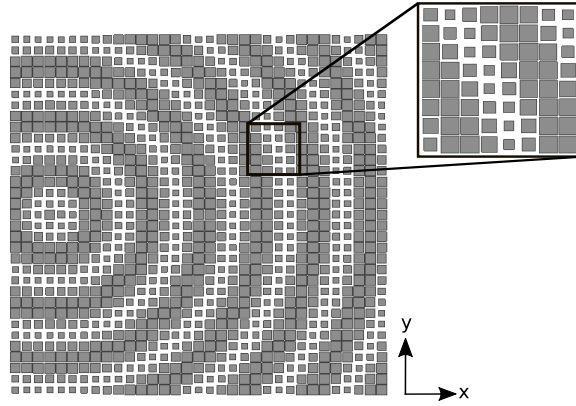


Figure 6.8: Example of a holographic pattern with square patches.

According to requirements of specific applications, the hologram can be configured to radiate in multi-beam direction in the range of GHz [71] and THz [49] frequencies, modifying the spatial distribution of the AIS. Also, a conical [72] and cylindrical [73] metasurface have been reported following the same theory of planar design.

The following sections present a step-by-step design of the surface wave feeding that will be used in the HAIA, divided into two types: *SIW H-sectoral and monopole of a quarter-wavelength*.

6.4

Modeling of the SIW H-sectoral Feeding

Some conventional methods of feeding in waveguides developed in PCB (Printed Circuit Board) are coaxial probe [63], microstrip line [74] and tapered microstrip line [75]. In this dissertation, the first two methods are aborbed, described in section 6.4.2 and 6.5, respectively. Table 6.3 presents the performance goals of the feeding for a comparative study among the proposed

designs. The values are chosen to generate a more directive surface wave, with the higher power transmitted at the feeding output.

Table 6.3: Design goals of the SIW H-sectoral.

Parameter	Specification
FTBR	greater than 30 dB
Reflection coefficient (S_{11})	lower than -20 dB
Gain	greater than 8 dB

6.4.1

Modeling of the Printed Transition Zone

In order to enhance the radiation performance of the SIW H-sectoral feeding, two types of transition zones are analyzed at the edge of the feeding: rectangular patches [63] and small triangles [64]. The last configuration is used for the first time in this kind of SIW configuration. The geometries are illustrated in figure 6.9.

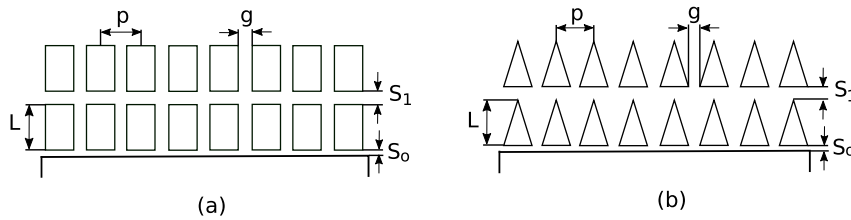


Figure 6.9: Transition zone in the SIW feeding with: (a) rectangular patches, and (b) small triangles.

Applying the equations defined in section 5.4 and parameterized on HFSS, table 6.4 presents the optimized values of the printed transition zone for the highest efficiency exhibited in the simulations.

Table 6.4: Parameters of the transition zone.

L [mm]	p [mm]	g [mm]	S_1 [mm]	S_o [mm]
3	2.2	0.6	0.7	0.2

6.4.2

Modeling of the SIW with Coaxial Probe

As explained in section 5.2.1, a coaxial probe is a very common feeding in conventional waveguides and horn antennas, furthermore it is an alternative connection in microstrip patch antennas. In the case of SIW technology, it is also used with straightforward implementation and a good impedance matching. The coaxial probe consists of an inner and outer conductor, where a recommended position as well as in conventional waveguides is $\lambda/4$ from one of the walls to avoid out-of-phase reflections as illustrated in figure 6.10.

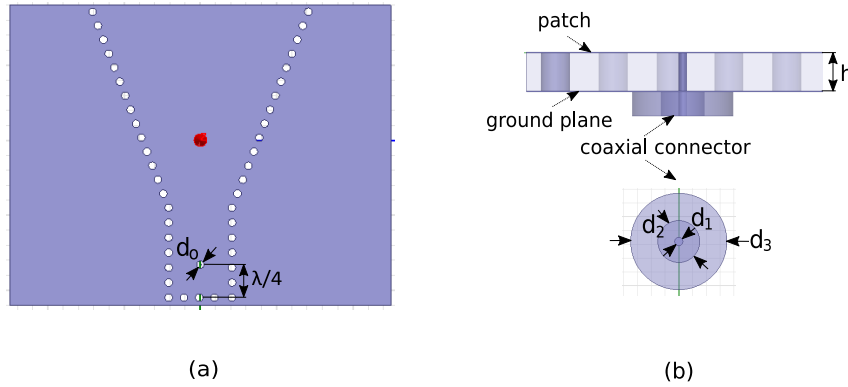


Figure 6.10: Coaxial probe technique: (a) top view, and (b) frontal view.

In the simulations, the coaxial probe is implemented with a waveport excitation and impedance of 50Ω . In this work, the inner conductor d_1 is inserted in a height h of the dielectric substrate without any contact with the top patch (a small isolation region d_o is used), the outer conductor d_3 is connected to the ground plane and d_2 is the dielectric component of the coaxial probe.

Table 6.5 presents the values optimized for the diameters d_1 , d_2 and d_3 , based on the improvement of the reflection coefficient (S_{11}) of the SIW structure tested in the simulations. The dimensions of the waveguide are solved by applying the equations (4-30), (5-3) and (5-8). In order to perform the proof of concept, the waveguide is modeled with an fundamental frequency (f_{10}) of 13 GHz.

Table 6.5: Parameters of the coaxial probe connection.

d_o [mm]	d_1 [mm]	d_2 [mm]	d_3 [mm]	h [mm]
1	0.38	1.52	3.5	1.57

The aperture of the SIW A and R_o is determined through the graphic shown in figure 5.5 to estimate the gain in the feeding. The dimensions of the structure are summarized in table 6.6.

Table 6.6: Parameters used in the simulations of the SIW H-plane feeding.

w_{eff} [mm]	a [mm]	d_{via} [mm]	l_{via} [mm]	A [mm]	R_o [mm]
8.3	7.3	1	1	28.30	26.15

In the following results, three structures are analyzed and compared: without transition zone, with a transition zone of rectangular patches and transition zone of small triangles as illustrated in figure 6.11. In this project, the transition zone is implemented only in the top copper of the dielectric substrate. The SIW feedings are modeled using the parameters of table 6.4, 6.5 and 6.6.

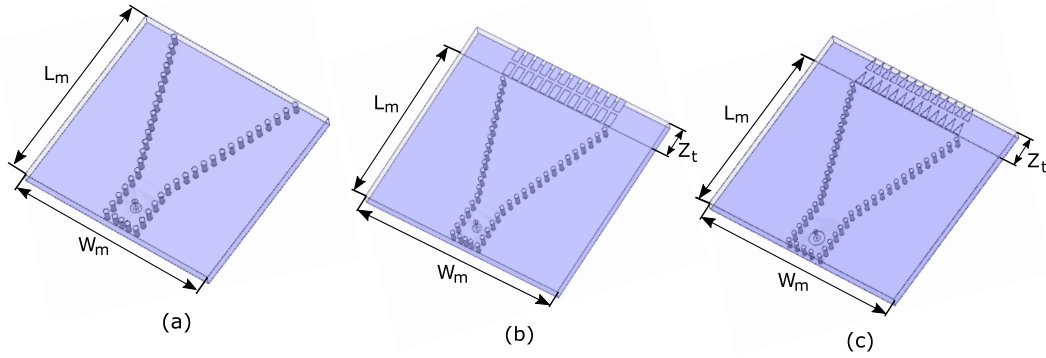


Figure 6.11: SIW H-plane feeding: (a) without transition zone, (b) transition zone of rectangular patches, and (c) transition zone of small triangles. Total dimension: $W_m = 50$ mm, $L_m = 40$ mm and $Z_t = 6.95$ mm.

The resonance frequencies of the three previous designs are presented in figure 6.12, analyzed from 13 GHz to 20 GHz, where the transition zone with small triangles shows the best performance. Additionally, the results are evaluated at the maximum resonance frequency of each structure summarized in table 6.7, where it shows the response of FTBR, reflection coefficient, and gain, demonstrating that the transition zone allows a better agreement between the parameters under study, and improving its values as reported in the literature. Furthermore, the best performance is obtained with the transition zone of small triangles, presenting a dual-band of operation: 15.9 - 16.5 GHz ($BW = 600$ MHz) and 18 - 18.8 GHz ($BW = 800$ MHz), with a maximum resonance frequency of 16.2 GHz and 18.4 GHz.

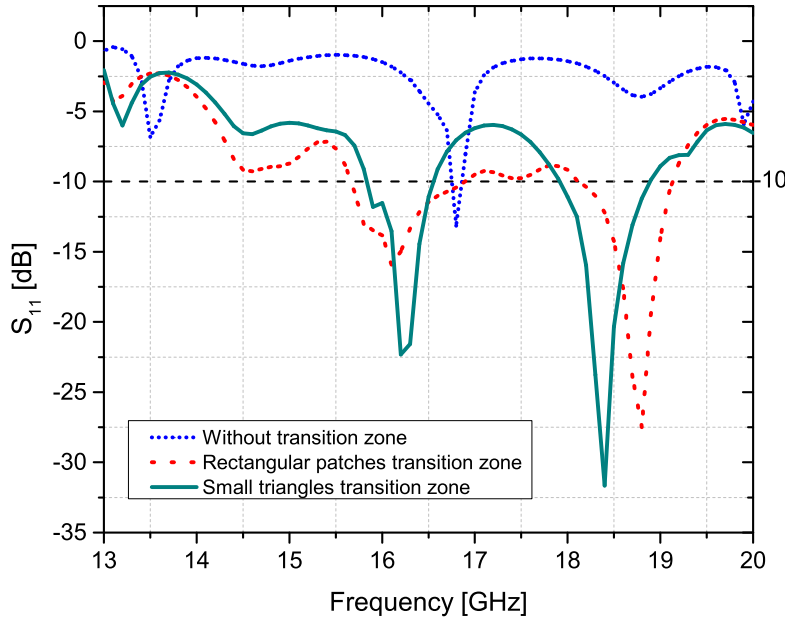


Figure 6.12: Comparative reflection coefficient results among the transition zones using coaxial probe connection.

Table 6.7: Performance results of the SIW structures with coaxial probe analyzed at the maximum resonance frequency.

Structure	FTBR [dB]	S_{11} [dB]	Gain [dB]	f_o [GHz]
Without transition zone	3.06	-13.15	2.67	16.8
Rectangular patches	25.14	-27.49	9.68	18.8
Small triangles	32.12	-31.64	9.42	18.4

The resonance frequencies of the SIW feeding can be controlled by the number of vias in the waveguide. In addition, the variation of the opening angle (ψ) allows to enhance the reflection coefficient, and the parameter S_o in the transition zone allows to control the magnitude of the FTBR parameter. Therefore, it is possible to adjust and scale the SIW feeding for other frequencies according to specific requirements.

Given the above results, in the following sections, the frequency of 18.4 GHz is chosen as the design frequency for the proof of concept of the HAIA. Figure 6.13 shows the distribution of the electric field inside the dielectric substrate and the 3-D radiation pattern, and figure 6.14 shows the comparative radiation pattern of the E-plane ($\phi = 0^\circ$) and the H-plane ($\theta = 90^\circ$) of the three previous designs in its maximum resonance frequency.

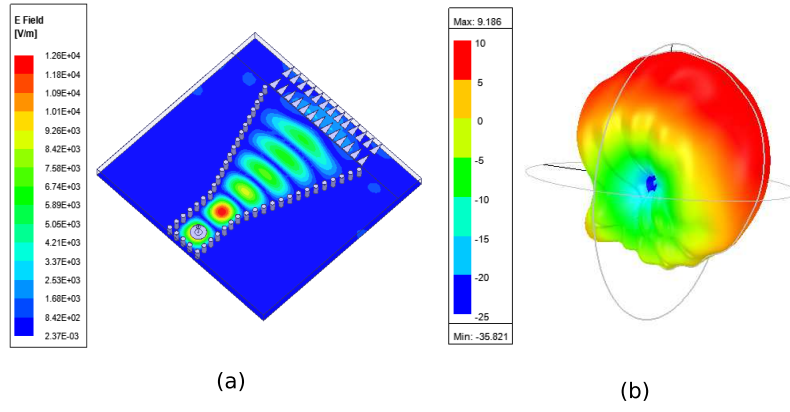


Figure 6.13: SIW structure with coaxial probe: (a) magnitude of the electric field, in V/m, and (b) 3-D radiation pattern, at $f_o = 18.4$ GHz.

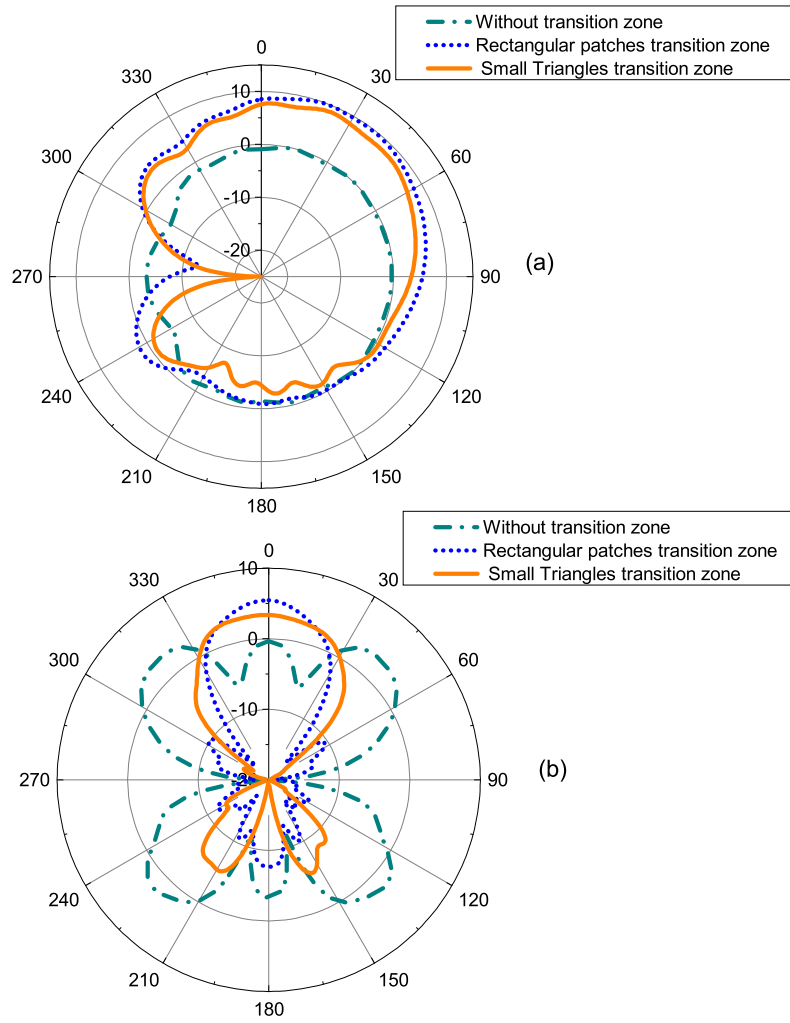


Figure 6.14: Comparative of the different structure SIW H-sectoral with coaxial probe connection: (a) E-plane ($\phi = 0^\circ$), and (b) H-plane ($\theta = 90^\circ$) at the maximum resonance frequency.

6.5

Modeling SIW with Microstrip Line

The microstrip line fed is very common in filters, couplers, microstrip antennas, and others [76], and aborded in this work as an alternative method to carry out the HAIA connection. Figure 6.15 shows the proposed microstrip line connected to the SIW H-sectoral. The microstrip line is configured with a width W_s and length L_s connected at the edge of the top copper trough the gaps of width W_g and length L_g to be excited with an impedance of $50\ \Omega$ using lumped port on HFSS. The use of gaps W_s is useful to increase the bandwidth of the feeding [59].

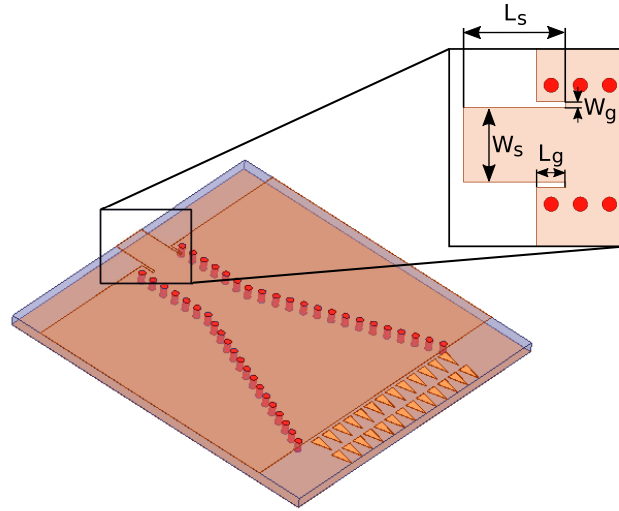


Figure 6.15: Microstrip line feeding.

The W_s and L_s parameters are solved with the ADS (Advanced Design System) calculator shown in table 6.8 for a dielectric substrate RT/duroid 5880 with electric permittivity $\epsilon_r = 2.2$, loss tangent $\tan\delta = 0.0009$, copper tickness of $35\mu\text{m}$ and height of 1.57 mm .

Table 6.8: Dimensions of the microstrip line.

W_s [mm]	L_s [mm]	L_g [mm]	W_g [mm]
5.2	7	2	0.4

As described in section 6.4.2, the fundamental frequency of the waveguide is chosen at 13 GHz with the transition zone of small triangles for the best result exhibited. Table 6.9 shows the parameter of the final structure. The reflection coefficient is also simulated at discrete frequencies from 13 GHz to 20 GHz , as shown in figure 6.16. Its is observed that there is a multi-band with

four maximum resonance frequencies with the highest bandwidth at 17.8 - 20 GHz (BW = 2.2 GHz). Therefore, this technique can be useful when a greater bandwidth is needed in the HAIA. With this kind of connection is obtained a gain of 9.18 dB, FTBR of 23.48 dB and reflection coefficient of -24.56 dB at $f_o = 18.4$ GHz.

Table 6.9: Parameters used in simulations for the SIW H-plane microstrip line.

w_{eff} [mm]	a [mm]	d_{via} [mm]	l_{via} [mm]	A [mm]	R_o [mm]
8.3	7.3	1	1	30.11	25.78

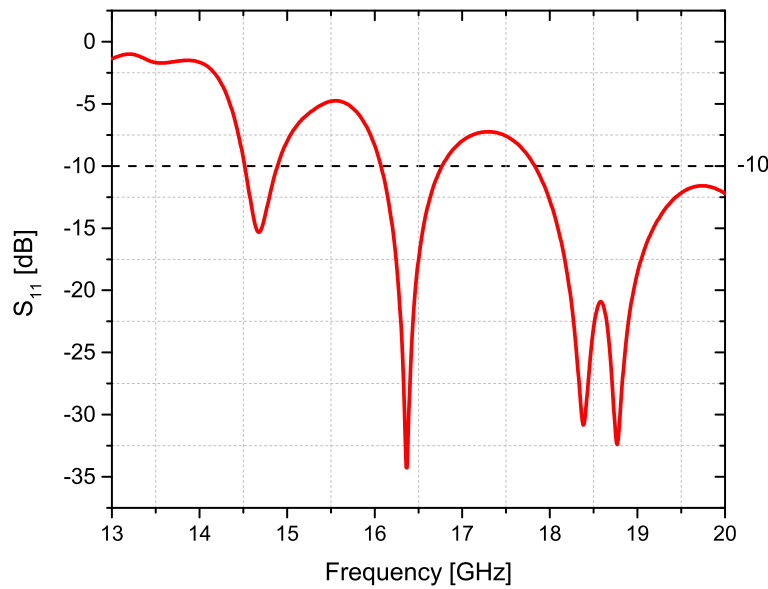


Figure 6.16: Simulated reflection coefficient for the SIW with microstrip line.

In the results is seen that the FTBR parameter and the reflection coefficient have lower values compared to the coaxial probe connection. Figure 6.17 shows the radiation pattern of the E-plane ($\phi = 0^\circ$) and H-plane ($\theta = 90^\circ$), where the E-plane and H-plane with the microstrip line have a higher level of side lobe (H-plane), in relation to the coaxial probe. However, some adjustment optimizations can be explored for future works. Figure 6.18 presents the behavior of the distribution of the electric field inside the substrate and the 3-D radiation pattern.

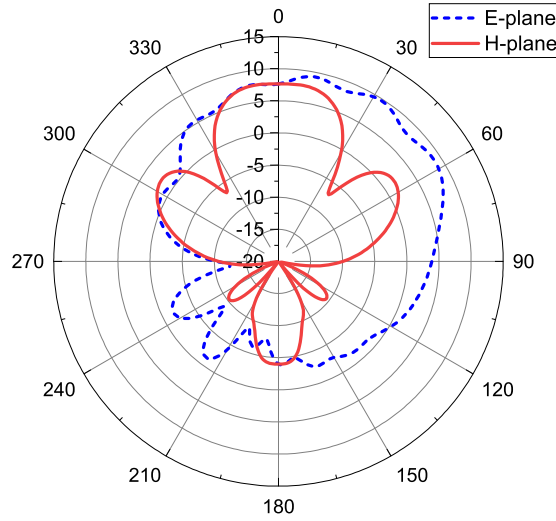


Figure 6.17: Radiation pattern of the SIW with microstrip line for the E-plane ($\phi = 0^\circ$) and H-plane ($\theta = 90^\circ$).

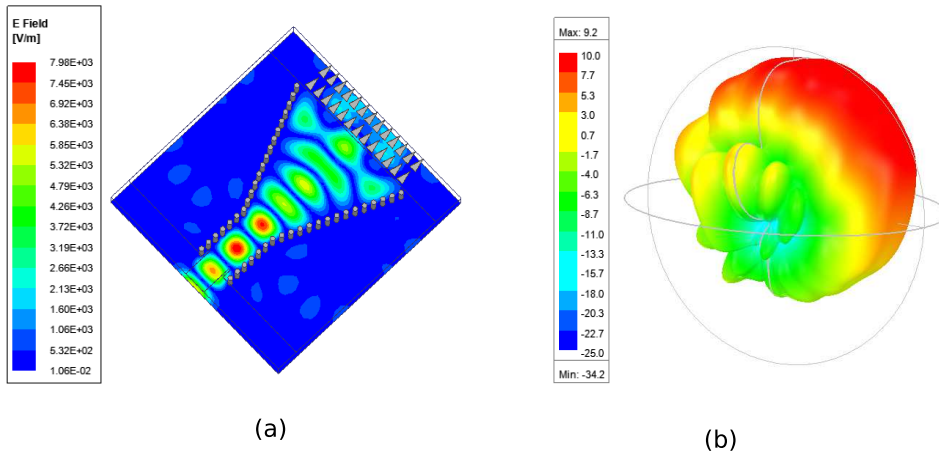


Figure 6.18: SIW structure with microstrip line: (a) magnitude of the electric field, in V/m, and (b) 3-D radiation pattern, at $f_o = 18.4$ GHz.

6.5.1

Modeling of the Monopole Feeding

The monopole is one of the first method used to generate a surface wave in the HAIA. Its configuration consists of a vertical conductor of a quarter-wavelength placed on the ground plane, radiating energy in an omnidirectional pattern as illustrated in figure 6.19.

To study the performance of this feeding, the design frequency of the monopole is chosen at 18.4 GHz as in the previous section. On HFSS, a lumped port excitation is configured with an impedance of 50Ω connected to a ground plane. The height of the monopole is $\lambda/4$ (4.1 mm), where λ is the wavelength

of the design frequency, with diameter $d_m = 0.3$ mm. Figure 6.20 presents the reflection coefficient of the simulated monopole from 13 GHz to 20 GHz. Lower values of the reflection coefficient are obtained in relation to the planar source studied.

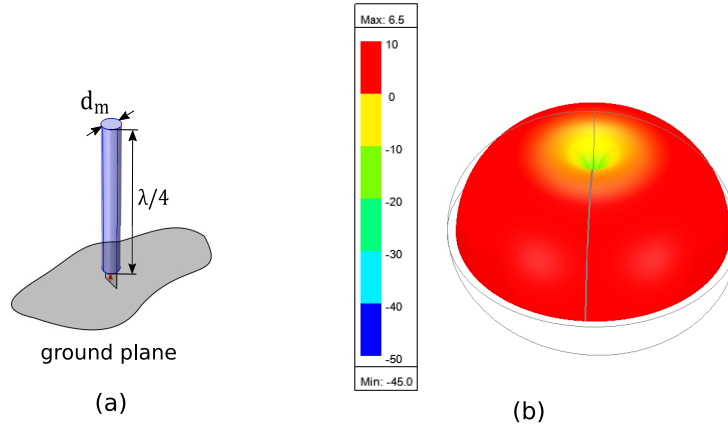


Figure 6.19: Monopole of a quarter-wavelength: (a) view of the structure, and (b) 3-D radiation pattern.

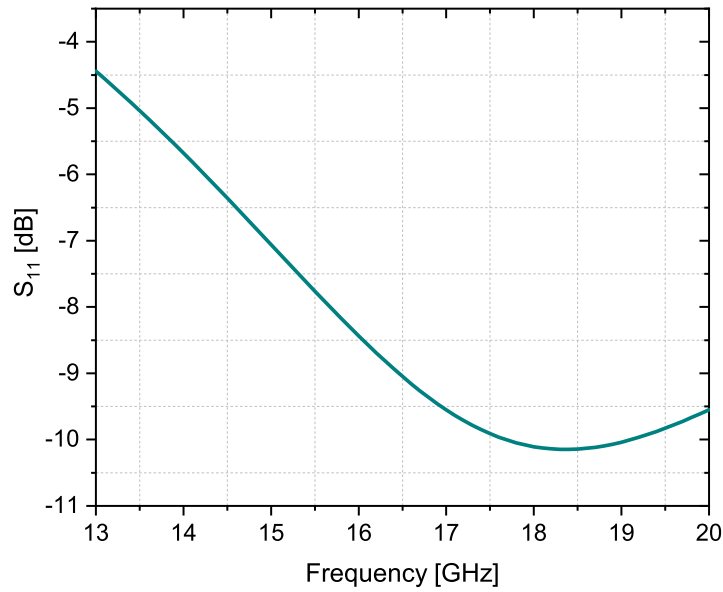


Figure 6.20: Simulated reflection coefficient of the monopole.

Finally, the simulations of the axial ratio parameter of the three feeding investigated are shown in figure 6.21. It is observed that in the region of maximum radiation of the feedings, the linear polarization behavior is dominant, capable of being used in the HAIA.

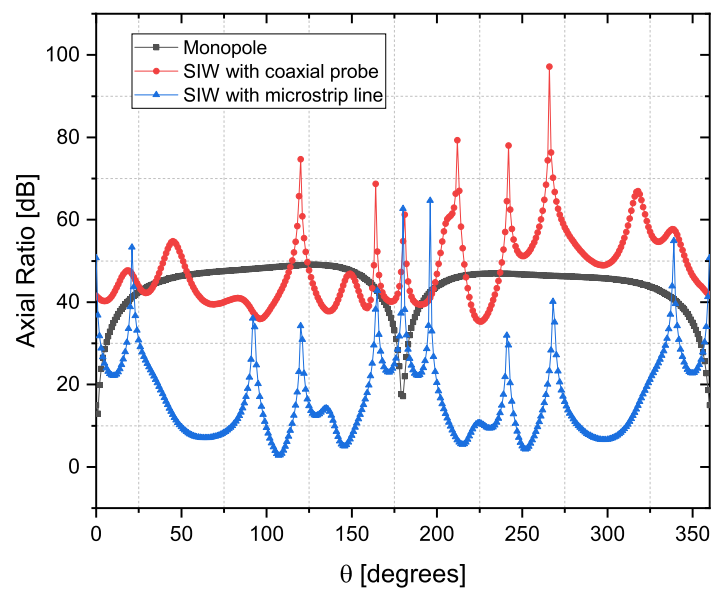


Figure 6.21: Comparative results of axial ratio among the types of feeding studied, at $f_o = 18.4$ GHz.

This chapter is dedicated to develop the HAIA, unifying the antenna components detailed in the previous chapter. The three types of feeding are simulated in the antenna, and the performance is compared. Also, variations are made in the dimensions of the holographic surface and changes in the maximum radiation angle to conclude the best results. Finally, a change in the polarization of the antenna is presented.

7.1

HAIA with SIW H-sectoral feeding

The HAIA is designed with the SIW H-sectoral feeding using a coaxial probe and microstrip line connection presented in sections 6.4.2 and 6.5, respectively. The printed transition zone used is the small triangles for the best results exhibited. The design frequency of 18.4 GHz is chosen as the proof of concept. Furthermore, the air box is configured with a radiation boundary at a distance of λ from the antenna. All the simulations are performed in the far-field region. A ground plane is used in the entire structure, and the antenna supports a TM surface wave mode.

7.1.1

Coaxial probe connection

The dimensions of the coaxial probe are shown in table 6.5. The SIW feeding is implemented with the parameters established in table 6.4 and 6.6, and the dimension of the coaxial probe corresponds to the values of table 6.5. Figure 7.1 shows the proposed design, with a sinusoidal holographic surface of length L_h and width W_h . In this kind of antennas, a common feeding position is at the focus of the concentric ellipses of the hologram. In this work, an optimized focus position is at a distance of $L_h/20$ and $W_h/2$ based on the parameters evaluated, such as gain and maximum radiation angle. In addition, different sizes of the holographic surface are simulated, which are described in table 7.1. For study purposes, the maximum radiation angle designed on the surface is 20° (θ_d), to radiate in the forward region.

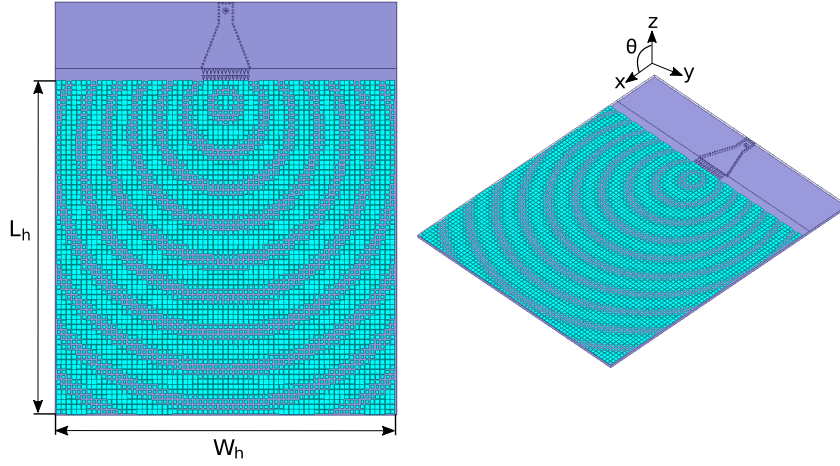


Figure 7.1: Simulated HAIA with SIW H-sectoral feeding coaxial probe connection, at $f_o = 18.4$ GHz and $\theta_d = 20^\circ$.

Table 7.1: Dimensions of the holographic surface tested.

L_h [cm]	W_h [cm]	No. of elements	Size
12	12	1,600	$7.36\lambda^2$
15	15	2,500	$9.20\lambda^2$
20	20	4,489	$12.26\lambda^2$
25	20	5,561	$15.30\lambda \times 12.26\lambda$
25	25	6,689	$15.30\lambda^2$

In table 7.1, the size of the holographic surface decreases from 40% to an increase of 25% concerning the dimensions $L_h = 20$ cm and $W_h = 20$ cm. The simulated maximum dimensions are $L_h = 25$ cm and $W_h = 25$ cm due to the computational limits of the resource used. Table 7.2 shows the performance results and the radiation pattern of the antenna for the five dimensions of the holographic surface tested.

Table 7.2: Performance of the HAIA with variation in the holographic surface dimension at $f_o = 18.4$ GHz.

L_h [cm]	W_h [cm]	S_{11} [dB]	Gain [dB]	θ_m [°]	HPBW [°]	SLL [dB]
12	12	-18.73	18.19	21	7.33	-2.62
15	15	-19.99	20.13	22	5.70	-5.25
20	20	-19.40	22.02	23	4.71	-8.18
25	20	-19.59	23.06	24	3.99	-12.38
25	25	-19.31	23.18	25	4.03	-13.31

The evaluated parameters are the reflection coefficient (S_{11}), gain, maximum radiation angle (θ_m), HPBW along the E-plane, and side lobe level (SLL)

measured in the appearance of the first side lobe. The radiation pattern is plotted for an xz plane, E-plane ($\phi = 0^\circ$), which contains the direction of maximum radiation. The results shown in figure 7.2 have the same behavior as reported in the literature for this kind of antenna [4], [25], [77], [43]. Figure 7.3 shows the lower and higher dimensions for a better resolution of the results among them.

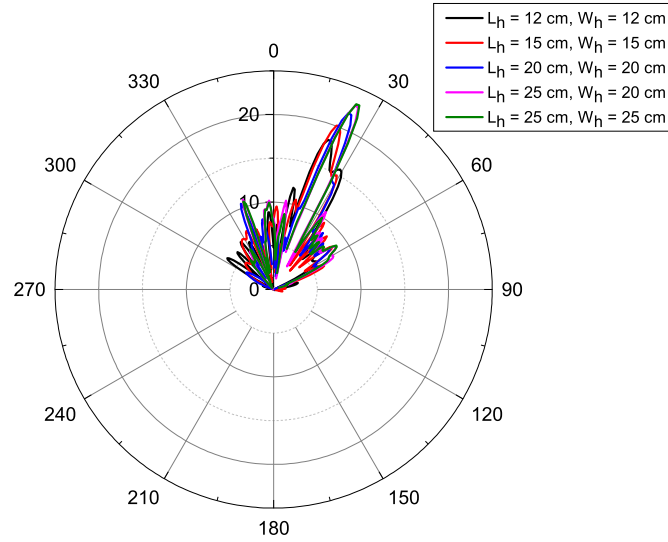


Figure 7.2: Radiation Pattern E-plane ($\phi = 0^\circ$) for different dimensions of the HAIA at $f_o = 18.4$ GHz with coaxial probe connection, maximum gain of 23.18 dB.

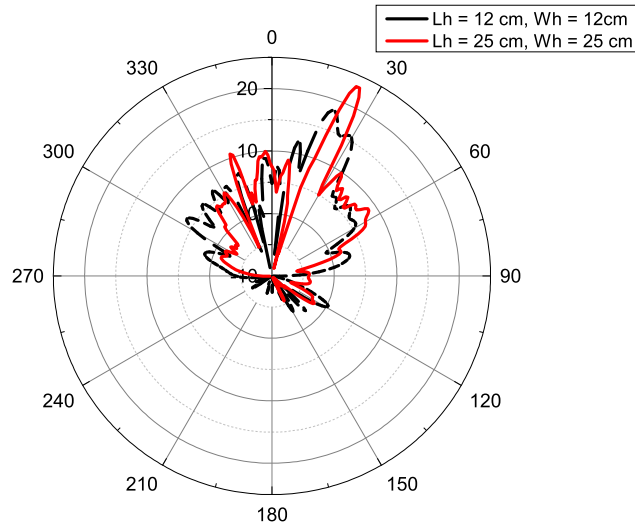


Figure 7.3: Radiation Pattern E-plane ($\phi = 0^\circ$) for the lower and higher dimensions of the HAIA at $f_o = 18.4$ GHz with coaxial probe connection, maximum gain of 23.18 dB.

Figure 7.4 shows the 3-D radiation pattern for the holographic surface of $12.26\lambda^2$.

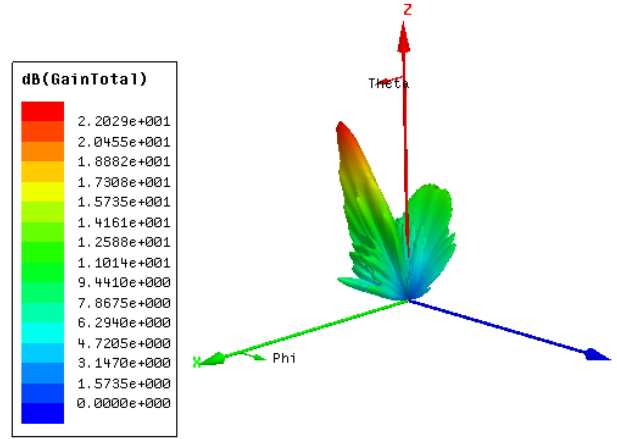


Figure 7.4: 3-D radiation pattern for the HAIA with coaxial probe connection at $f_o = 18.4$ GHz.

The following simulated results are obtained:

- An increase in the size of the holographic surface represents a higher number of square elements. Consequently, it requires a higher computational resource and longer solution time;
- It is observed when the dimensions increase, the gain also increases as exhibited in [31]. The radiation pattern with the highest dimension ($L_h = 25$ cm, $W_h = 25$ cm) shows an increase in gain and lower levels in the side lobes of -13.31 dB below the main beam, presenting acceptable values reported for this kind of antennas [12]. The reflection coefficient of the antenna does not change abruptly with the size variation;
- The maximum radiation angle (θ_m) has an increase of 1° with respect to the design angle (θ_d) when the size increases. This can be compensated by adjusting the impedance parameter X_s on the holographic surface [43];
- A variation of the attenuation constant can be used to control the side lobe levels by varying the impedance parameter M on the holographic surface [43];
- HPBW values lower than 5° are obtained from the dimension of L_h , $W_h = 20$ cm. [25], [43];
- Given the above results, the minimum physical area of the holographic surface that fulfills the design requirements defined in table 6.1 is $12.26\lambda^2$. Therefore, that proportion is chosen for the proof of concept, considering a fabrication-friendly employment and lower cost of manufacture of the final prototype.

Figure 7.5 shows the simulated reflection coefficient of the HAIA (size of $12.26\lambda^2$) using discrete frequencies on HFSS, compared to the reflection coefficient of the SIW feeding without the holographic surface.

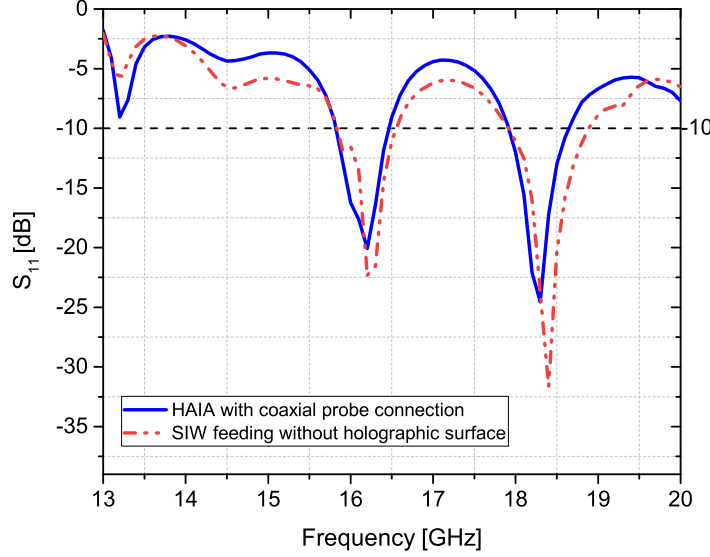


Figure 7.5: Comparative result of reflection coefficient between the HAIA with coaxial probe connection (size of $12.26\lambda^2$) and the SIW feeding.

A good agreement of the parameter S_{11} is observed for both structures, and dual operating bands are found in the antenna: 15.9 - 16.4 GHz ($BW = 500$ MHz) and 18.0 - 18.6 GHz ($BW = 600$ MHz). Figure 7.6 shows the distribution of the magnitude of the electric field (V/m) and the magnitude of the surface current (A/m) in the antenna at $f_o = 18.4$ GHz.

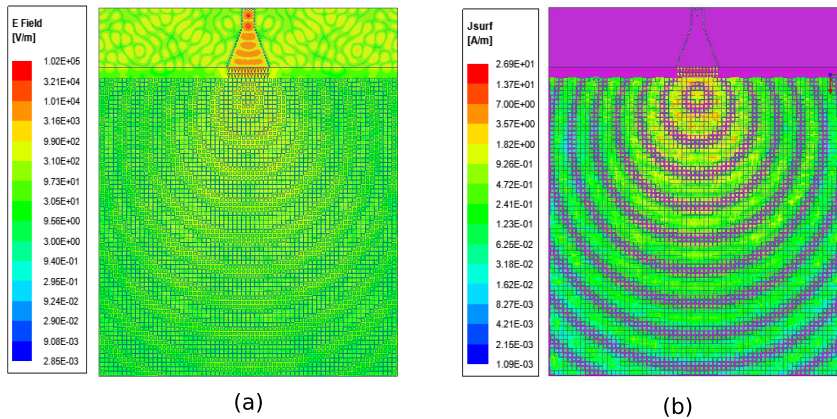


Figure 7.6: Distribution of the (a) magnitude of electric field, in V/m, and (b) magnitude of the surface current, in A/m, at $f_o = 18.4$ GHz and $\theta_d = 20^\circ$.

The surface current is present in the whole holographic surface, where it is observed that, in the focus of the hologram, there is a higher intensity of the

surface current, vanishing until reaching the opposite edge of the antenna. In figure 7.7 is shown the radiation pattern in the co-polarization component of the gain in the E-plane ($\phi = 0^\circ$).

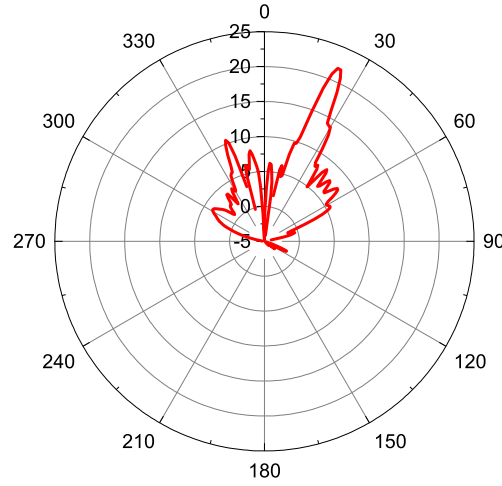


Figure 7.7: Radiation pattern SIW H-sectoral with coaxial probe, E-plane ($\phi = 0^\circ$) at $f_o = 18.4$ GHz, maximum gain of 22.02 dB at $\theta_m = 23^\circ$.

The cross-polarization of the gain is shown in figure 7.8. For the distribution of the AIS in this antenna, the co-polarization represents the radiation pattern in the vertical polarization being the reference polarization of the electric field. The cross-polarized component of the gain has a low value of -38.23 dB at $\theta_m = 23^\circ$.

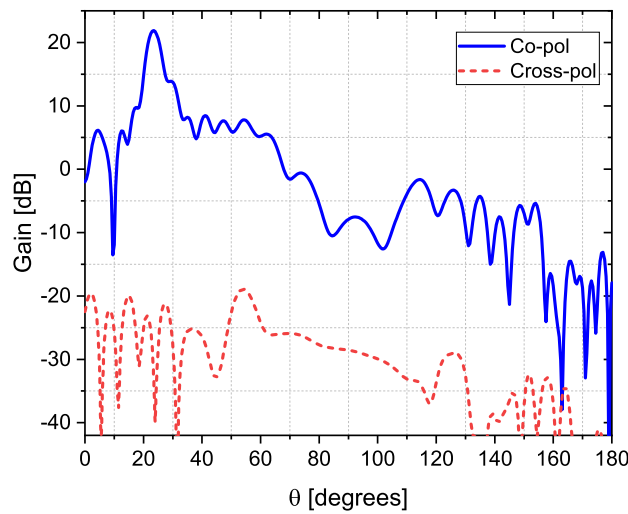


Figure 7.8: Radiation pattern for the co- and cross- polarization component of the gain at $f_o = 18.4$ GHz, HAIA with coaxial probe connection.

7.1.2 Frequency-controlled Beam Scanning

In order to explore the frequency response scanning of the HAIA with the coaxial probe connection, discrete frequencies are simulated on HFSS in the two frequency ranges previously defined, which are 15.9 GHz to 16.4 GHz, and 18 GHz to 18.6 GHz. Figure 7.9 shows the frequency scanning in the first band of the antenna with a variation in the maximum radiation angle when the frequency varies. The lowest frequency has a maximum gain of 18.2 dB at $\theta_m = 13.5^\circ$ and the highest frequency a maximum gain of 18.72 dB at $\theta_m = 16^\circ$. Figure 7.10 shows the radiation patterns in the whole band and table 7.3 summarizes its performance parameters.

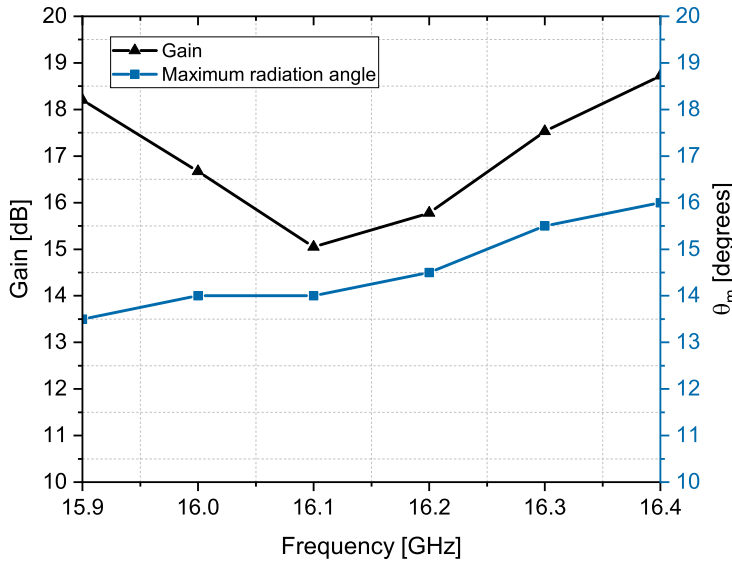


Figure 7.9: Gain versus frequency and maximum radiation angle in the firsts operating band, with scanning range from 13.5° to 16° .

Table 7.3: Performances parameter of the antenna in the first operating band, simulated in the E-plane ($\phi = 0^\circ$).

f_o [GHz]	S_{11} [dB]	Gain[dB]	θ_m [°]	HPBW[°]	SLL[dB]	Cross-pol[dB]
15.9	-12.50	18.20	13.5	4.39	-7.26	-33.13
16.0	-15.95	16.67	14.0	4.04	-5.87	-30.50
16.1	-33.39	15.05	14.0	3.47	-4.38	-33.39
16.2	-19.97	15.78	14.5	4.40	-4.60	-46.21
16.3	-16.48	17.53	15.5	3.63	-5.81	-36.05
16.4	-12.02	18.72	16.0	4.52	-6.61	-35.83

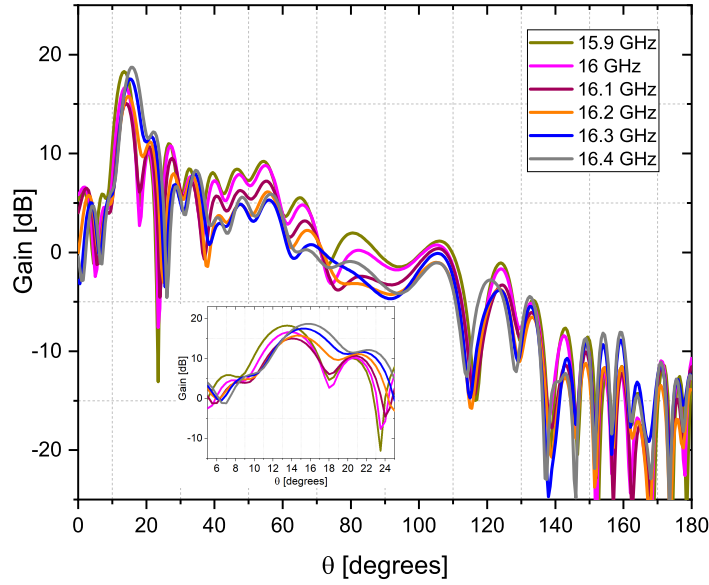


Figure 7.10: Radiation pattern of the first band, E-plane ($\phi = 0^\circ$).

Figure 7.11 presents the frequency scanning in the second band of the antenna, with a variation in the maximum radiation angle when the frequency varies. The lowest frequency has a maximum gain of 22.45 dB at $\theta_m = 22^\circ$ and the highest frequency a maximum gain of 21.99 dB at $\theta_m = 24^\circ$. Figure 7.12 shows the radiation patterns in the whole band and table 7.4 summarizes its performance parameters. The maximum angle increases for each 300 MHz frequency increase, without an abrupt change in the gain value.

Table 7.4: Simulation results of the frequencies in the second band, E-plane.

f_o [GHz]	S_{11} [dB]	Gain[dB]	θ_m [$^\circ$]	HPBW[$^\circ$]	SLL[dB]	Cross-pol[dB]
18.0	-11.15	22.45	22	4.39	-10.33	-46.79
18.1	-14.98	22.55	22	4.04	-10.01	-43.70
18.2	-22.10	22.45	23	3.47	-9.36	-39.72
18.3	-23.29	22.13	23	4.40	-8.45	-38.23
18.4	-16.85	22.02	23	3.63	-8.18	-38.23
18.5	-12.98	22.09	24	4.52	-7.80	-42.26
18.6	-10.79	21.99	24	4.57	-7.36	-45.57

Given the above results, the radiation pattern in the first band presents a higher side lobe level. This can be due to the HAIA is designed at the frequency of 18.4 GHz and abrupt changes in the operating frequency can affect the performance of the antenna. Therefore, the best performance is found in the second band of the antenna.

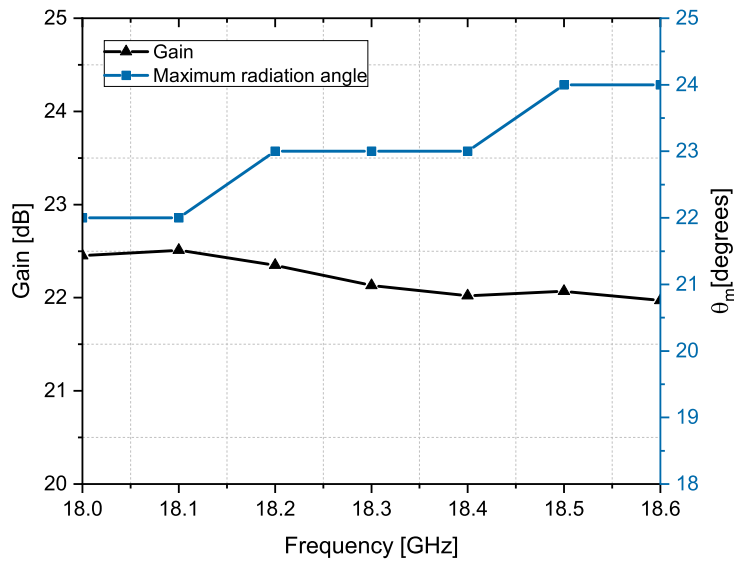


Figure 7.11: Gain versus frequency and maximum radiation angle in the second operating band, with scanning range from 22° to 24° .

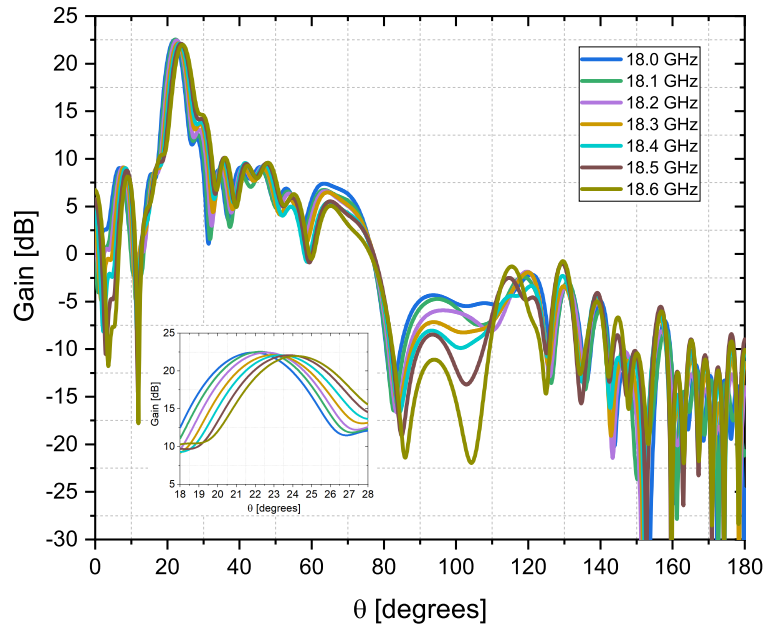


Figure 7.12: Radiation pattern of the second band, E-plane ($\phi = 0^\circ$).

7.1.3 VSWR

Figure 7.13 shows comparative values of VSWR between the HAIA with coaxial probe connection and the SIW feeding without the holographic surface

in the bandwidth of interest (18 - 18.6 GHz), presenting acceptable values in the whole band ($VSWR < 2$).

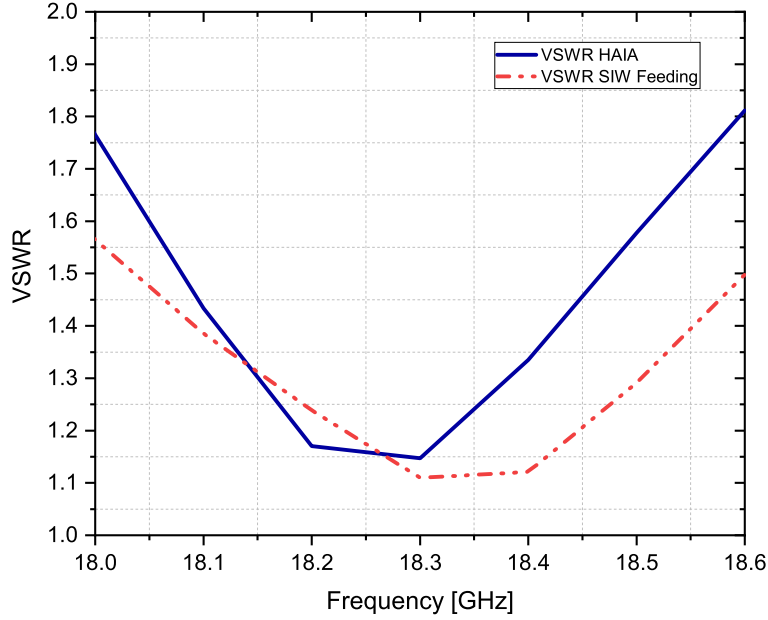


Figure 7.13: Comparative result of VSWR between the HAIA and the SIW feeding.

7.1.4 Microstrip line connection

In addition, a microstrip line is used as the feeding point of the HAIA. The design of the feeding follows the parameters presented in section 6.5. In order to compare the performance with the coaxial probe connection, only the frequency of $f_o = 18.4$ GHz is simulated at $\theta_d = 20^\circ$, keeping the same distribution of the AIS to excite a TM surface wave mode on the surface. The proposed structure is shown in figure 7.14, and table 7.5 summarizes the simulated results of the HAIA. Figure 7.15 and 7.16 show the co-and cross-polarization components of the gain.

Table 7.5: Performance results of the HAIA with microstrip line at $f_o = 18.4$ GHz.

f_o [GHz]	S_{11} [dB]	Gain[dB]	θ_m [°]	HPBW[°]	SLL[dB]	Cross-pol[dB]
18.4	-12.58	21.81	24	5.16	-6.62	-41.19

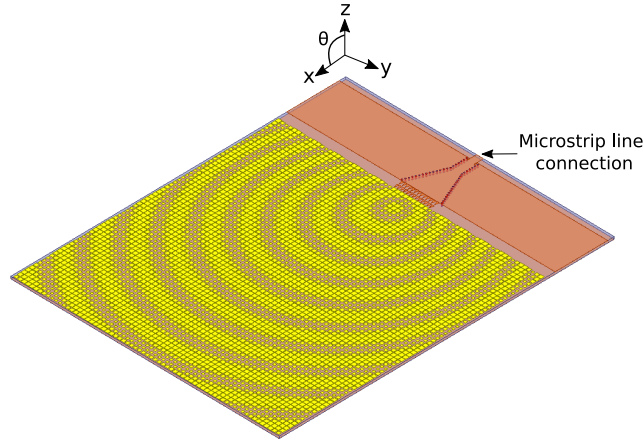


Figure 7.14: HAIA with microstrip line feeding, size of $12.26\lambda^2$, at $f_o = 18.4$ GHz and $\theta_d = 20^\circ$.

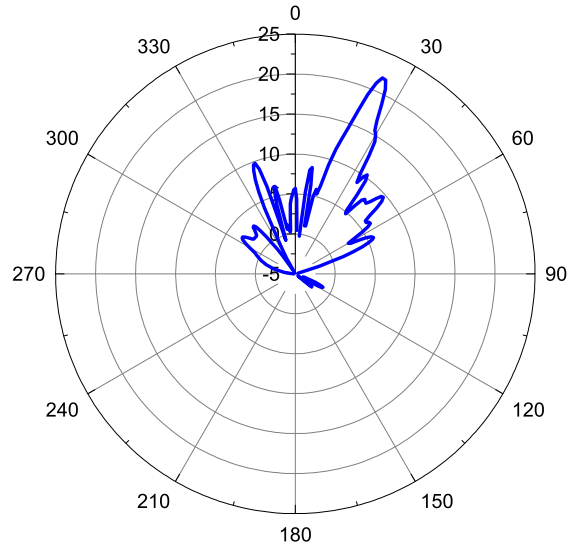


Figure 7.15: Simulated radiation pattern of the E-plane ($\phi = 0^\circ$) of the HAIA using microstrip line at $f_o = 18.4$ GHz, with maximum gain of 21.81 dB at $\theta_m = 24^\circ$.

Given the results exhibited, the HAIA with microstrip line has a good performance according to the parameters evaluated, however, the side lobe level is higher for the configuration used about the result obtained for the coaxial probe connection. The other parameters, such as the reflection coefficient, gain, HPBW, and cross-polarization, have acceptable operating values.

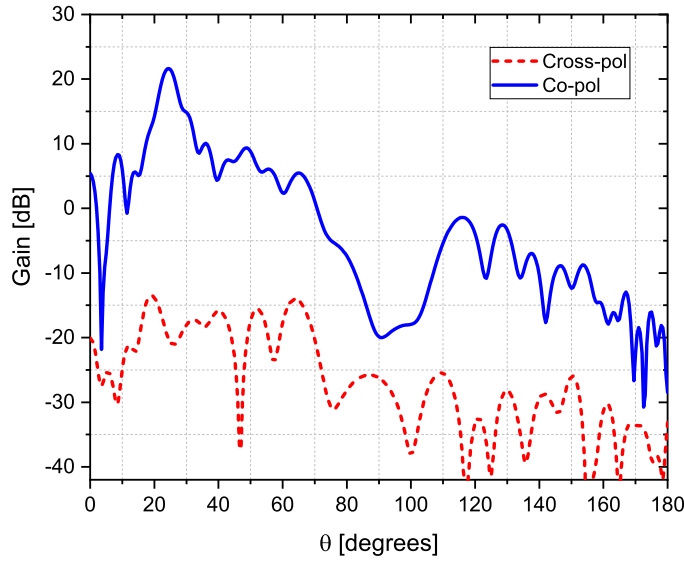


Figure 7.16: Radiation pattern for the co- and cross- polarization component of the gain at $f_o = 18.4$ GHz, HAIA with microstrip line connection.

7.2 HAIA with Monopole Feeding

A monopole of a quarter-wavelength is used to excite a TM surface wave mode on the antenna, as shown in figure 7.17. Initially, the holographic surface is set to dimensions of $12.26\lambda^2$. With the purpose to evaluate the influence of the monopole position in the HAIA, the monopole is varied by three points along the x -axis: $L_h/6$, $L_h/4$ and $L_h/2$, coinciding with the focus of the hologram. The position in y -axis is kept constant in $W_h/2$. The design frequency in all three cases is 18.4 GHz.

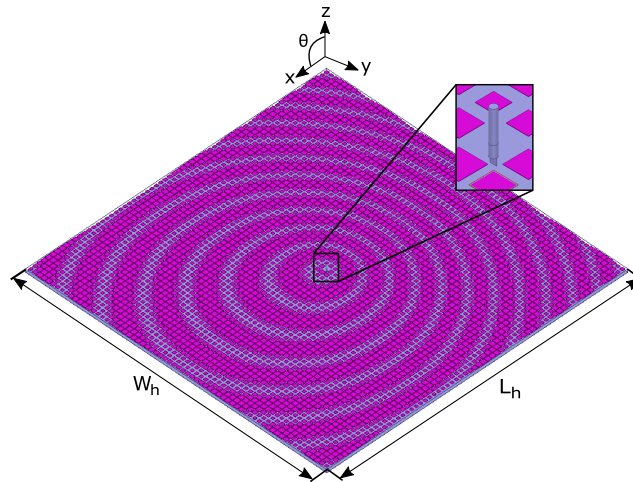


Figure 7.17: Holographic antenna with monopole feeding, size of $12.26\lambda^2$, at $f_o = 18.4$ GHz and $\theta_d = 20^\circ$.

Figure 7.18 shows the gain results obtained from the three configurations described above, where the monopole position is varied. In table 7.6 are summarized the results of the performance parameters in the three scenarios.

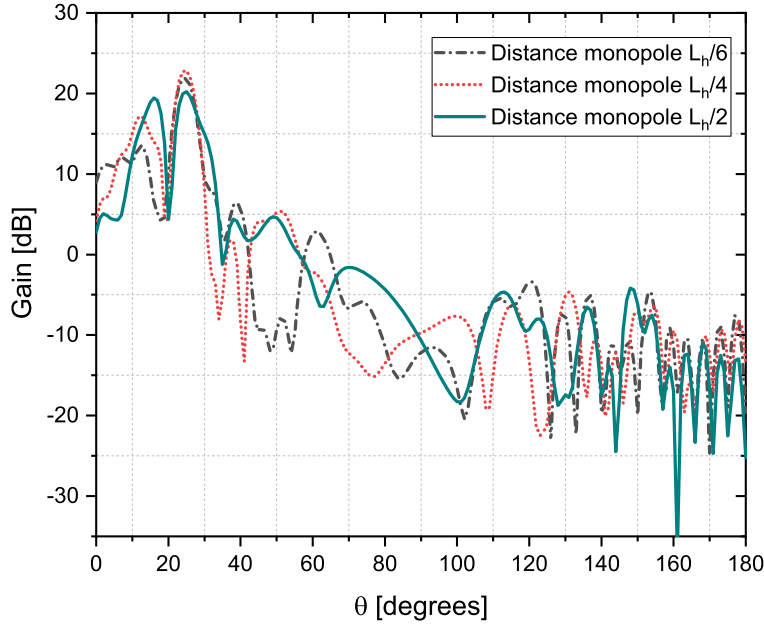


Figure 7.18: Comparative gain result of the HAIA with monopole feeding for variation in the focus position, size of $12.26\lambda^2$, at $f_o = 18.4$ GHz.

Table 7.6: Performance parameters of the HAIA at $f_o = 18.4$ GHz with monopole feeding.

Configuration	S_{11} [dB]	Gain[dB]	θ_m [°]	SLL[dB]
$L_h/6$	-11.05	21.87	25	-8.39
$L_h/4$	-11.42	22.81	25	-5.60
$L_h/2$	-11.03	22.02	25	-2.57

The following simulated results are obtained:

- The gain result in the three positions of the monopole is higher than 20 dB. A more uniform distribution of the radiation pattern is obtained with the parameter $L_h/2$, this is because the omnidirectional radiation of the monopole requires a central position on the surface to improve the distribution of the surface wave;
- The maximum beam direction in $L_h/2$ is 25° and a split appeared in the direction of the maximum beam [2]. According to the simulated schemes,

the phenomenon of the split can disappear with a higher dimension of the holographic surface.

Thus, an increase of 25% in the holographic surface dimension ($15.33\lambda^2$) is simulated to improve the performance of the antenna. Table 7.7 presents its results and figure 7.19 shows a comparative radiation pattern between the antenna with monopole and SIW feeding with the same size ($15.33\lambda^2$).

Table 7.7: Performance parameters of the HAIA with monopole, size of $15.33\lambda^2$, at $f_o = 18.4$ GHz.

f_o [GHz]	S_{11} [dB]	Gain[dB]	θ_m [°]	HPBW[°]	SLL[dB]	Cross-pol[dB]
18.4	-10.31	23.89	21	5.0	-2.30	-35.45

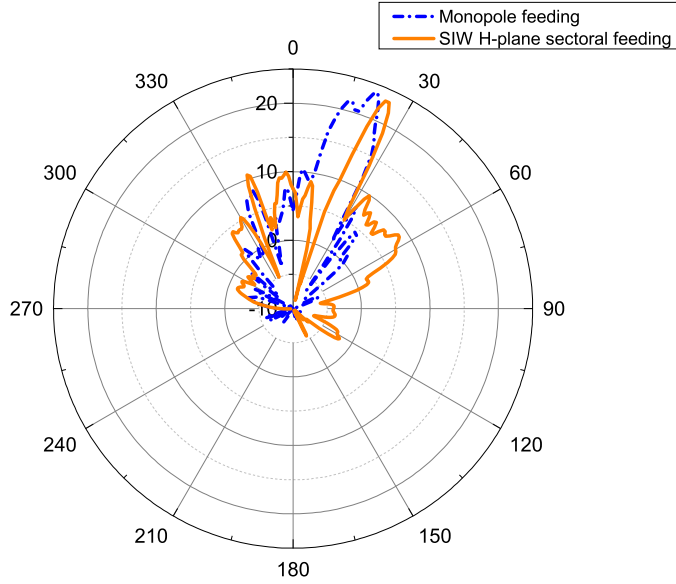


Figure 7.19: Comparative radiation pattern, E-plane ($\phi = 0^\circ$) of the holographic antenna with monopole feeding and SIW H-plane sectoral (size of $15.33\lambda^2$ in both structures).

The results show that the HAIA with monopole has a width HPBW and higher side lobe level (SLL) concerning the SIW H-sectoral feeding. Also, as seen in figure 7.18 and 7.19, when the size of the holographic surface increases, a higher directivity is obtained and, therefore, to generate a narrower beam using the monopole feeding it will be necessary to increase the size of the holographic surface. Figure 7.20 shows the distribution of the magnitude of the electric field and the magnitude of the surface current for the monopole with a size of $15.33\lambda^2$.

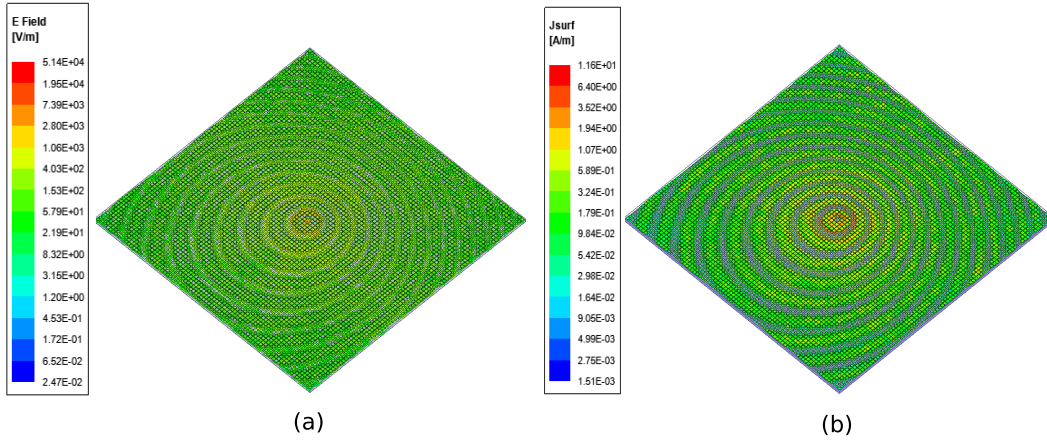


Figure 7.20: Distribution of the (a) magnitude of the electric field, in V/m, and (b) magnitude of the surface current, in A/m, size of $15.33\lambda^2$, at $f_o = 18.4$ GHz.

7.3 HAIA with Horizontal Polarization

Another characteristic explored in the HAIA is the change to horizontal polarization developed in [25], where the holographic surface is designed 180° out-of-phase in one of its halves ($W_h/2$) to support the propagation of a TE surface wave mode to radiate the horizontally polarized electric field. The antenna design performed is illustrated in figure 7.21.

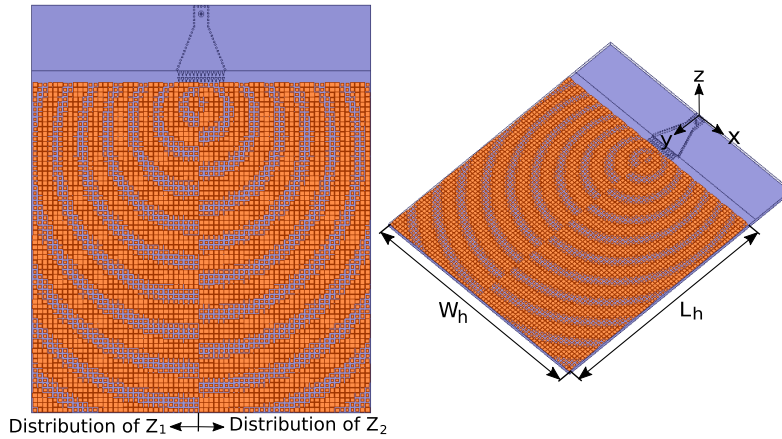


Figure 7.21: Holographic surface with 180° out-of-phase, for horizontal polarization, at $f_o = 18.4$ GHz and $\theta_d = 20^\circ$.

The purpose of the out-of-phase modification is to improve the magnitude of the horizontal component of the electric field performed through the distribution equation of the surface impedance in Z_{s1} and Z_{s2} as described below.

$$Z_{s1} = j[X_s + MRe(e^{-jk_x \sin(\theta_d)} e^{jknr})], x < 0, \quad (7-1)$$

$$Z_{s2} = j[X_s + MRe(e^{j\pi} e^{-jk_x \sin(\theta_d)} e^{jknr})], x > 0. \quad (7-2)$$

In figure 7.22, it is shown the result of the co- and cross-polarized components of the gain. For this modified holographic surface, the co-polarization represents the radiation pattern in the horizontal polarization being the reference polarization of the electric field. An improvement of the magnitude in the horizontal polarization is found with a gain of 6.67 dB. However, for this configuration, the cross-polarized values remain high.

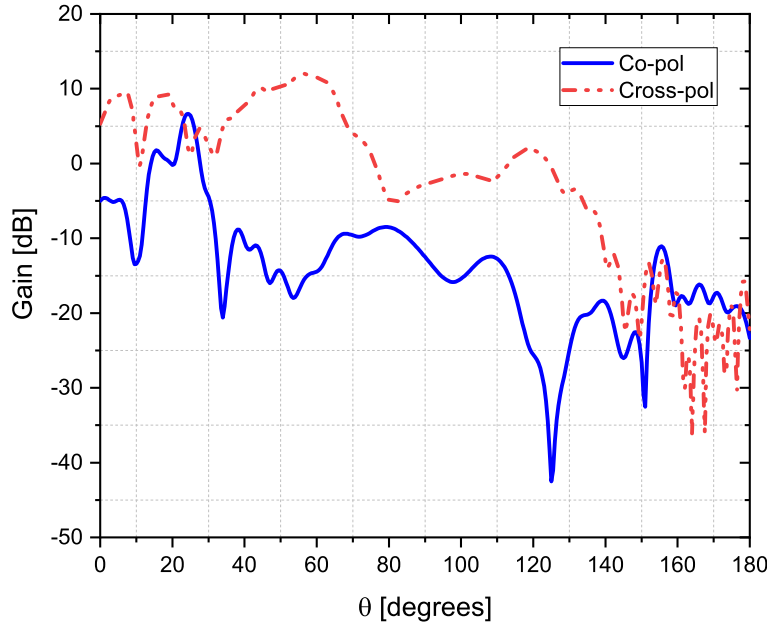


Figure 7.22: Radiation pattern of the co- and cross-polarization components of the gain, E-plane ($\phi = 0^\circ$), horizontal polarization, size of $12.26\lambda^2$, at $f_o = 18.4$ GHz.

The upper dimension of $15.33\lambda^2$ in the holographic surface is used to explore the reduction of the cross-polarization component of the gain. With this change, the magnitude of the gain in the co-polarization component increases to 8.89 dB as seen in figure 7.23. However, the cross-polarization is still high. Furthermore, the variation of the impedance parameters of the surface distribution is widely explored to decrease the gain in the cross-polarization [43], [25].

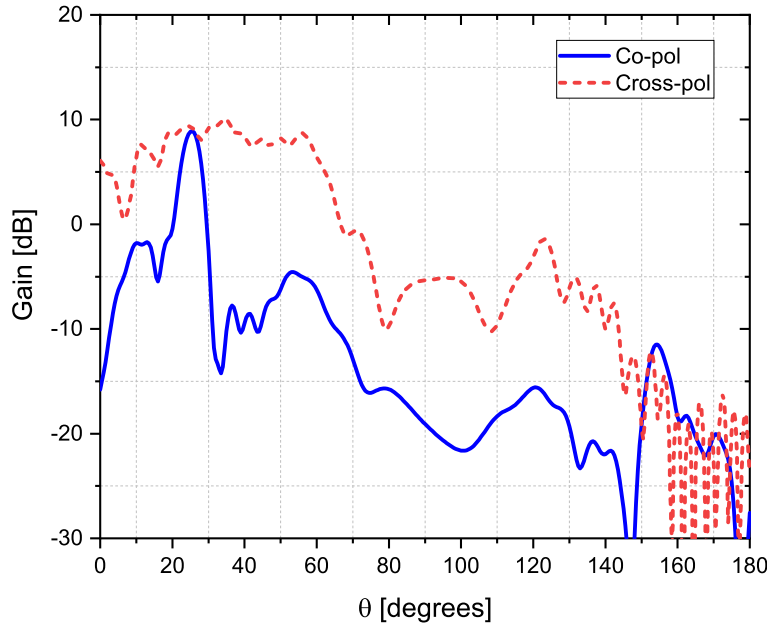


Figure 7.23: Radiation pattern of the co- and cross-polarization components of the gain, E-plane ($\phi = 0^\circ$), horizontal polarization, size of $15.33\lambda^2$, at $f_o = 18.4$ GHz.

7.4

Conclusion of the Proposed Designs

The designed models of the HAIA are summarized below:

- Design 1: HAIA with coaxial probe connection (holographic size of $12.26\lambda^2$);
- Design 2: HAIA with microstrip line connection (holographic size of $12.26\lambda^2$);
- Design 3: HAIA with monopole feeding (holographic size of $15.33\lambda^2$);
- Design 4: Horizontally polarized HAIA (holographic size of $15.33\lambda^2$).

Table 7.8 presents a summary of the radiation performance of all four antennas. The designs 1, 2 and 3 fulfill with the established goals for a vertically polarized electric field with low cross-polarization component of the gain. The design 4 for a horizontally polarized electric field, the cross-polarization is high and has a difference of 5° respect to the design angle of radiation. The HAIA with coaxial probe connection presents the best performance using a smaller dimension, leading to a miniaturization process. This final prototype is chosen to be manufactured and measured as proof of concept.

Table 7.8: Comparison of results between the modeled designs.

Design	Gain[dB]	θ_m [°]	HPBW[°]	SLL[dB]	Cross-pol[dB]	No. Elem
Des. 1	22.02	23	3.63	-8.18	-38.23	4,489
Des. 2	21.81	24	5.16	-6.62	-41.19	4,489
Des. 3	23.89	21	5.0	-2.30	-34.45	6,689
Des. 4	8.89	25	5.50	-10.68	-0.32	6,689

Table 7.9 presents a comparison of the final prototype with other works. It is noted that the SIW feeding allows reducing the surface size without a negative effect on the aperture efficiency of the antenna. The above due to the directivity of the surface wave. Also, a narrower beamwidth is presented in this work.

Table 7.9: Comparative results with other works.

Parameter	This work	[77]	[2]	[4]
f_o	18.4 GHz	20 GHz	17 GHz	10 GHz
Supported mode	TM	TM	TM	TE
Aperture size	$12.26\lambda^2$	$17.33\lambda^2$	$14.43\lambda \times 23.09\lambda$	$76.8\lambda^2$
No. Elem	4,489	5,721	–	3,600
Type of feeding	Planar SIW	Planar SIW	Monopole	Monopole
Gain	22.02 dB	23.73 dB	20 dB	16 dB
SLL	-8.18 dB	-13.12 dB	–	-20 dB
Cross-pol	-38.23 dB	–	–	–
HPBW	3.63°	4.6°	–	–
Scanning range	22° to 24°	18.7° to 43.6°	–	–
Aperture eff.	8.42%	6.25%	2.40%	5.85%

7.5

Change in the Design Radiation Angle

In order to explore the behavior of the antenna at the limits of the forward radiation, other design angles (θ_d) on the holographic surface are tested at 0° and 90° . The formed holographic surface is shown in figure 7.24 for dimensions of $12.26\lambda^2$ at $f_o = 18.4$ GHz. Figure 7.25 shows the radiation patterns for the design angle of 0° , where the maximum radiation angle is 4° with a gain of 22.87 dB. Figure 7.26 presents the radiation pattern for the design angle at 90° , where the leaky-wave radiation is observed pointing to the designed angle. Table 7.10 summarizes the performance parameters.

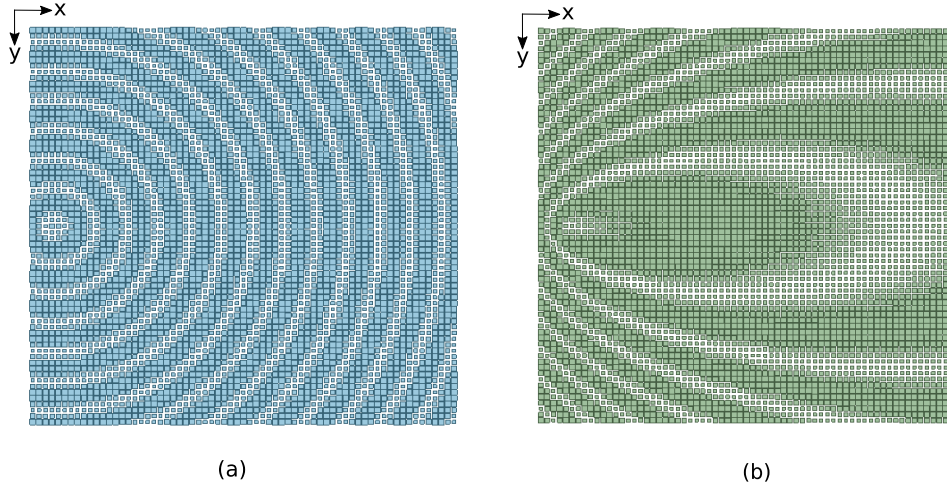


Figure 7.24: Radiation angle tested on the holographic surface: (a) $\theta_d = 0^\circ$, and (b) $\theta_d = 90^\circ$, size of $12.26\lambda^2$ at $f_o=18.4$ GHz.

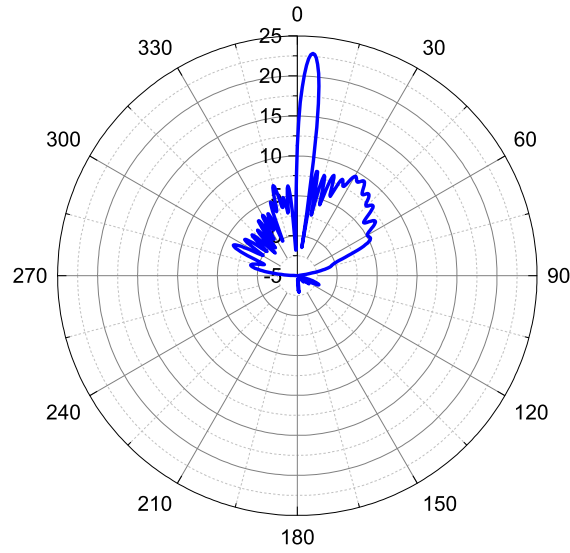


Figure 7.25: Simulated radiation pattern of the HAIA SIW H-sectoral at $f_o=18.4$ GHz, $\theta_m = 4^\circ$, E-plane ($\phi = 0^\circ$).

Table 7.10: Performance results of the HAIA SIW H-sectoral at $f_o = 18.4$ GHz, $\theta_d = 0^\circ$ and $\theta_d = 90^\circ$.

f_o [GHz]	S_{11} [dB]	Gain[dB]	θ_m [°]	HPBW[°]	SLL[dB]	Cross-pol [dB]
18.4	-17.65	22.87	4	3.51	-13.41	-36.82
18.4	-10.31	12	62	5	-2.30	-35.45

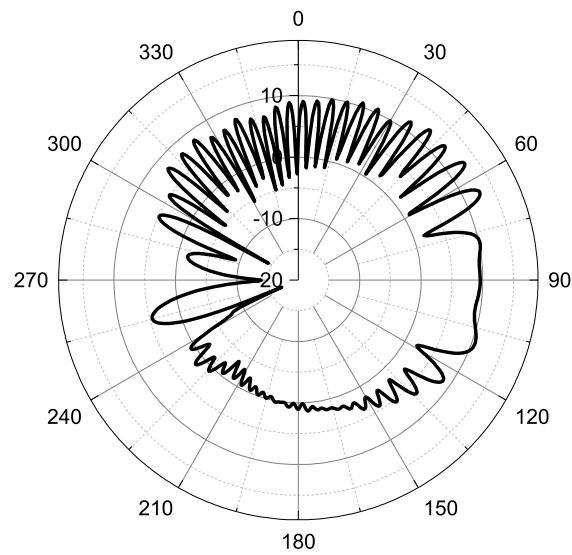


Figure 7.26: Simulated radiation pattern of the HAIA SIW H-sectoral at $f_o = 18.4$ GHz, $\theta_d = 90^\circ$ E-plane ($\phi = 0^\circ$).

In this chapter, the antenna is designed in the X and Ku bands, as well as in terahertz frequency to present the scalability of the antenna for operation in another frequency range by applying the same design theory used in the proof of concept at 18.4 GHz.

8.1

Results for the X and Ku bands

The HAIA is modeled to operate at the central frequencies of 11.63 GHz and 14.29 GHz, with specific application in FSS (Fixed Satellite Service). The SIW feeding and the holographic surface are easily adjusted to work at these frequencies of interest, keeping the same characteristics of the dielectric substrate used at the design frequency of the proof of concept. The length of the unit cell has a size of $a = 4.7$ mm for 11.63 GHz and $a = 3.8$ mm for 14.29 GHz. Figure 8.1 and 8.2 show the impedance curve for the unit cells proposed.

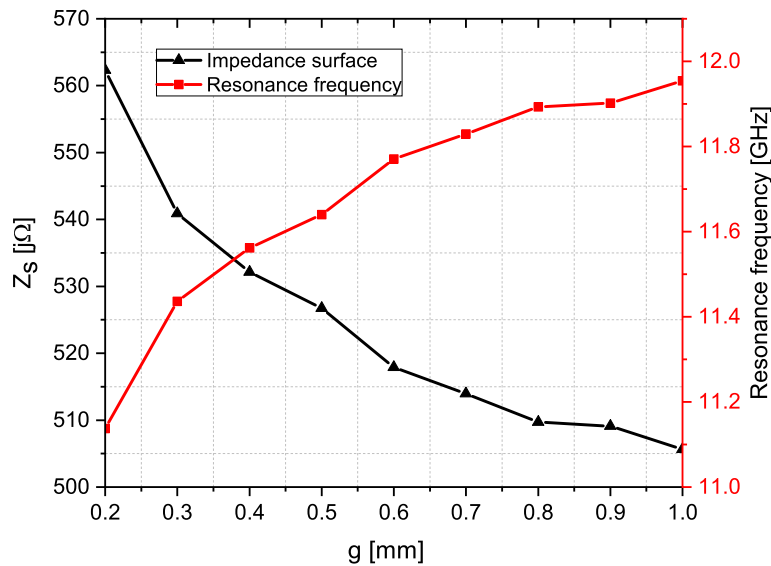


Figure 8.1: Relationship between the gap and surface impedance of the unit cell, at the central frequency of 11.63 GHz.

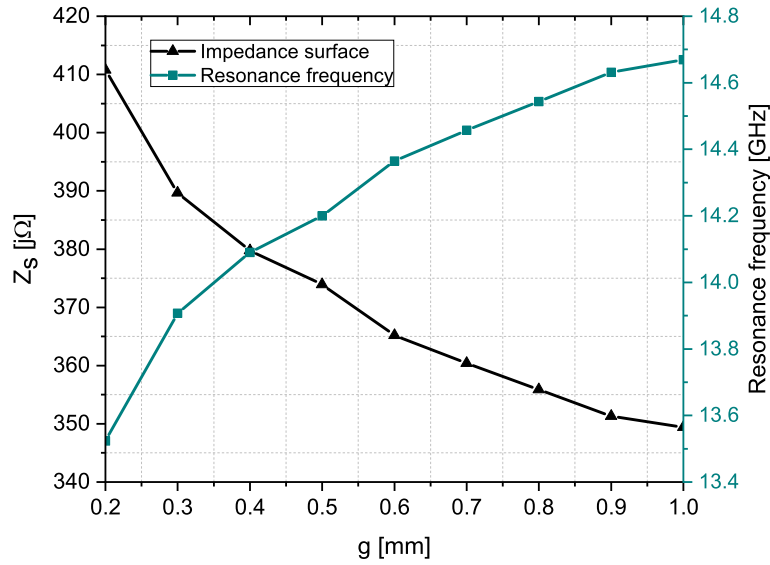


Figure 8.2: Relationship between the gap and impedance surface of the unit cell, at central frequency of 14.29 GHz.

Using the results of figure 8.1 and 8.2, polynomial approximations are calculated to obtain the relationship between g and the surface impedance for 11.63 GHz and 14.29 GHz, respectively, which are given by

$$g = -5.83^{-6}(Z_s^3) + 9.62^{-3}(Z_s^2) - 5.29(Z_s) + 971.50, \quad (8-1)$$

$$g = -3.57^{-6}(Z_s^3) + 4.28^{-3}(Z_s^2) - 1.71(Z_s) + 230.4. \quad (8-2)$$

Figure 8.3 and 8.4 show the simulated reflection coefficient of the SIW feedings. In order to maintain a good antenna performance, the holographic size of $15.33\lambda^2$ is used at the central frequencies under designs, because at the lower frequencies, the size of the holographic surface increases. As in the proof of concept, the design angle of 20° is chosen. Figure 8.5 and figure 8.6 show the result of the radiation pattern for the co-polarization component of the gain in the E-plane ($\phi = 0^\circ$), respectively in 11.63 GHz and 14.29 GHz.

Table 8.1 shows the summary results for the two antennas designed. A maximum gain of 20.92 dB at 11.63 GHz and 21.76 dB at 14.29 GHz is found. Given the results, good performance has been found in the HAIAs compared with the result of the proof of concept, presenting the leaky-wave radiation characteristic, which demonstrates its easy scalability in those frequency ranges. For the frequency of 14.29 GHz, optimization setting in the leakage energy can be implemented to enhance the agreement between the designed angle and the result of the simulated angle.

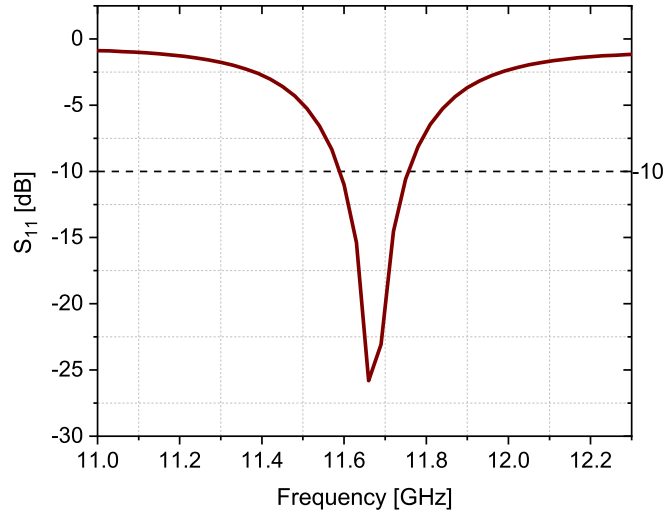


Figure 8.3: Reflection coefficient of the SIW feeding at central frequency of 11.63 GHz (bandwidth operation from 11.60 to 11.75 GHz, BW = 150 MHz).

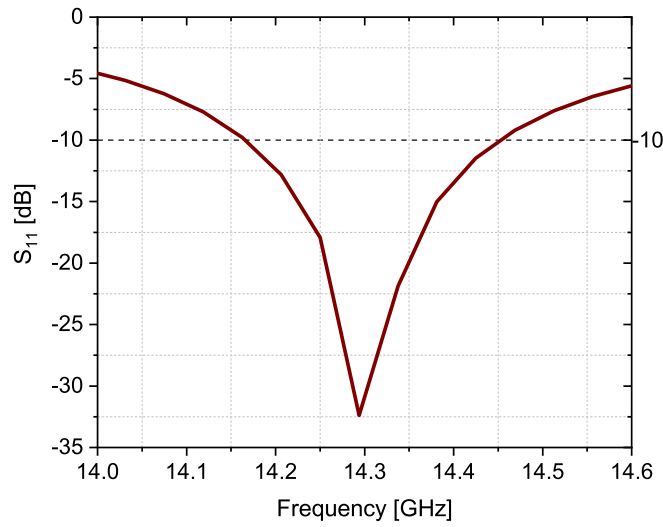


Figure 8.4: Reflection coefficient of the SIW feeding at central frequency of 14.29 GHz (bandwidth operation from 14.20 to 14.42 GHz, BW = 220 MHz).

Table 8.1: Performance results of the HAIA SIW H-sectoral at $f_o = 11.63$ GHz and $f_o = 14.29$ GHz.

f_o [GHz]	S_{11} [dB]	Gain[dB]	θ_m [°]	HPBW[°]	SLL[dB]	Cross-pol [dB]
11.63	-15.66	22.74	18	3.2	-13.58	-32.61
14.29	-14.47	21.76	28	3.8	-12.98	-53.57

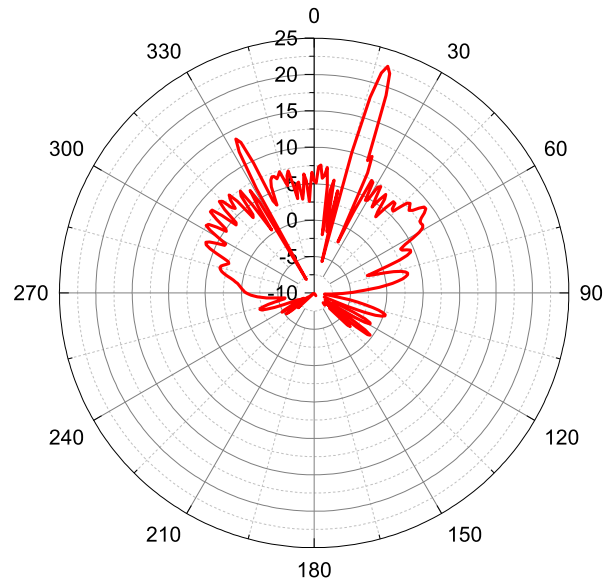


Figure 8.5: Radiation pattern of the co-polarization of the gain at $f_o = 11.63$ GHz, E-plane ($\phi = 0^\circ$).

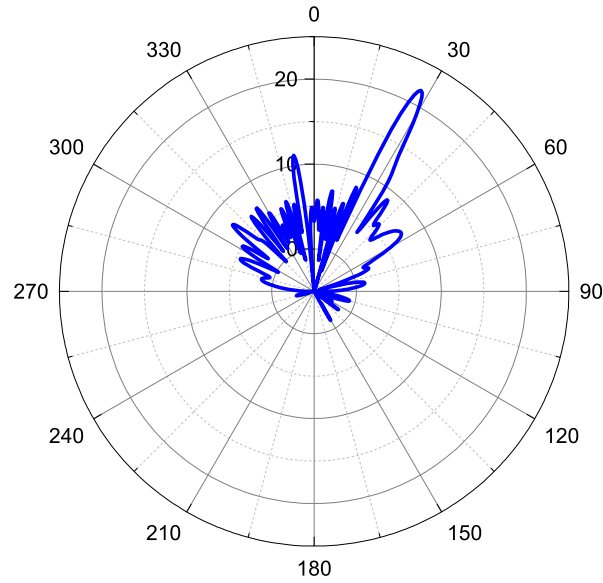


Figure 8.6: Radiation pattern of the co-polarization of the gain at $f_o = 14.29$ GHz, E-plane ($\phi = 0^\circ$).

8.2

Results for Terahertz Frequency

This section presents the design of the antenna in the terahertz range, demonstrating the step-by-step modeling at very high frequencies.

8.2.1

Modeling of the Unit Cell in THz Frequency

The proposed unit cell consists of a dielectric substrate with electric permittivity $\epsilon_r = 2.22$, $\tan\delta = 0.0009$, thickness substrate of $30 \mu m$ and thickness cooper of $0.3 \mu m$. The length of the square unit cell is $a = 46 \mu m$ with variations of the gap from $4 \mu m$ to $28 \mu m$ to obtain the resonance frequencies in the THz range. The unit cell is simulated on HFSS using the eigenmode function. The result of the relationship between impedance and the gaps is presented in figure 8.7, with variations between $98.63 j\Omega$ to $278.59 j\Omega$. The holographic surface is designed for a maximum radiation at 20° .

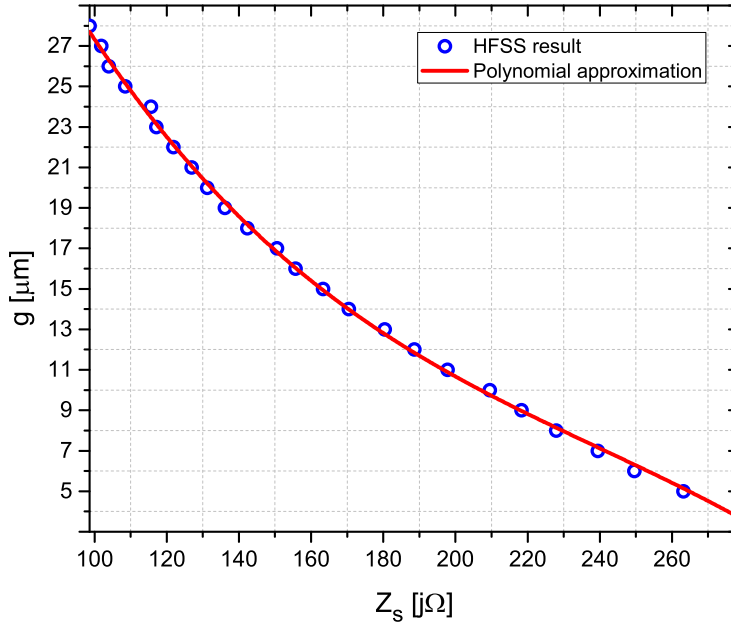


Figure 8.7: Impedance value for THz frequency.

The polynomial approximation is calculated to obtain the relationship with g and is given by

$$g = -3.10^{-6}(Z_s^3) + 2.23^3(Z_s^2) - 0.61(Z_s) + 70.02. \quad (8-3)$$

The waveguide aperture A and the length R_o in the SIW feeding are scaled to the terahertz dimension using the following approximations:

$$A = \frac{\lambda_o}{0.81}, \quad (8-4)$$

$$R_o = \frac{\lambda_o}{0.88}, \quad (8-5)$$

where λ_o is the wavelength of the fundamental frequency in the SIW feeding chosen to be 1 THz for study purposes. The values of the feeding dimensions

and the transition zone are summarized in table 8.2 and 8.3, where the total dimension is $L_m = 0.63$ mm and $W_m = 0.36$ mm.

Table 8.2: Parameters used in the SIW feeding in THz frequency.

w_{eff} [μm]	a [μm]	d_{via} [μm]	l_{via} [μm]	A [μm]	R_o [μm]
115	95	15	30	350	340

Table 8.3: Values of the transition zone in THz frequency.

L [μm]	p [μm]	g [μm]	S_1 [μm]	S_o [μm]
63	37	7	2.14	1

The dimensions of the holographic surface have the same proportion used in the proof of concept ($12.26\lambda^2$) to generate a size of $L_h = 3.1$ mm and $W_h = 3.1$ mm with 4,489 metallic square patches. The total area of the antenna is $W_h = 3.73$ mm and $L_h = 3.46$ mm.

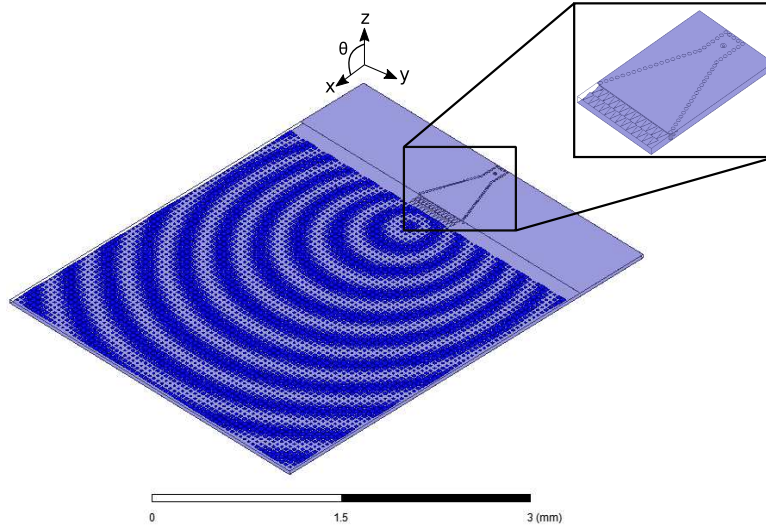


Figure 8.8: Antenna modeled in THz frequency.

Figure 8.9 shows the simulated reflection coefficient for the feeding and the whole antenna. Values of S_{11} lower than -10 dB are found in two frequency bands: 1.205 THz to 1.28 THz ($BW = 75$ GHz) and 1.35 THz to 1.395 THz ($BW = 45$ GHz).

For study purposes, the frequency of 1.205 THz is chosen as the design frequency of the antenna, where the simulated reflection coefficient obtained is -10.12 dB with a maximum gain of 23.35 dB at $\theta_m = 25^\circ$, HPBW of 5.45° and side lobe levels of -14.63 in the E-plane ($\phi = 0^\circ$) as shown in figure 8.10.

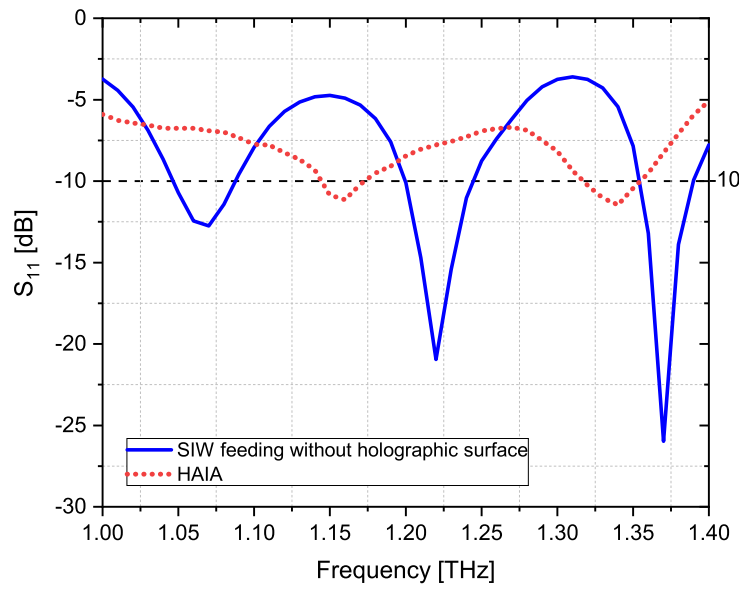


Figure 8.9: Simulated reflection coefficient of the HAIA operating at the THz frequency.

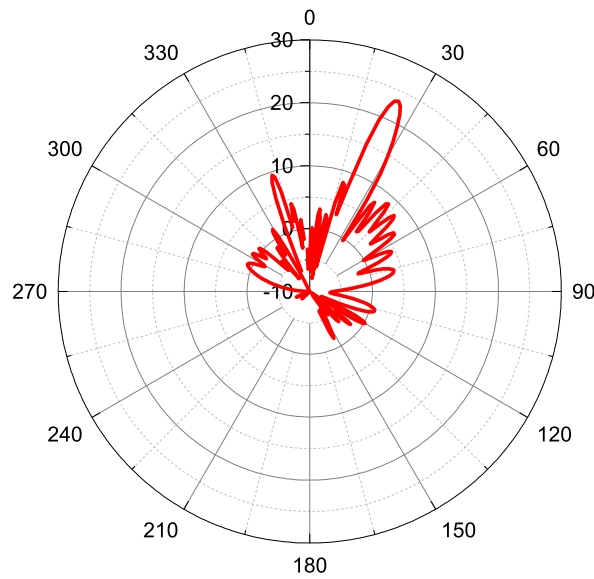


Figure 8.10: Simulated radiation pattern E-plane ($\phi = 0^\circ$) of the HAIA at $f_o = 1.205$ THz, with maximum gain of 24.45 dB.

Figure 8.11 and 8.12 show the frequency scanning of the antenna in the two bands found. Table 8.4 and 8.5 present the summary of the parameters evaluated. The results presented show a good antenna performance, demonstrating its feasibility of design at terahertz frequencies.

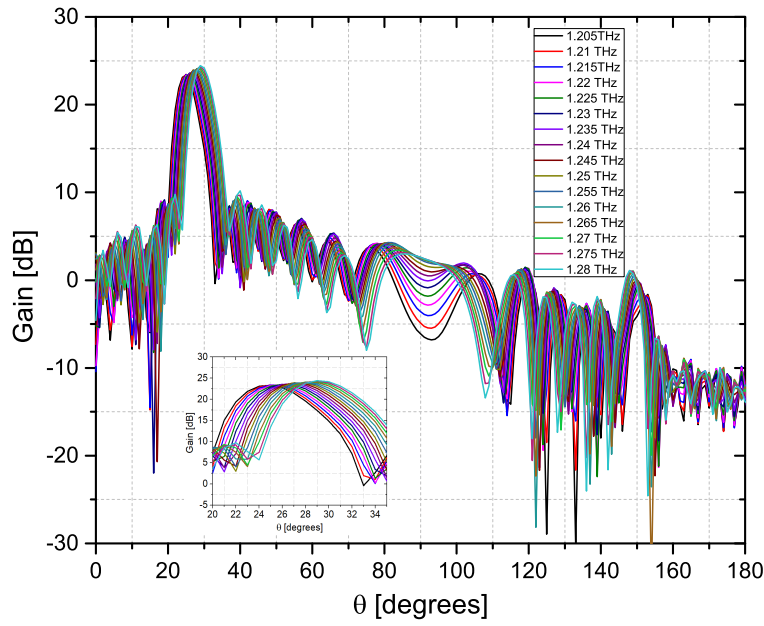


Figure 8.11: Radiation pattern of the HAIA, in the first band, E-plane ($\phi = 0^\circ$), THz frequency.

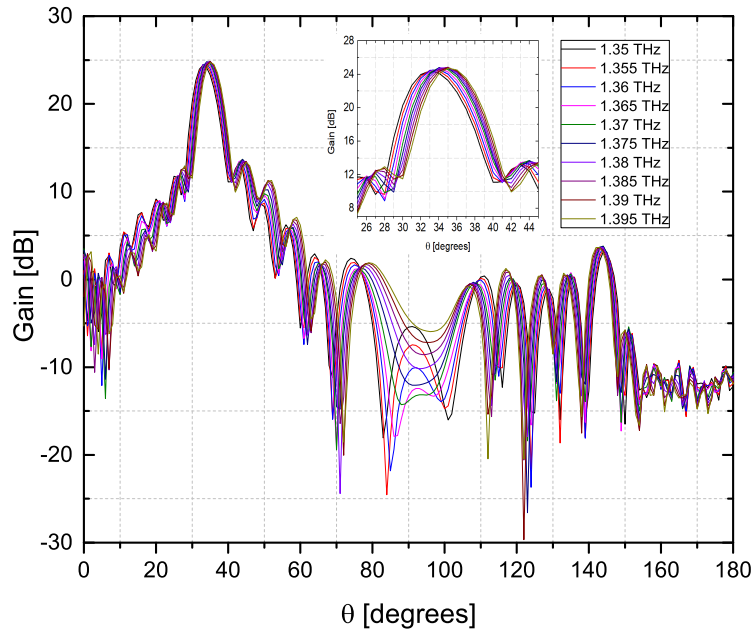


Figure 8.12: Radiation pattern of the HAIA, in the second band, E-plane ($\phi = 0^\circ$), THz frequency.

Table 8.4: Results of the HAIA in the first band, E-plane ($\phi=0^\circ$), THz frequency.

f_o [THz]	Gain[dB]	θ_m [$^\circ$]	HPBW[$^\circ$]	SLL[dB]	Cross-pol[dB]
1.205	23.35	25	6	-14.63	-46.35
1.21	23.43	25	6	-14.47	-43.70
1.215	23.41	25	5	-14.36	-39.72
1.22	23.45	26	6	-14.42	-38.23
1.225	23.55	26	6	-14.53	-38.23
1.23	23.58	26	5	-14.42	-42.26
1.235	23.65	27	6	-14.72	-45.57
1.24	23.82	27	5	-15.50	-45.57
1.245	23.92	27	5	-15.43	-45.57
1.25	23.93	27	6	-15.01	-45.57
1.255	24.01	28	6	-14.99	-45.57
1.26	24.07	28	6	-14.69	-45.57
1.265	24.11	28	6	-14.56	-45.57
1.27	24.23	29	5	-14.66	-45.57
1.275	24.36	29	5	-14.69	-45.57
1.28	24.44	29	6	-14.26	-45.57

Table 8.5: Results of the HAIA in the second band, E-plane ($\phi=0^\circ$), THz frequency.

f_o [THz]	Gain[dB]	θ_m [$^\circ$]	HPBW[$^\circ$]	SLL[dB]	Cross-pol[dB]
1.35	24.40	33	6	-14.63	-46.31
1.355	24.47	33	5	-14.47	-42.65
1.36	23.41	25	5	-14.36	-40.01
1.365	24.59	34	6	-14.42	41.19
1.37	24.68	34	6	-14.53	-39.20
1.375	24.77	34	5	-14.41	-42.30
1.38	24.79	34	6	-14.32	-44.32
1.385	24.81	35	6	-14.38	-46.78
1.39	24.84	35	6	-14.40	-44.15
1.395	24.79	35	5	-14.52	-45.10

9

Prototype Realization and Results

In this chapter the measured parameters of the antenna fabricated are exhibited. The parameters of the antenna, such as the reflection coefficient and radiation pattern will be presented for comparative results between simulations and implementation.

The measurement setup for the reflection coefficient was carried out using a network vector analyzer and the characterization of the radiation pattern was performed in the anechoic chamber of CETUC (Center of Study in Telecommunications).

9.1

Prototype of the Fabricated Antenna

Figure 9.1 shows the antenna fabricated for the dimensions on the holographic surface of $12.26\lambda^2$. The connector used in the coaxial probe is a waveguide probe 2.92 mm (K) Jack (Female) with a central pin of 0.38 mm in diameter, corresponding to the same dimension implemented in the simulations. The specification sheet is included in Appendix A.

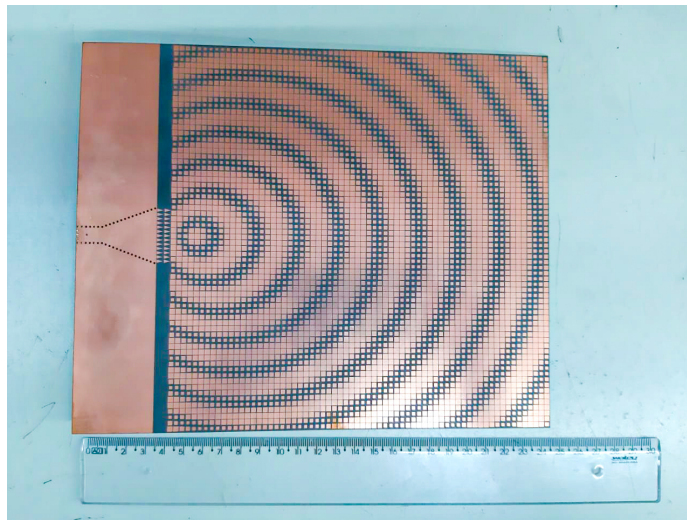


Figure 9.1: Demonstration of the fabricated antenna (rule in cm).

9.2
Measurement of the Reflection Coefficient

The reflection coefficient was measured using a Signal Integrity Network Analyzer SPARQ - 4002M Teledyne Lecroy. Figure 9.2 and 9.3 present the setup of the measurements.

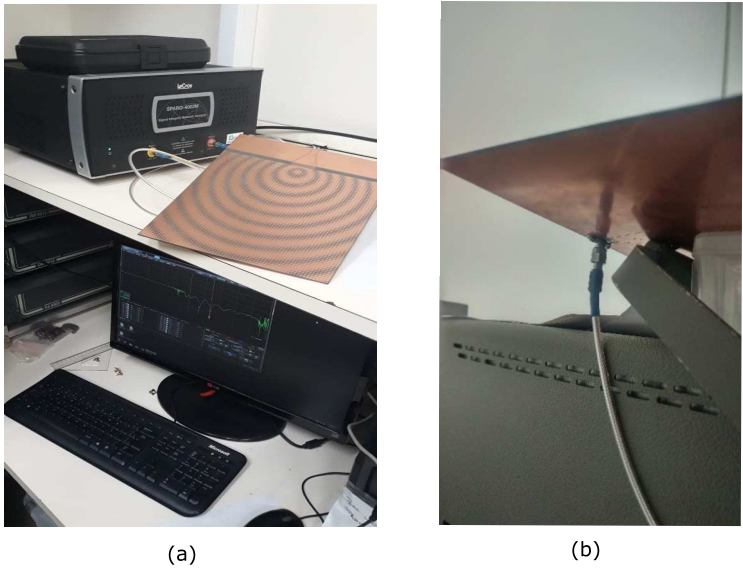


Figure 9.2: Setup for the measurement of the reflection coefficient: (a) top view of the holographic surface, and (b) close view of the feeding system.



Figure 9.3: Software of the analyzer Teledyne Lecroy.

Figure 9.4 shows a comparative result of the measured and simulated reflection coefficient. A good agreement is obtained between the results. The measured result presents a dual-band operation in the antenna: 15.78 - 16.42 GHz (640 MHz) and 17.82 - 18.50 (658 MHz).

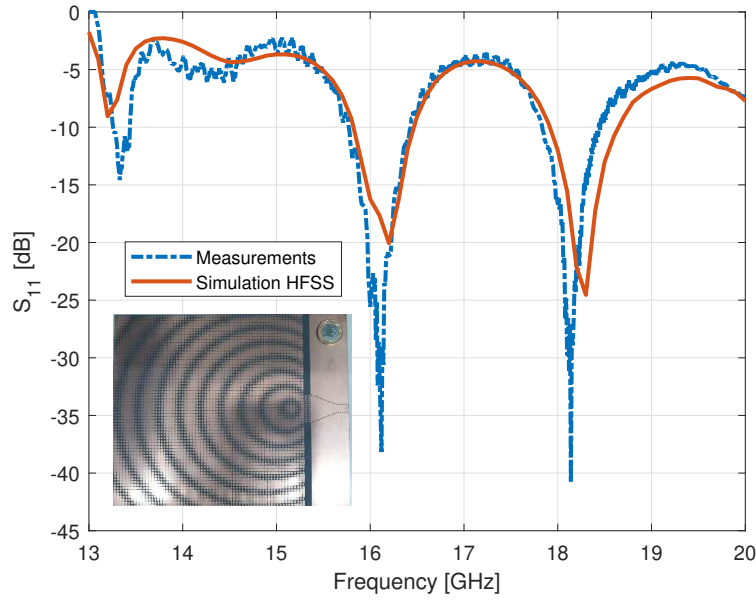


Figure 9.4: Comparative result between the simulated and measured reflection coefficient of the antenna.

9.3 Measurements in Anechoic Chamber

A FieldFox Microwave Analyzer 44 GHz was used to measure the transmission coefficient parameter (S_{21}). The initial setup was implemented with two identical horn antennas adapted in the anechoic chamber, as illustrated in figure 9.5. The specifications sheet of the horn antenna is included in Appendix B. Figure 9.6 shows the radiation pattern measured in the initial setup.

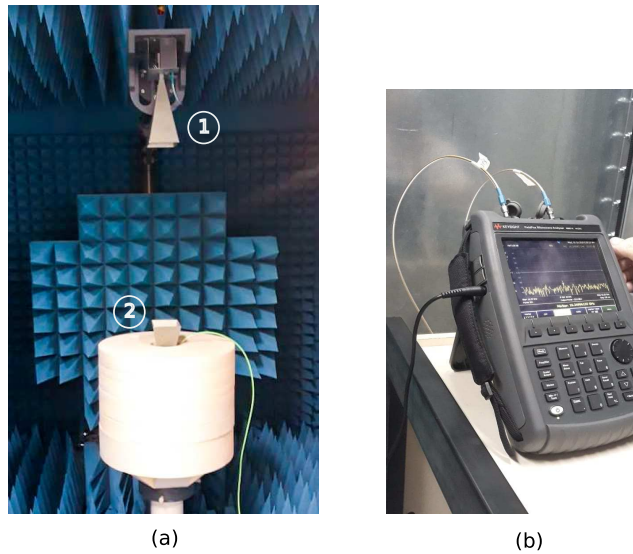


Figure 9.5: Initial setup in the anechoic chamber of CETUC, at 18.4 GHz: (a) position of the horn antennas with 20 dB of gain, and (b) FieldFox analyzer.

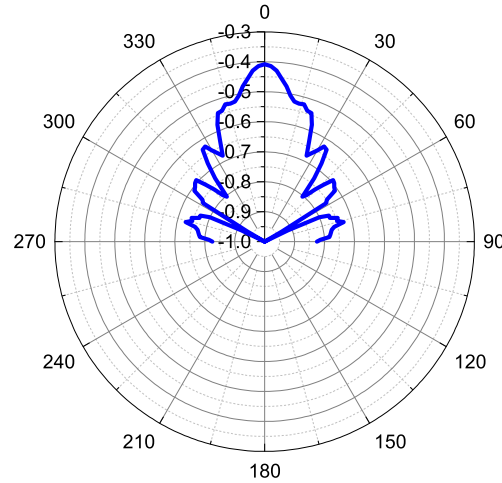


Figure 9.6: Normalized radiation pattern measured of the horn antenna for the initial setup at $f_o = 18.4$ GHz, E-plane ($\phi = 0^\circ$).

It was proven based on the calculation of the effective area in the transmission antenna corresponding to horn antenna in the position 1 of the setup, that the minimum distance for the far-field radiation was of 25 cm, and the measurements performed were in 60 cm, which demonstrates the far-field condition in the setup of the anechoic chamber.

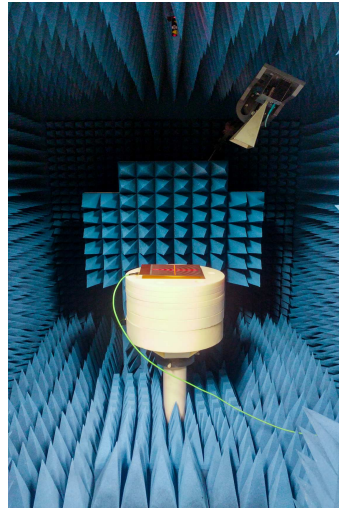


Figure 9.7: Setup in the anechoic chamber of CETUC to measures the co-polarization component of the HAIA.

The mechanical arm was rotated from -90° to 90° to obtain the graph of the radiation pattern in the co-polarization component. Figure 9.8 presents the radiation pattern measured at $f_o = 18.4$ GHz, showing good agreement with the simulated radiation pattern (see figure 7.7). Maximum radiation at 26° was obtained for the setup used in the anechoic chamber.

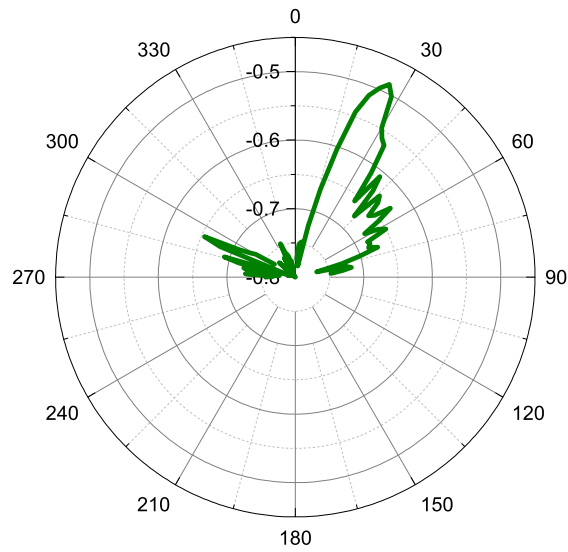


Figure 9.8: Normalized radiation pattern measured for the co-polarization gain at $f_o = 18.4$ GHz, E-plane ($\phi = 0^\circ$). Maximum radiation angle at 26° .

In order to measure the cross-polarization component at $f_o = 18.4$ GHz, the horn antenna 1 was rotated 90° , and the mechanical arm was rotated between -90° and 90° . Figure 9.9 shows the results between the co-polarization and cross-polarization component, with a value of -19 dB in the cross-polarization measurement.

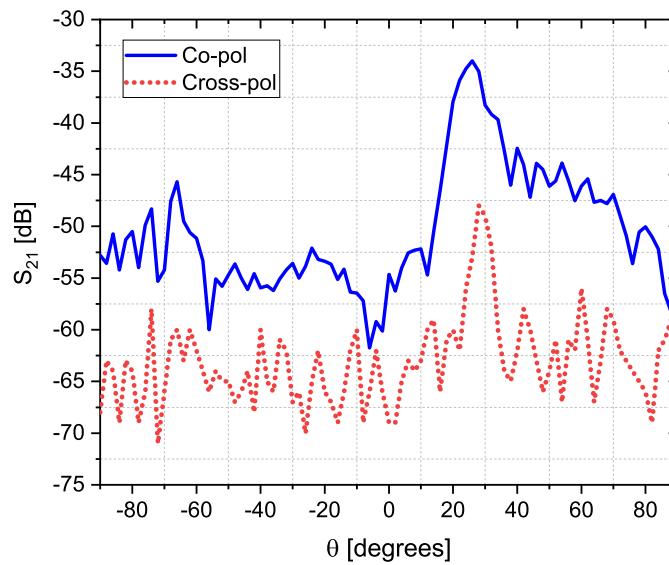


Figure 9.9: Transmission coefficient measured for the co- and cross-polarization component of the HAIA at 18.4 GHz.

To prove the frequency scanning of the antenna, two additional frequencies were tested in the second operating bandwidth of the antenna at 18.2 GHz and 18.5 GHz. The results of the co-polarization components are shown in figure 9.10 and 9.11.

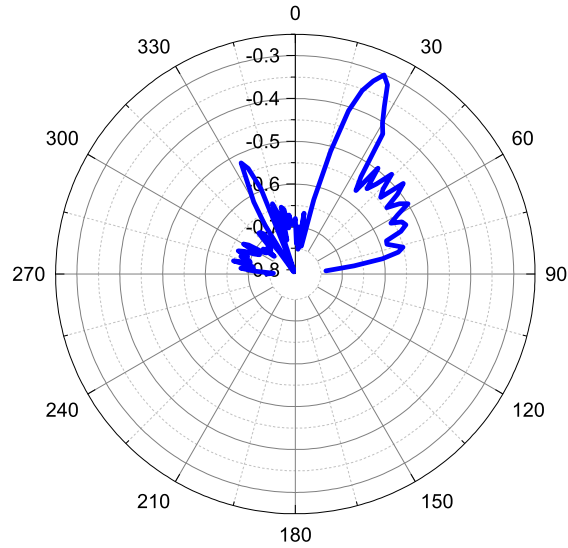


Figure 9.10: Normalized pattern measured for the co-polarization component of the antenna at $f_o = 18.2$ GHz. Maximum radiation angle at 24° .

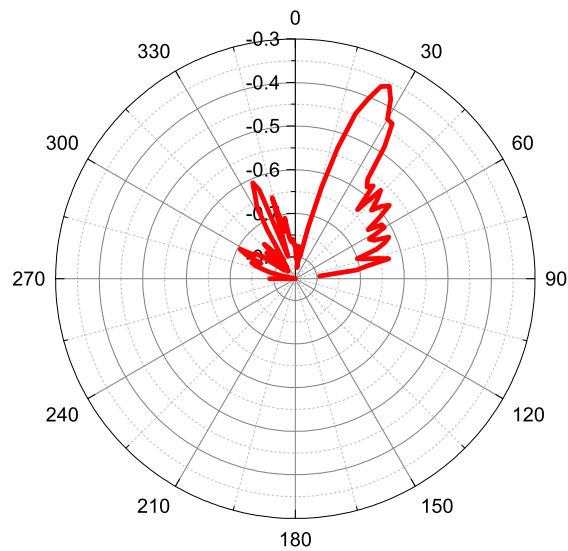


Figure 9.11: Normalized pattern measured for the co-polarization component of the antenna at $f_o = 18.5$ GHz. Maximum radiation angle at 26° .

It is observed that the maximum radiation angle increases in response to the increase of the frequency as seen in the simulations. A fourth setup was made for the frequency of 16.2 GHz in the first operating band of the antenna. The radiation pattern is presented in figure 9.12. It is observed the presence of a high side lobe level as seen in the results of the simulation.

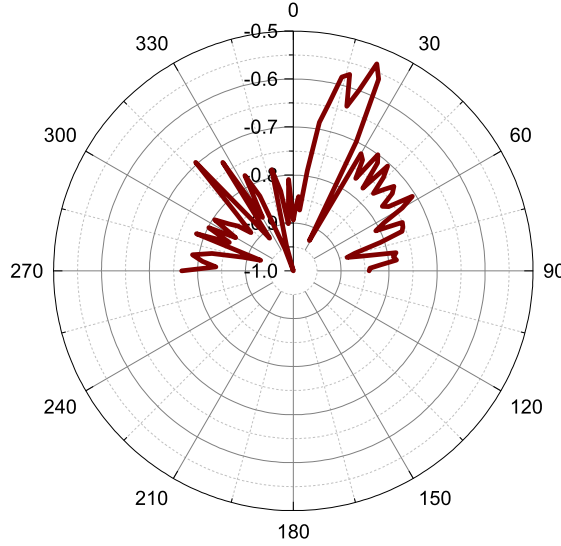


Figure 9.12: Normalized radiation pattern measured for the co-polarization component of the antenna at $f_o = 16.2$ GHz.

The value of the transmission coefficient (S_{21}) is useful for calculating the antenna gain through the Free-Space Path Loss (FSPL) equation [78], given by

$$FSPL = 20\log(d) + 20\log(f_o) + 32.45, \quad (9-1)$$

where d is the distance between the antennas in km, f_o is the frequency in MHz and 32.45 is the factor when are used magnitudes in kilometers and MHz. Table 9.1 and 9.2 present the summary of results for the setups measured.

A good agreement is found between the values measured and simulated of the gain and maximum radiation angles, except measures at 16.2 GHz, as explained above. Therefore, the fabricated prototype presents the best performance in the second operating band of the antenna, as seen in the simulations results. Appendix C shows the graphs of the near-field of the HAIA performed on HFSS.

Table 9.1: Results of the measured gain in the setups used.

Measures	FSPL[dB]	d[km]	f_o [MHz]	Gain meas.[dB]	Gain sim.[dB]
Horn ant.	-29.80	5^{-4}	18400	21.92	—
HAIA	-36.61	6^{-4}	16200	15.59	15.78
HAIA	-30.51	6^{-4}	18200	22.70	22.45
HAIA	-33.15	6^{-4}	18400	20.15	22.02
HAIA	-32.50	6^{-4}	18500	21.20	22.09

Table 9.2: Comparative results between the measured angle and simulated angle in the setups used.

Measures	f_o [GHz]	Max. angle measured [°]	Max. angle simulated [°]
Horn ant.	18.4	0	—
HAIA	16.2	22	14.5
HAIA	18.2	24	23
HAIA	18.4	26	23
HAIA	18.5	26	24

In this dissertation was carried out a study for the modeling and characterization of a holographic artificial impedance antenna (HAIA) with potential application in satellites system for the X and Ku bands due to its characteristic of high gain, narrow beamwidth, reduced size, low manufacturing cost in relation to other solutions, as well as its potential in the control of beam direction, which satisfies the requirements of the next-generation communication networks.

Three types of surface wave feeding were studied and evaluated through the established design goals: SIW H-sectoral with coaxial probe connection, SIW H-sectoral with microstrip line and a monopole of a quarter-wavelength. For the SIW H-sectoral feeding different types of transition zone were analyzed to improve the directivity of the surface wave, where the use of small triangles allowed a better agreement between the FTBR parameter and the reflection coefficient in the feeding.

The simulation results exhibited a good performance with the SIW H-sectoral in the two types of connection used. For the design of the microstrip line, a higher bandwidth was obtained in the studied frequency range, being a solution when a higher bandwidth is required. However, the coaxial probe presented the best performance of the parameter FTBR and reflection coefficient.

The AIS was characterized with square copper patches distributed sinusoidally on the surface, applying the holographic technique used in the optical system to record and reconstruct the desired radiated field. The design frequency chosen to be studied is 18.4 GHz, and the maximum radiation angle for the test was 20°. Also, the limits of the forward radiation of the antenna were explored at 0° and 90°, which show good behavior in response to the angle designed on the holographic surface.

The difference between the maximum radiation of the designed angle and the maximum radiation of the simulated angle among the evaluated antennas presents an average variation of 3.25°. When the accuracy of the main lobe angle is critical, some adjust in the impedance parameters, such as X_s and M can be optimized. In this project, the direction of the main lobe of the antenna

can be steered by changing the frequency in the forward radiation region. In the simulations, increments of 1° were obtained in the maximum radiation angle for each frequency increase of 300 MHz in the operating band of 18 - 18.6 GHz.

A series of dimensions were evaluated on the holographic surface to find the minimum size capable of producing a efficient leaky-wave radiation, where the physical size that fulfills the design goals established in this work was $12.26\lambda^2$. It was observed that increasing the width W_h of the surface reduces the side lobe levels, and the increase of the length L_h generates a higher gain. In addition, another characteristic explored in the antenna was the modification of the holographic surface to improve the horizontal component of the electric field to produce a horizontal polarization as seen in the results.

Furthermore, it was observed that the HAIA with monopole presented a wider beamwidth using the same dimension of the holographic surface ($12.26\lambda^2$). For a narrow beamwidth with this feeding, it was necessary to increase to 25% of the size ($15.33\lambda^2$). Thus, an improvement in the result was obtained. However, to further improve the performance using a monopole will be necessary a higher increase of the holographic dimensions. Therefore, with the SIW H-sectoral feeding, the dimensions of the holographic surface can be reduced to 25% without affecting the performance of the antenna leading to a miniaturization process.

The HAIA with SIW H-sectoral coaxial probe connection of size $12.26\lambda^2$ for vertical polarization was chosen to be fabricated. The proof of concept at the design frequency of 18.4 GHz allowed a fabrication-friendly employment given its smaller size. The lower frequencies would have resulted in a larger size and a higher manufacturing cost, and frequencies higher than 18.4 GHz would have presented measurement limitations in the available equipment.

In the final prototype, a simulated gain higher than 20 dB was obtained in the result for the bandwidth of interest exhibited from 18 GHz to 18.6 GHz, presenting a low cross-polarization component, HPBW of $\sim 4^\circ$ in the whole band, and low side lobe level. The fabricated antenna was measured in experimental tests using a vector network analyzer for the reflection coefficient, and the radiation pattern was characterized in the anechoic chamber of CETUC, presenting a good agreement between the measured and simulated results, demonstrating the leaky-wave radiation of the antenna and the frequency-controlled beam scanning.

The fabricated HAIA presents a good performance for the designed characteristic that improve the aperture efficiency in comparison with other evaluated works. The aperture efficiency relates the gain and the physical size

of the antenna. Therefore, the reduction of the dimensions using the SIW feeding does not have a negative effect on the efficiency of the antenna due to the directivity of the surface wave.

A final contribution in this work was the antenna design performed in the X and Ku bands, as well as in terahertz frequency, where the feeding of the surface wave and the holographic surface were easily scaled to those frequency ranges, showing the similar performance behavior of the proof of concept.

The following future works will be studied:

- Application of tensor impedance theory to produce a circular polarization in the antenna;
- Variation of the impedance parameters X_s and M in the holographic pattern to improve the precision result between the projected, simulated and measured maximum radiation angle, as well as reduce the level of the side lobes;
- Another kind of planar surface wave launcher can be explored, such as Vivaldi antenna for a more directive radiation pattern. Its effect on the leaky-wave radiation will be studied;
- For lower frequencies, such as X band, the length of the unit cell increases. Therefore, the total dimension of the holographic surface must be higher to maintain good performance. To try to reduce the dimensions of the structure, the effect to increase the electric permittivity of the dielectric substrate in the antenna will be studied. However, for a high permittivity, higher impedance values will be produced, creating a higher concentration of the electric field inside the substrate affecting the surface wave propagation along the surface. Therefore, an optimization process must be performed;
- The use of a lens with metamaterial to further improve the gain of the antenna;
- The feature of beam steering capability with a fixed frequency can be explored using microelectronic technology for the active control of the radiation pattern.

Bibliography

- [1] OJAROUDI PARCHIN, N.; JAHANBAKHSH BASHERLOU, H.; AL-YASIR, Y. I.; ABD-ALHAMEED, R. A.; ABDULKHALEQ, A. M. ; NORAS, J. M..
Recent developments of reconfigurable antennas for current and future wireless communication systems. Electronics, 8(2):128, 2019.
- [2] PANDI, S..
Holographic metasurface leaky wave antennas. 2017.
- [3] SCHÄFER, J.; DITTRICH, M.; GULAN, H. ; ZWICK, T..
Planar frequency scanning holographic antenna for FMCW-radar applications at 240 GHz. In: 2016 IEEE INTERNATIONAL SYMPOSIUM ON ANTENNAS AND PROPAGATION (APSURSI), p. 1401–1402. IEEE, 2016.
- [4] FONG, B. H.; COLBURN, J. S.; OTTUSCH, J. J.; VISHER, J. L. ; SIEVENPIPER, D. F..
Scalar and tensor holographic artificial impedance surfaces. IEEE Transactions on Antennas and Propagation, 58(10):3212–3221, 2010.
- [5] OLINER, A.; HESSEL, A..
Guided waves on sinusoidally-modulated reactance surfaces. IRE Transactions on Antennas and Propagation, 7(5):201–208, 1959.
- [6] CHEN, Z. N.; LIU, D.; NAKANO, H.; QING, X. ; ZWICK, T..
Handbook of Antenna Technologies. Springer Publishing Company, Incorporated, 2016.
- [7] ZENNECK, J..
Propagation of plane em waves along a plane conducting surface. Ann. Phys.(Leipzig), 23(1):907, 1907.
- [8] SIEVENPIPER, D. F..
High-impedance electromagnetic surfaces. 1999.
- [9] BALANIS, C. A..
Advanced engineering electromagnetics. John Wiley & Sons, 1999.
- [10] COLLIN, R. E..
Field theory of guided waves. 1960.
- [11] SOLYMAR, L.; SHAMONINA, E..
Waves in metamaterials. Oxford University Press, 2009.

- [12] OLINER, A. A.. **Leaky waves: Basic properties and applications.** In: PROCEEDINGS OF 1997 ASIA-PACIFIC MICROWAVE CONFERENCE, volumen 1, p. 397–400. IEEE, 1997.
- [13] VESELAGO, V.. **Electrodynamics of substances with simultaneously negative and.** Usp. Fiz. Nauk, 92:517, 1967.
- [14] VESELAGO, V.; BRAGINSKY, L.; SHKLOVER, V. ; HAFNER, C.. **Negative refractive index materials.** Journal of Computational and Theoretical Nanoscience, 3(2):189–218, 2006.
- [15] PENDRY, J. B.; HOLDEN, A. J.; ROBBINS, D. J.; STEWART, W. ; OTHERS. **Magnetism from conductors and enhanced nonlinear phenomena.** IEEE transactions on microwave theory and techniques, 47(11):2075–2084, 1999.
- [16] SMITH, D.; MOCK, J.; STARR, A. ; SCHURIG, D.. **Gradient index metamaterials.** Physical Review E, 71(3):036609, 2005.
- [17] SIHVOLA, A.. **Metamaterials: A personal view.** Radioengineering, 18(2), 2009.
- [18] KSHETRIMAYUM, R. S.. **A brief intro to metamaterials.** IEEE Potentials, 23(5):44–46, 2004.
- [19] SMITH, D. R.. **What are electromagnetic metamaterials? Novel electromagnetic materials (2006-06-10),** 2009.
- [20] CUI, T. J.; SMITH, D. ; LIU, R.. **Metamaterials theory, design, and applications.** 2010.
- [21] YABLONOVITCH, E.. **Photonic band-gap structures.** JOSA B, 10(2):283–295, 1993.
- [22] RAMOS, W. T.; MESQUITA, R. C. ; SILVA, E. J.. **Electric field distribution on surface of the artificial magnetic conductor: miniaturization process.** In: METAMATERIALS, METADEVICES, AND METASYSTEMS 2017, volumen 10343, p. 1034326. International Society for Optics and Photonics, 2017.
- [23] HSIAO, H.-H.; CHU, C. H. ; TSAI, D. P.. **Fundamentals and applications of metasurfaces.** Small Methods, 1(4):1600064, 2017.
- [24] LUUKKONEN, O.; SIMOVSKI, C. R.; RAISANEN, A. V. ; TRETYAKOV, S. A.. **An efficient and simple analytical model for analysis of**

- propagation properties in impedance waveguides. *IEEE Transactions on Microwave Theory and Techniques*, 56(7):1624–1632, 2008.
- [25] PANDI, S.; BALANIS, C. A. ; BIRTCHE, C. R.. **Design of scalar impedance holographic metasurfaces for antenna beam formation with desired polarization.** *IEEE Transactions on Antennas and Propagation*, 63(7):3016–3024, 2015.
- [26] LI, M.; XIAO, S.-Q. ; SIEVENPIPER, D. F.. **Polarization-insensitive holographic surfaces with broadside radiation.** *IEEE Transactions on Antennas and Propagation*, 64(12):5272–5280, 2016.
- [27] SUN, Z.; ZUO, X.; GUAN, T. ; CHEN, W.. **Artificial TE-mode surface waves at metal surfaces mimicking surface plasmons.** *Optics express*, 22(4):4714–4722, 2014.
- [28] LUUKKONEN, O.; SIMOVSKI, C.; GRANET, G.; GOUSSETIS, G.; LI-OUBTCHENKO, D.; RAISANEN, A. V. ; TRETYAKOV, S. A.. **Simple and accurate analytical model of planar grids and high-impedance surfaces comprising metal strips or patches.** *IEEE Transactions on Antennas and Propagation*, 56(6):1624–1632, 2008.
- [29] PATEL, M.. **Controlling electromagnetic surface waves with scalar and tensor impedance surfaces.** 2013.
- [30] LEE, J.; SIEVENPIPER, D. F.. **Patterning technique for generating arbitrary anisotropic impedance surfaces.** *IEEE Transactions on Antennas and Propagation*, 64(11):4725–4732, 2016.
- [31] MINATTI, G.; CAMINITA, F.; CASALETI, M. ; MACI, S.. **Spiral leaky-wave antennas based on modulated surface impedance.** *IEEE Transactions on Antennas and Propagation*, 59(12):4436–4444, 2011.
- [32] MOHSEN, M.; ISA, M. M.; ISA, A.; ZIN, M.; SAAT, S.; ZAKARIA, Z.; IBRAHIM, I.; ABU, M.; AHMAD, A. ; ABDULHAMEED, M.. **The fundamental of leaky wave antenna.** *Journal of Telecommunication, Electronic and Computer Engineering (JTEC)*, 10(1):119–127, 2018.
- [33] **Uniform waveguide leaky wave antenna.**
<https://www.spiedigitallibrary.org/conference-proceedings-of-spie/0544/0000/Uniform-Waveguide-Leaky-Wave-Antennas/10.1117/12.948248.full?SSO=1>.

- [34] BAHL, I.; GUPTA, K.. **Design considerations for leaky-wave antennas.** In: PROCEEDINGS OF THE INSTITUTION OF ELECTRICAL ENGINEERS, volumen 123, p. 1302–1306. IET, 1976.
- [35] GOLDSTONE, L.; OLINER, A.. **Leaky-wave antennas i: Rectangular waveguides.** IRE Transactions on Antennas and propagation, 7(4):307–319, 1959.
- [36] GOLDSTONE, L.; OLINER, A.. **Leaky wave antennas ii: Circular waveguides.** IRE Transactions on Antennas and Propagation, 9(3):280–290, 1961.
- [37] JACKSON, D.; OLINER, A. ; IP, A.. **Leaky-wave propagation and radiation for a narrow-beam multiple-layer dielectric structure.** IEEE Transactions on Antennas and Propagation, 41(3):344–348, 1993.
- [38] GUGLIELMI, M.; BOCCALONE, G.. **A novel theory for dielectric-inset waveguide leaky-wave antennas.** IEEE Transactions on Antennas and Propagation, 39(4):497–504, 1991.
- [39] BALANIS, C. A.. **Modern antenna handbook.** John Wiley & Sons, 2011.
- [40] DU PREEZ, J.; SINHA, S.. **Millimeter-wave antennas: configurations and applications.** Springer, 2016.
- [41] SUTINJO, A.; OKONIEWSKI, M. ; JOHNSTON, R. H.. **Radiation from fast and slow traveling waves.** IEEE Antennas and Propagation Magazine, 50(4):175–181, 2008.
- [42] THOMAS, A.; ZUCKER, F.. **Radiation from modulated surface wave structures-i.** In: 1958 IRE INTERNATIONAL CONVENTION RECORD, volumen 5, p. 153–160. IEEE, 1966.
- [43] PATEL, A. M.; GRBIC, A.. **A printed leaky-wave antenna based on a sinusoidally-modulated reactance surface.** IEEE Transactions on Antennas and Propagation, 59(6):2087–2096, 2011.
- [44] MAHMOUD, S.; ANTAR, Y.. **Leaky wave antennas: Theory and design.** In: RADIO SCIENCE CONFERENCE (NRSC), 2013 30TH NATIONAL, p. 1–8. IEEE, 2013.
- [45] LIU, J.; JACKSON, D. R. ; LONG, Y.. **Substrate integrated waveguide (SIW) leaky-wave antenna with transverse slots.** IEEE Transactions on Antennas and Propagation, 60(1):20–29, 2012.

- [46] KARL, N. J.; MCKINNEY, R. W.; MONNAI, Y.; MENDIS, R. ; MITTLEMAN, D. M.. **Frequency-division multiplexing in the terahertz range using a leaky-wave antenna**. *Nature Photonics*, 9(11):717, 2015.
- [47] FUSCALDO, W.; TOFANI, S.; BURGHIGNOLI, P.; BACCARELLI, P. ; GALLI, A.. **Terahertz leaky-wave antennas based on metasurfaces and tunable materials**. In: *METAMATERIALS AND METASURFACES*. IntechOpen, 2018.
- [48] GAO, S. S.; QIAO, H. M. ; LI, J. L.. **High gain holographic antenna for terahertz applications**. *Optical Materials Express*, 8(2):452–462, 2018.
- [49] GAO, S. S.; QIAO, H.-M. ; LI, J.-L.. **Multibeam holographic antenna for terahertz applications**. *Optik*, 181:538–544, 2019.
- [50] GAO, S. S.; QIAO, H.-M. ; LI, J.-L.. **High gain terahertz antenna based on modified holographic artificial impedance surface**. *Optik*, 170:185–189, 2018.
- [51] HEJASE, J. A.; PALADHI, P. R. ; CHAHAL, P. P.. **Terahertz characterization of dielectric substrates for component design and nondestructive evaluation of packages**. *IEEE Transactions on Components, Packaging and Manufacturing Technology*, 1(11):1685–1694, 2011.
- [52] CHECCACCI, P.; RUSSO, V. ; SCHEGGI, A.. **Holographic antennas**. *IEEE Transactions on Antennas and Propagation*, 18(6):811–813, 1970.
- [53] PETOSA, A.; THIRAKOUNE, S.; LEVIS, K. ; ITTIPIBOON, A.. **Microwave holographic antenna with integrated printed dipole feed**. *Electronics Letters*, 40(19):1162–1163, 2004.
- [54] **The museum of holography, chicago illinois**. <https://www.atlasobscura.com/places/museum-holography-mro>.
- [55] HARIHARAN, P.; HARIHARAN, P.. **Optical Holography: Principles, techniques and applications**. Cambridge University Press, 1996.
- [56] LI, A.; SINGH, S. ; SIEVENPIPER, D.. **Metasurfaces and their applications**. *Nanophotonics*, 7(6):989–1011, 2018.
- [57] BIRD, T. S.. **Definition and misuse of return loss [report of the transactions editor-in-chief]**. *IEEE Antennas and Propagation Magazine*, 51(2):166–167, 2009.

- [58] BANSAL, R.. **Handbook of engineering electromagnetics**. CRC Press, 2004.
- [59] BALANIS, C. A.. **Antenna theory: analysis and design**. John Wiley & sons, 2016.
- [60] LUDWIG, A.. **The definition of cross polarization**. IEEE Transactions on Antennas and Propagation, 21(1):116–119, 1973.
- [61] PODILCHAK, S. K.; FREUNDORFER, A. P. ; ANTAR, Y. M.. **Surface-wave launchers for beam steering and application to planar leaky-wave antennas**. IEEE Transactions on Antennas and Propagation, 57(2):355–363, 2009.
- [62] RUSCH, C.; BEER, S.; GULAN, H. ; ZWICK, T.. **Holographic antenna with antipodal feed for frequency-scanning radar**. In: 2013 IEEE ANTENNAS AND PROPAGATION SOCIETY INTERNATIONAL SYMPOSIUM (APSURSI), p. 234–235. IEEE, 2013.
- [63] ESQUIUS-MOROTE, M.; FUCHS, B.; ZÜRCHER, J.-F. ; MOSIG, J. R.. **A printed transition for matching improvement of SIW Horn antennas**. IEEE Transactions on Antennas and propagation, 61(4):1923–1930, 2013.
- [64] ESQUIUS-MOROTE, M.; FUCHS, B.; ZÜRCHER, J.-F. ; MOSIG, J. R.. **Novel thin and compact H-plane SIW Horn antenna**. IEEE Transactions on Antennas and Propagation, 61(6):2911–2920, 2013.
- [65] NANNETTI, M.; CAMINITA, F. ; MACI, S.. **Leaky-wave based interpretation of the radiation from holographic surfaces**. In: 2007 IEEE ANTENNAS AND PROPAGATION SOCIETY INTERNATIONAL SYMPOSIUM, p. 5813–5816. IEEE, 2007.
- [66] CHENG, Y.-M.; MENG, F.-Y.. **Miniaturized planar holographic antenna with surface-wave launcher feed**. In: 2015 7TH ASIA-PACIFIC CONFERENCE ON ENVIRONMENTAL ELECTROMAGNETICS (CEEM), p. 20–23. IEEE, 2015.
- [67] JOHNSON, R. C.; JASIK, H.. **Antenna engineering handbook**. New York, McGraw-Hill Book Company, 1984, 1356 p. No individual items are abstracted in this volume., 1984.
- [68] DESLANDES, D.; WU, K.. **Integrated microstrip and rectangular waveguide in planar form**. IEEE Microwave and Wireless Components Letters, 11(2):68–70, 2001.

- [69] BOZZI, M.; GEORGIADIS, A. ; WU, K.. **Review of substrate-integrated waveguide circuits and antennas.** IET Microwaves, Antennas & Propagation, 5(8):909–920, 2011.
- [70] BENEDEK, P.; SILVESTER, P.. **Capacitance of parallel rectangular plates separated by a dielectric sheet.** IEEE Transactions on Microwave Theory and Techniques, 20(8):504–510, 1972.
- [71] LI, Y. B.; CAI, B. G. ; CUI, T. J.. **Design of multi-beam holographic leaky-wave antenna with one/two-dimension frequency sweep.** In: 2014 IEEE-APS TOPICAL CONFERENCE ON ANTENNAS AND PROPAGATION IN WIRELESS COMMUNICATIONS (APWC), p. 582–584. IEEE, 2014.
- [72] ZHANG, Y.; OUYANG, J.; ZHANG, K.-Z.; LONG, Y.; ZHOU, L.-J. ; YANG, F.. **Conformal antennas based on holographic artificial impedance surfaces.** In: 2014 IEEE ANTENNAS AND PROPAGATION SOCIETY INTERNATIONAL SYMPOSIUM (APSURSI), p. 1552–1553. IEEE, 2014.
- [73] RAMALINGAM, S.; PANDI, S.; BALANIS, C. A. ; BIRTCHER, C. R.. **Axial and circumferential modulation on cylindrical metasurfaces.** In: 2017 IEEE INTERNATIONAL SYMPOSIUM ON ANTENNAS AND PROPAGATION & USNC/URSI NATIONAL RADIO SCIENCE MEETING, p. 279–280. IEEE, 2017.
- [74] NWAJANA, A. O.; DAINKEH, A. ; YEO, K. S.. **Substrate integrated waveguide (SIW) bandpass filter with novel microstrip-CPW-SIW input coupling.** Journal of Microwaves, Optoelectronics and Electromagnetic Applications, 16(2):393–402, 2017.
- [75] CALEFFO, R. C.. **New design procedure to determine the taper transition for impedance matching between microstrip line and siw component.** Journal of Microwaves, Optoelectronics and Electromagnetic Applications, 15(3):247–260, 2016.
- [76] KOBAYASHI, M.; SAWADA, N.. **Analysis and synthesis of tapered microstrip transmission lines.** IEEE transactions on microwave theory and techniques, 40(8):1642–1646, 1992.
- [77] **Planar integrated holographic antenna with substrate integrated waveguide.** <https://pdfs.semanticscholar.org/ff1a/34d2a65a850ee0ac9a86e09dc0507cab546d.pdf>.

- [78] GIDY, F.. **Fractal configurations for millimeter wave antennas design**. PhD thesis, Department of Electrical Engineering. Pontifical Catholic University of Rio de Janeiro, September 2016.

A

Specification Sheet of the Coaxial Probe Connector

PUC-Rio - Certificação Digital Nº 1721783/CA

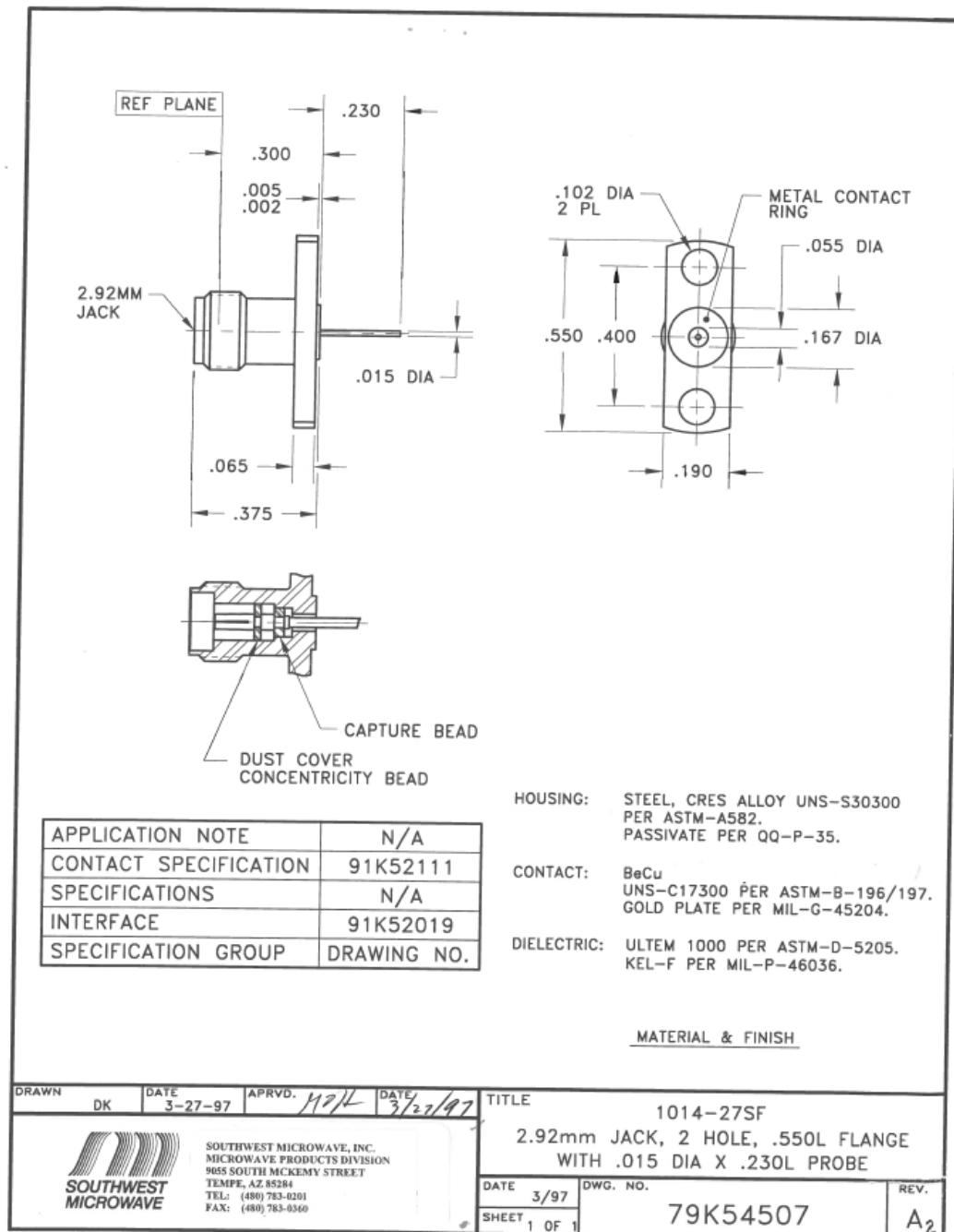

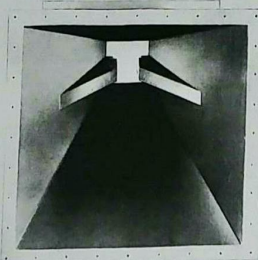


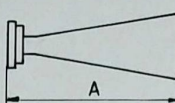
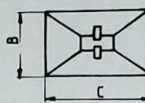
Figure A.1: Connector of the antenna.

B Specification sheet of the Horn Antenna


MICROGUIDE LTD.



HORNS WITH DOUBLE RIDGE INPUT

Specifications

Temperature Range: -55 C to +150 C

Housing Finish: Paint, enamel

VSWR: 1.15 max.

Material: Aluminum

Finish: Paint, enamel

Microguide AN-DR series standard gain horns are accurate gain standards. The unknown gain of an antenna can be accurately determined by comparison with the appropriate horn. They are also useful in other propagation studies where relatively narrow and controlled beam width is required. A curve of gain vs. frequency is provided with each on request. They are also available with coaxial input connectors, SMA, TNC, N Type, SC.

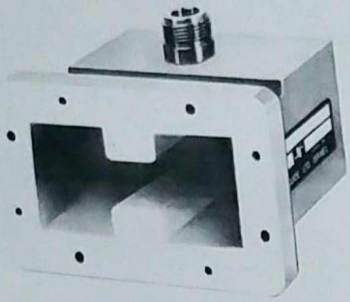
Frequency Range (GHz)	Waveguide WRD No.	Flange	Gain at mid. freq.	Dimensions (in)			Microguide Part No.
				a	b	c	
2.0-4.8	200-D24	F-2001	20	30	11.0	15.0	AN-200-DR
3.5-8.2	350-D24	F-3501	20	14	7.0	11.0	AN-350-DR
4.75-11	475-D24	F-4751	20	12	4.0	5.3	AN-475-DR
4.75-11	DR-19	F-1901	20	12	4.0	5.3	AN-190-DR
5.8-16	580-D28	F-5801	20	11	3.7	4.9	AN-580-DR
6.5-18	650-D28	F-6501	20	8	3.0	4.1	AN-650-DR
7.5-18	750-D24	F-7501	20	8	3.0	4.0	AN-750-DR

88 GIBOREI ISRAEL ST., TEL AVIV 67891, ISRAEL, TEL. 03-255181-5, TELEX: 33578

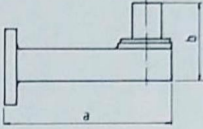
B 3

Figure B.1: Specification sheet Horn antenna.

MICROGUIDE LTD.



DOUBLE-RIDGE WAVEGUIDE TO COAX ADAPTERS



Specifications

Coaxial Connector:	type N female
Temperature Range:	-55° C to +150° C
Housing Finish:	paint, enamel
Flange Material:	Aluminum 6061-T6
Flange Finish:	C-5541

Microguide WCA Series Adapters provide a Low VSWR Transition from a D.R. Waveguide to a coaxial transmission line. Special designs are available on request. VSWR over a full octave band is less than 1.25. Swept frequency test data will be supplied on request.

VSWR of 1.15 for octave band can be supplied on request.

Frequency Range (GHz)	Waveguide WRD No.	Flange	Max. VSWR	Dimensions (Max. mm)		Microguide Part No.
				a	b	
2-4.8	200-D24	F-2001	1.25	63.5 (2.5")	55 (2.2")	WCA-200
3.5-8.2	350-D24	F-3501	1.25	58.5 (2.3")	38 (1.5")	WCA-350
4.75-11	DR-19	F-1901	1.25	54 (2.1")	33 (1.3")	WCA-190
4.75-11	475-D24	F-4751	1.25	54 (2.1")	33 (1.3")	WCA-475
5.8-16	580-D28	F-5801	1.25	46 (1.8")	25 (1")	WCA-580
6.5-18	650-D28	F-6501	1.25	46 (1.8")	25 (1")	WCA-650
7.5-18	750-D24	F-7501	1.25	46 (1.8")	25 (1")	WCA-750

Note: WCA-580 — 650 — 750 are supplied with a SMA Female connector. Special connectors: SMA, TNC, 7 MM, N Type Male are supplied on special request.

88 GIBORET ISRAEL ST. TEL AVIV 67891 ISRAEL TEL 03-7551815 TELEX 31578

A

Figure B.2: Specification sheet of the waveguide of the Horn antenna.

C

Near-field Plots

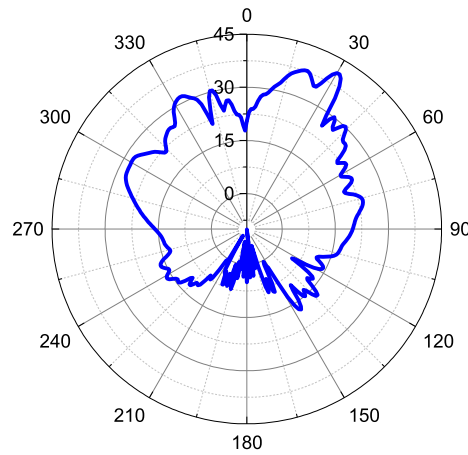


Figure C.1: Radiation pattern near-field, co-polarization component of the electric field at $f_o = 18.4$ GHz.

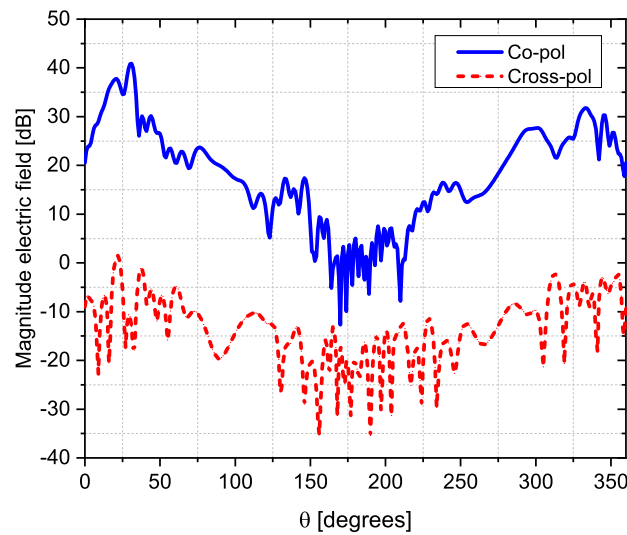


Figure C.2: Radiation pattern near-field, co- and cross-polarization components of the electric field at $f_o = 18.4$ GHz.